Second-sphere ligand field effects on oxygen ligator atoms and experimental evidence—the transition metal–oxygen bond in oxidic solids

Dirk Reinen [a,*], Michail Atanasov [b], Show-Ling Lee [a]

[a] *Fachbereich Chemie and Zentrum für Materialwissenschaften, Philipps-Universität,
Hans-Meerwein-Strasse, 35043 Marburg, Germany*
[b] *Institute of General and Inorganic Chemistry, Bulgarian Academy of Sciences, 1113 Sofia, Bulgaria*

Contents

  * Corresponding author. Tel.: + 49-6421-285792; Fax: + 49-6421-288917; e-mail: reinen@
ps1515.chemie.uni-marburg.de.

Abstract

The properties of the M–O bond in oxidic solids, where M is a low-valent 3d transition metal ion such as Ni^{II}, Cu^{II}, Co^{II} or Cr^{III}, are very variable depending on the structure and constitution of the respective compound, and are studied by optical and EPR spectroscopy. Specifically, high-valent cations in the cationic coordination of the oxygen ligator atoms beside M determine the bonding behaviour of oxygen towards the transition metal ions. Applying a newly developed extension of the angular overlap model (AOM) to fit the d–d spectra and the EPR g and hyperfine tensor components (Cu^{2+}), the bonding parameters e_σ and e_π for a great variety of structures and solids are evaluated. In these calculations a 2s–2p hybridisation on oxygen is anticipated, where the number and the geometrical arrangement of the high-valent cations (Nb^V, Sb^V; W^{VI}, Te^{VI}, etc.) determine the kind of hybridisation (sp, sp^2, sp^3) and the directional properties of the hybrid orbitals. A wide range of AOM parameters—e_σ ranging from ~ 3 to $\sim 5 \times 10^3$ cm^{-1} in the case of Ni^{2+}—is obtained, the most striking changes being observed, if a d^0 configurated cation (Nb^V, W^{VI}) is substituted by a cation with d^{10} configuration (Sb^V, Te^{VI}). Particularly interesting are anisotropies in the π-interactions in the case of sp^2 hybridised oxygen atoms, which lead to large symmetry splittings of the d–d transitions. The e_σ and e_π energies, which constitute the ligand field parameter Δ, turn out to be rather complex bonding parameters. They can be classified according to the local symmetry of the M–O bond in the respective crystal structure and correspond to the σ- and π-overlap capacities resulting from the modeling of the oxygen bonding properties by strongly contrapolarising cations in the oxygen coordination sphere. Additional information, specifically about the degree of covalence within the transition metal–oxygen bond, comes from the nephelauxetic ratio β and the mixing coefficient α of Cu^{II} in the ground state MO—both parameters deduced from the experiment. The obtained results can be nicely interpreted by defining effective electronegativities of oxygen towards the transition metal. Thus, high-valent and small cations as S^{VI} and P^V are strongly contrapolarising and generate highly ionic oxygen atoms comparable to the fluoride ions. The collected data are finally used to define oxygen ligand fields with the property to stablise the higher oxidation states of the late 3d metal ions (Cu^{III}, Ni^{III}, Ni^{IV}). © 1998 Elsevier Science S.A. All rights reserved.

1. Introduction and outline

The energies of electronic transitions within the $3d^n$ configuration of transition metal ions in the lower oxidation states, surrounded by ligands in solids and complexes, are predominantly determined by the interelectronic repulsion between the delocalised d-electrons and by the ligand field, namely the interaction between these electrons and the ligands. It is well known since the pioneering work of in particular Jorgensen [1,2] that both effects, represented by the Racah parameters B, C and the ligand field strength Δ, can be used as probes for the properties of the metal–ligand bonds. Thus, the interelectronic repulsion parameters, derived from the d–d spectra by using classical ligand field theory, show a reduction with respect to the 'free ion' values B_o, C_o, which becomes more pronounced with increasing

covalency (nephelauxetic effect). In cases of more covalent bonds parameters, B_{55}, B_{35}, B_{33} (similarly for C) have been proposed considering for example octahedral ligand fields, depending on whether only π-antibonding t_{2g}^* (γ_5) or σ-antibonding e_g^* (γ_3) orbitals (see below) are involved [2]. Such an approach gives a good semi-quantitative understanding for the degree of d-covalency of the metal–ligand bond also in the case of higher-valent d^n cations.

The situation is quite different regarding the ligand field parameter Δ or 10 Dq, which is defined as the energy difference $E(e_g^*) - E(t_{2g}^*)$ in octahedral coordination. This parameter does not vary in a simple way in dependence on the ligand covalency (polarisability). A break-through in the insight how bond properties are reflected by Δ was provided by the 'angular overlap model' (AOM). Its basic feature is the resolution of d-orbital perturbations into contributions from each individual ligand, discriminating between local $\sigma(e_\sigma)$- and $\pi(e_\pi)$-type metal–ligand interactions [3]. The AOM approach meets the chemists' view, who usually considers a complex or molecule as consisting of discrete two-atomic bonds. Since its introduction in the early 1960s [3] the AOM and the interpretation of the AOM parameters in terms of chemical bonding has become rather sophisticated—as in the cellular ligand field theory (CLF) [4]. The main proposition of the AOM and CLF is the use of an effective operator H_{LF}, which comprises the Coulomb and the LF potential terms for a best d-orbital set underlying all electronic states within the ligand field domain. This approach is justified only if the d-orbitals are weakly involved into the bonding, however, which is typical for 3d metal ions in lower oxidation states, and we will indeed restrict to examples of this kind. The 3d orbitals are rather contracted relative to 4s and 4p, implying that the latter contribute predominantly to the bond covalency. We may hence look at the 3d-ligand overlap as being of a higher-order type-utilising ligand orbitals, which are mainly used in LCAO's symmetry-adapted to metal 4s and 4p orbitals. However, a reasonable assumption is surely, that the metal 3d-ligand interaction is a sensitive probe for the total bond energies.

In the AOM the octahedral ligand field strength is the difference of two antibonding energy parameters e_σ and e_π (Eq. (1)). This parametrisation presents Δ as a complex bonding parameter, which depends on the interplay between σ- and π-overlap within the transition metal–ligand bond.

$$\Delta = E(e_g^*) - E(t_{2g}^*) = 3e_\sigma - 4e_\pi \tag{1}$$

Many studies have shown, that such a view can be very useful and may provide much insight into the bond character. A similar—by the factor 4/9 smaller—orbital splitting results for a 3d cation in tetrahedral coordination (Eq. (1a)). Here the e* state of lower energy is π-antibonding, while t_2^* reflects σ- and π-antibonding interactions. The e_σ and e_π in Eqs. (1) and (1a) are expected to be of equal magnitude for identical cations, ligands and bond lengths.

$$\Delta_{tet} = E(t_2^*) - E(e^*) = 4/9(3e_\sigma - 4e_\pi) \tag{1a}$$

A permanent point of irritation is the fact, however, that the AOM parameters derived from the experiment reflect not only covalent, but ionic interactions as well.

Attempts to separate the two contributions, were not successful [5]. Thus, a parameter interpretation has to be done to a large extent with chemical intuition.

A further fact, which we consider as particularly important, is that the parameters e_σ and e_π may exhibit a much more pronounced variation in dependence on the nature and charge of the 3d metal ion and the ligand than Δ itself, because even constant values of the latter parameter may imply e_σ and e_π energies of rather different magnitudes (Eq. (1)). This argument has been raised before by Smith [6]. Fig. 1a illustrates that even Δ may vary considerably for transition metal ions such as Ni^{2+}, if they are isomorphically substituted into the octahedral sites of oxidic solids with various structures and chemical compositions. The very large reduction of Δ passing from the spinel (I) to the perowskite lattice (III), which amounts to greater than 30% (3000 cm^{-1}), cannot be understood by using simple ligand field arguments [7]. Only the further red-shift of Δ from III to IV (1600 cm^{-1}) is clearly due to the expansion of the Ni^{2+} site by the much larger Ca^{2+} ion. The change of Δ—the Racah parameters B, C remaining nearly constant—is also visualised by the colour, which is determined by the position of the broad minimum between the two $^3A_{2g} \rightarrow {}^3_{a,b}T_{1g}$ transitions and varies from greenish blue to yellowish green to bright yellow in the sequence from I to III. For IV also a second minimum—that after the third main band at > 22000 cm^{-1}—is involved, the colour being violet-red in this case. An even lower Δ value would shift the first minimum into the IR and the second minimum towards the blue part of the visible region. A (violet) blue colour is expected and indeed observed for $Co^{II}O_4$ tetrahedra (Fig. 1b). The tetrahedral Co^{2+} has the same term diagram as the octahedral Ni^{2+}, but a by a factor of about 2 smaller Δ value.

The main purpose of this contribution is to emphasise the importance of the cationic coordination of the oxygen atoms in determining the properties of the transition metal–oxygen bond and their manifestitation in the AOM parameters, derived from the d–d spectra. For example the 3d metal–2s,2p oxygen overlap is expected to be of a different quality for oxygen atoms, imbedded into a planar Nb_2ONi ($NiSb_2O_6$, trirutile lattice) and in a pseudotetrahedral $GeONi_3$ coordination (Ni_2GeO_4, spinel structure). Because in the former case two high-valent strongly polarising metal atoms are present instead of only one in Ni_2GeO_4, a comparatively much larger part of the binding capacity of oxygen is needed by the high-valent cations, leading to significantly smaller AOM parameters for the Ni–O bond in the trirutile case—as will be demonstrated below. The total bond energy at any oxygen atom can hence be assumed to be predominantly due to the overlap between the orbitals of the high-valent M cations and the 2s, 2p orbitals of oxygen, the Ni–O bond energies accommodating to this situation. Furthermore, the number and the steric arrangement of the M cations in the oxygen coordination sphere will determine the nature of the 2s–2p hybridisation on the oxygen ligator atoms—having in mind, that the bond energy is larger for hybridised than for pure 2p and 2s orbitals [8]. Thus, we anticipate a sp_z hybridisation along the Ge–O bond direction in Ni_2GeO_4, while the two Nb^V atoms with a Nb–O–Nb angle near to 120° enforce a $sp^2_{x,y}$ hybridisation at the oxygen atoms in $NiNb_2O_6$. While ideally oriented sp, sp^2 and sp^3 hybrid orbitals correspond to cationic oxygen coordina-

tions with $D_{\infty h}$, D_{3h} and T_d symmetry, respectively, the presence of different cations and inhomogeneous bond length distributions or angular distortions necessarily leads to symmetry reduction and spectral band splittings. In particular angular distortions induce a directional mismatch between the hybrid orbitals and the Ni–O bond, this phenomenon being well-known as misdirected valence. This concept was introduced by Liehr [9] and later implemented into the AOM formal-
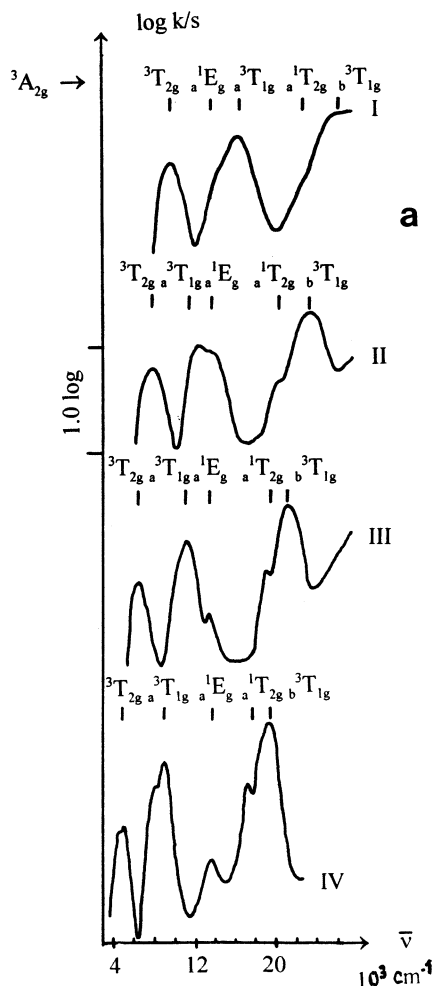

Fig. 1. d–d Reflection spectra of octahedral Ni^{2+} in oxide ceramics (coordination number: upper index in parenthesis): I. $(Zn)^{(4)}(Zn_{0.75}Ni_{0.25}Ge)^{(6)}O_4$ [$\Delta = 9500$ cm^{-1}; $B \approx 860$ cm^{-1}] (spinel); II. $(NiTa_2)^{(6)}O_6$ [$\Delta = 7800$ cm^{-1}; $B = 850$ cm^{-1}] (trirutile); III. $(Ba_{0.25}Sr_{0.75})^{(12)}(Ni_{0.5}Te_{0.5})^{(6)}O_3$ [$\Delta = 6500$ cm^{-1}; $B = 860$ cm^{-1}] (elpasolite); IV. $(Ba)^{(12)}(Ca_{0.45}Ni_{0.05}Te_{0.5})^{(6)}O_3$ [$\Delta = 4900$ cm^{-1}; $B = 870$ cm^{-1}] (elpasolite)— band positions calculated with the given parameters and $C/B = 4.2$ (a) and of tetrahedral Co^{2+} in oxide spinels—band positions (Bethe notation) calculated with: $\Delta = 4100$ (4350) cm^{-1}, $B = 770$ (780) cm^{-1} for I (II); $C/B = 4.5$, $\xi = 750$ cm^{-1} (white standards: Zn(Mg)Ga(Al)$_2$O$_4$ for I (II)) (b).
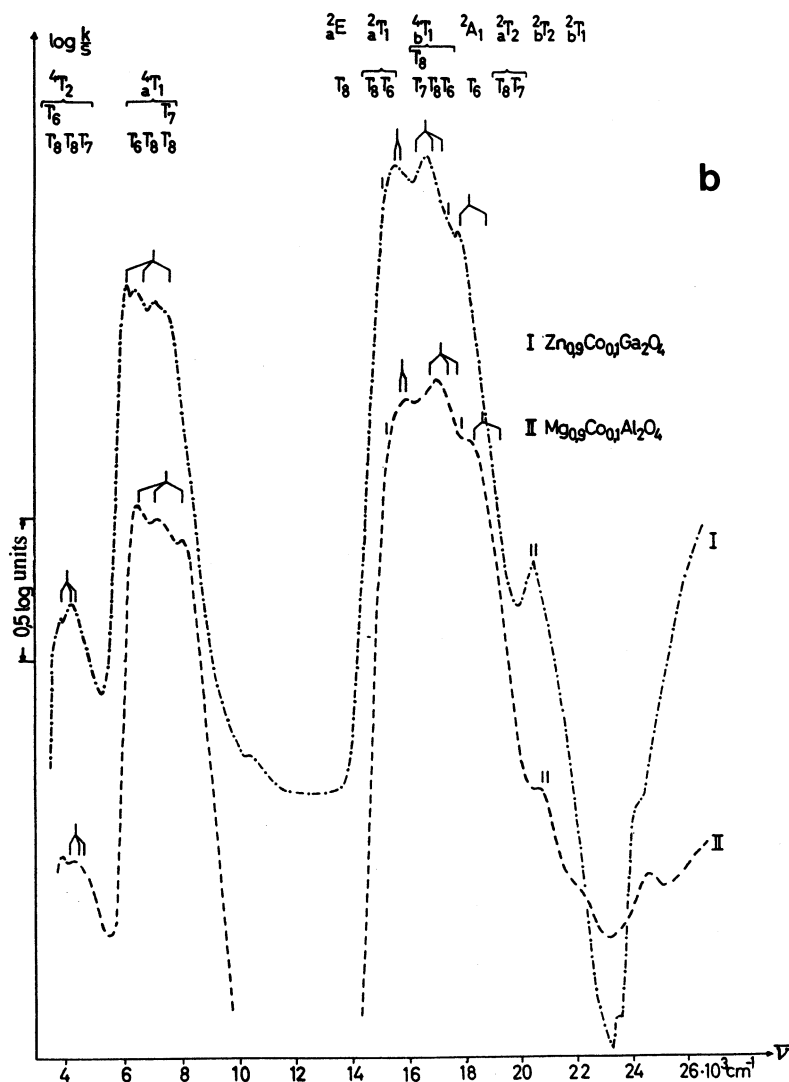
Fig. 1. (*Continued*)

ism by Gerloch et al. [10]. The application to copper(II) and nickel(II) acetylaceto-nate complexes utilising hybrid orbitals turned out to be very effective in analysing the π-bonding anisotropies in these planar entities [11]. The formal use of hybrid orbitals in ligand field theory is elaborated by Kennedy and Schäffer [12]. We employ a similar AOM procedure in this contribution. The main draw-back is an overparametrisation, mostly due to the occurence of non-diagonal AOM energies $e_{\sigma\pi}$, which can be approximated as $(e_{\sigma}e_{\pi})^{1/2}$, however. Though a detailed description of the theory and the calculational procedure underlying our bonding concept will

be published separately [13], the used bonding model is explicitly introduced for each case. The subdivision of the oxygen atoms with their specific cationic environment into the categories sp, sp^2 and sp^3 allows to set up a ligand field model for misdirected bonds, introducing AOM parameters $e_\sigma(sp_z)$, $e_\pi(sp_z)$, $e_\sigma(p_{x,y})$, $e_\pi(p_{x,y})$; $e_\sigma(sp_{x,y}^2)$, $e_\pi(sp_{x,y}^2)$, $e_\pi(p_z)$ and $e_\sigma(sp^3)$, $e_\pi(sp^3)$, respectively.

The usefulness of the proposed bonding concept is demonstrated in the second section. Here cases are discussed, where considerable symmetry splittings in the d–d spectra of octahedral Ni^{2+}, Co^{2+} and Cr^{3+} are observed, which are not reflected by correspondingly large polyhedron distortions. Bonding anisotropies induced by misdirected valence effects of the kind just discussed, however, account nicely for the band splittings.

In Section 3 the variability of the ligand field parameter Δ and of the underlying e_σ and e_π energies in depencence on the geometry and constitution of the cationic oxygen coordination is considered. In particular, the large changes of these parameters when high-valent d^0 configurated cations such as W^{VI}, Nb^V, Ta^V are replaced by the d^{10} cations Te^{VI}, Sb^V are discussed in great detail. Also, in this section the d–d and EPR spectra of Cu^{2+} oxide ceramics are analysed. Because the Jahn–Teller distortion of the CuO_6 octahedra leads to symmetry splittings and anisotropies of the g- and hyperfine tensor components for otherwise highly regular NiO_6 octahedra, one may deduce e_σ and e_π separately from these spectra. Here we approximate the distance dependence of the AOM parameters by Eq. (2) where the S_i are overlap integrals and δ denotes an arbitrary spacing.

$$e_i(\delta) = e_i(\text{oct})S_i(\delta)^2/S_i(\text{oct})^2 \quad (i = \sigma, \pi) \tag{2}$$

The S_i have been calculated for Cu^{2+}, Ni^{2+} and neutral oxygen utilising the quantum chemical data as published in [14]a and [14]b, respectively. Eq. (2) has its origin in the Hückel theory (Wolfsberg–Helmholtz approximation) and is—in a strict sense—theoretically not justified fully. Nevertheless Eq. (2) approximately pictures the experimentally observed effect, that the R^n dependence (R: metal–ligand spacing) of the ligand field parameters is more pronounced than predicted by electrostatic theory ($n = 5$ for cubic crystal fields and $n = 3$ for lower-symmetry contributions). One should keep in mind, however, that e_σ and e_π values resulting from such a procedure (Eq. (2))—which is necessary in order to keep the number of free fitting parameters sufficiently low—is rather approximate for *large* differences in the bond distances.

A further interesting problem concerns the transferability of the AOM parameters between different oxidic solids. The factorisation of the ligand field parameter as proposed by Jørgensen [1,2] (Eq. (1b)),

$$\Delta = f \cdot g \cdot 10^3 \text{ cm}^{-1} \tag{1b}$$

where f and g are the contributions characteristic of a certain ligand grouping with a specific ligator atom and for a specific transition metal ion in a fixed oxidation state, respectively, works rather well within certain limits in very many cases and seems to indicate transferable bonding parameters. However, as Fig. 1 and the respective discussion demonstrates, this is not the case for oxidic solids with widely

interconnected polyhedra and a great variety of cationic coordinations, which strongly differ in the coordination number, the geometry and the constitution. We will show, that the AOM parameters are only transferable from one solid to another, if the bonding situation on the oxygen atoms is very similar in both cases.

In Section 4 the covalency contributions to the transition metal–oxygen bond are considered, as reflected by the Racah' parameters of interelectronic repulsion (for Ni^{2+} and Cr^{3+} as model examples) and by the mixing coefficients α of the 3d participation in the ground state MO of Cu^{2+}, which are accessible by EPR spectroscopy. The results are critically compared with those, which are derived from various other experimental techniques. The deduced arguments are finally used to discuss, whether not only ionic ligands, but more covalent ligator atoms as well are able to stabilise the higher oxidation states of the late 3d transition metals in complexes and solids.

2. Symmetry effects and band splittings by bonding anisotropies

2.1. The spinel lattice

Figs. 2 and 3 show the reflection spectra of the spinels Me_2GeO_4 (Me: Ni^{II}, Co^{II}) and their mixed crystals with Mg_2GeO_4. The latter compound crystallises in the olivine structure, but transforms into the low-temperature spinel modification under pressure [15]. Mixed crystals $Me_{2-x}Mg_xGeO_4$ are stable in the spinel phase under atmospheric pressure up to $x \approx 1.25$ and 1.0 for Me = Ni^{2+} and Co^{2+}, respectively and are characterised by a normal cation distribution, with the Me^{2+} cations residing on octahedral sites of D_{3d} point symmetry and Ge^{IV} on regular tetrahedral sites (T_d) [16]. While the cations occupy special positions, there is one free parameter u for oxygen. The geometry of the hexaoxo-coordinated transition metal ions is regularly octahedral in the case of $u = 3/8$. For Mg_2GeO_4 an u-parameter of 0.3758(5) is reported [15], corresponding to Ge–O and Mg–O bond lengths of 1.80(1) and 2.055(5) Å. Adopting the value of the Ge–O spacing, oxygen parameters of $u = 0.376(0.375)$ are deduced for the spinels Ni_2GeO_4 (Co_2GeO_4), which lie in the range estimated for the two compounds from X-ray powder data (0.375(3) [17]). The calculated Ni–O and Co–O spacings are 2.04_5 and 2.08 Å, respectively, and hence by 1–2% smaller than following from reported ionic radii [18]. The possible tiny positive deviation of 0.01 from the ideal u-value corresponds to a trigonal elongation along the S_6 axis of the MeO_6 octahedra by $\sim 0.6\%$, which is by far too small to explain in particular the large splittings of the highest d–d transitions in Figs. 2 and 3 (3000 cm^{-1}).

In trigonal ligand fields the symmetry splitting of the t_{2g} orbitals into e_g and a_{1g} (higher- and lower-energy split state, respectively) and the non-diagonal energy between $e_g(t_{2g})$ and $e_g(e_g)$ can be described by empirical parameters $3K$ and $\sqrt{2}\,K'$, respectively (Eq. (3)) [19], where a positive sign for K corresponds to a compression along the S_6 axis. Note, that K' is also posivite in this case bearing in mind the appropriate phase relations for the e_g eigenfunctions.

$$3K = E[e_g(t_{2g})] - E[a_{1g}(t_{2g})]$$

$$\sqrt{2}\,K' = -\langle e_g(t_{2g})\,|V_{ax}|\,e_g(e_g)\rangle \tag{3}$$

In terms of simple angular overlap theory one obains the expressions in Eq. (4) for the two trigonal parameters, if only small $\delta\theta$ values are considered.

$$K = 2\sqrt{2}(\delta\theta)e_\pi \qquad K' = 3\sqrt{2}(\delta\theta)e_\sigma \tag{4}$$

Here e_σ and e_π are antibonding AOM energies defined along the Me–O bond directions, while $\delta\theta$ (in radians) denotes the deviation of the angle between the Me–O bond vectors and the S_6 axis (Fig. 4b) from the octahedral value (54°44′). $\delta\theta$

Fig. 2. Diffuse reflection spectra (d–d transitions) of spinel-type mixed crystals $Mg_{2-x}Ni_xGeO_4$. The band assignment is according to D_{3d} symmetry, with the O_h parent terms also given on top. Splittings due to LS-coupling are not shown for the sake of transparency. Calculated energy positions are based on the parameter set in Eq. (7).
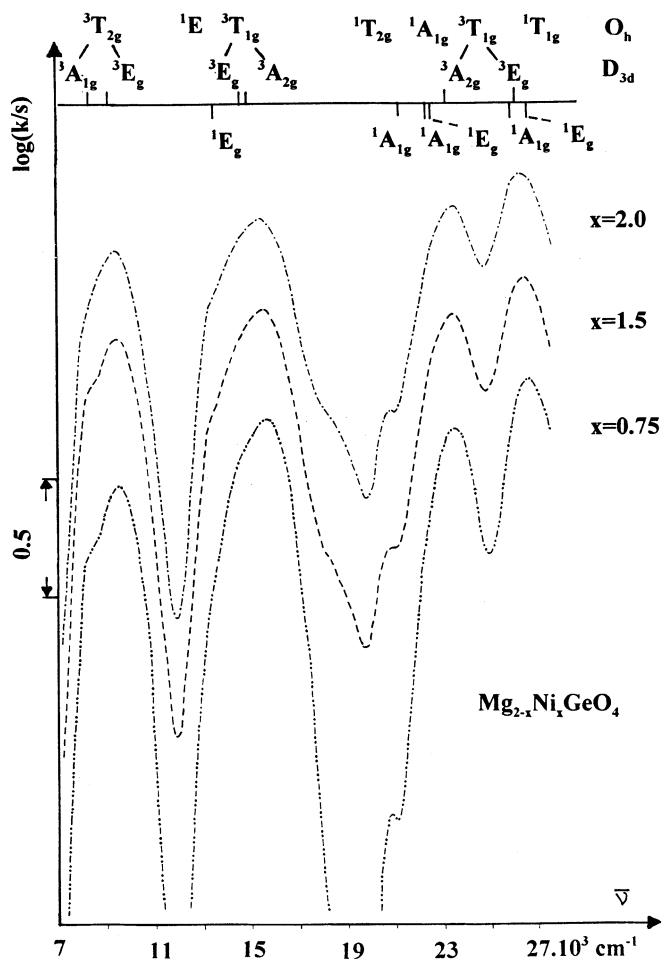
Fig. 3. Diffuse reflection spectra (d–d transitions) of spinel-type mixed crystals $Mg_{2-x}Co_xGeO_4$. The band assignment is according to D_{3d} symmetry, with the O_h quartet parent terms also given on top. Splittings due to LS-coupling are not shown for the sake of transparency. Calculated energy positions are based on the parameter set in Eq. (8).
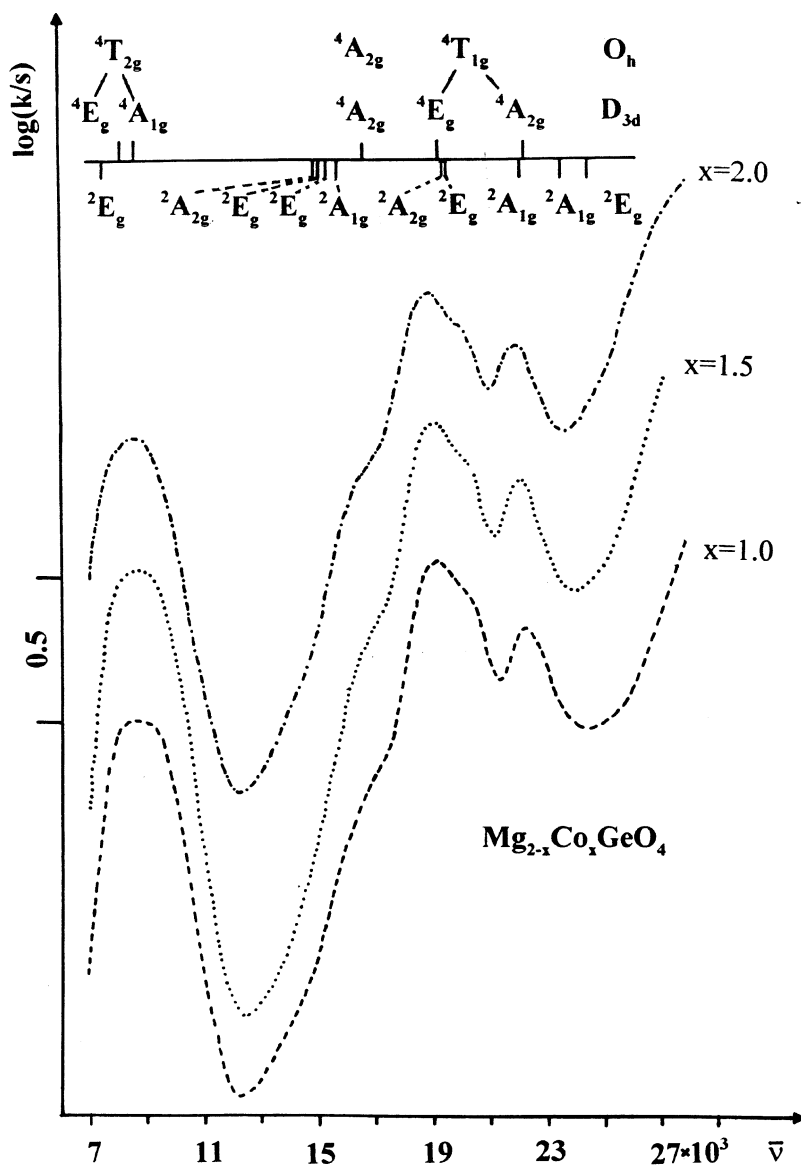
amounts to $\mp 1.0°$ (∓ 0.017 radians) for deviations ± 0.003 from the ideal oxygen parameter u (3/8), yielding rather small values of K (< 50 cm^{-1}) and K' (< 300 cm^{-1}) for e_σ and e_π energies of reasonable magnitudes (see below). However,

parameter values $K \cong 600$ (750) cm^{-1} and K' energies of the same magnitude have to be chosen for $Ni_2GeO_4(Co_2GeO_4)$, in order to account for the observed very distinct band splittings (Figs. 2 and 3) [16], though a definite explanation for the surprisingly large symmetry effect is still lacking. The spectral energies do not change on dilution with Mg^{2+} in the octahedral sites, but the spectral resolution improves somewhat. It is also seen, that the shoulder at $\cong 13000$ cm^{-1} in Fig. 2 has to be assigned to the octahedral $^3A_2 \rightarrow {_a^1}E_g$ transition and not to a split band of the $^3A_2 \rightarrow {_a^3}T_{1g}$ transition, because its intensity drastically reduces on dilution. This phenomenon has been observed in the $Mg_{1-x}Ni_xO$ mixed crystal series as well and is readily explained by cooperative electronic interactions between neighboured NiO_6 octahedra with antiparallel spin orientations, inducing an intensity increase of the spin-forbidden transitions with increasing x [20].

We will now consider possible mechanisms, by which the large band splittings in Figs. 2 and 3 might be explained. The coordination of the oxygen anions is one Ge^{IV} and three Me^{2+} cations (Fig. 4a), the corresponding polyhedron possessing the symmetry C_{3v}. For $u = 3/8$ the Me–O bonds have perpendicular orientations
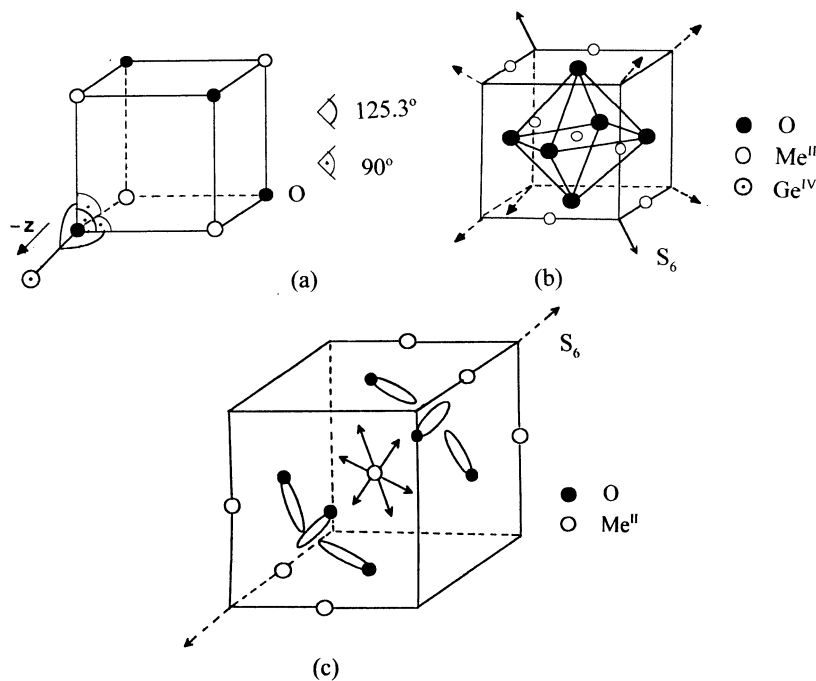
Fig. 4. The spinel structure of Me_2GeO_4 (Me = Ni^{2+}, Co^{2+}; normal cation distribution, ideal oxygen parameter $u = 3/8$): The $Me_4O_4Ge_4$ cluster, only one Ge^{4+} ion is shown (a), the cationic Me^{2+} environment of the oxygen atoms of a MeO_6 octahedron with D_{3d} symmetry [three of the four cube diagonals (hatched arrows) parallel to the six $\pm z$ directions (see Fig. 4a), and the S_6 axis imposed by the space group symmetry are indicated] (b) and the orientations of the sp_z hybrids of each oxygen atom, which extend (bulk arrows) parallel to three of the four cube diagonals (c).

with respect to each other, while the Ge–O bond exhibits angles of 125.3° towards the Ni–O(Co–O) bond vectors. Two limiting bonding concepts seem to be feasible:

a. sp^3 hybridisation of the oxygen ligator atoms, with one hybrid orbital matching with the Ge–O bond direction ($\|\|(-z)$, Fig. 4a),
b. sp$_z$ hybridisation of oxygen, with one hybrid orbital oriented towards Ge^{IV} ($\|\|(-z)$), while the other one points in the opposite direction ($\|\|(+z)$) (Fig. 4a). p$_x$, p$_y$ have orientations perpendicular to z and are available for π-overlap with Ge^{IV} and a mixed $\sigma-\pi$-bonding with Me^{2+}. The sp-hybrid oriented along the $(+z)$ axis also exhibits σ- and π-overlap with the Me^{2+} d-orbitals.

Concept (b) takes into account, that the Ge^{IV}–O overlap represents the dominating bonding effect. The Ni(Co)$^{2+}$ ions adapt to the situation created by Ge^{IV} with the much higher positive charge and corresponds to that sketched in the introductory chapter. In an ionic description Ge^{4+} acts on *one oxygen ion* with the polarising charge $(+1)$, which value is defined as the ratio of the charge and coordination number (C.N. 4) of the respective cation. The *three* Me^{2+} ions (C.N. 6) represent the same charge *in total*, this charge distribution in the GeONi$_3$ polyhedron strongly supporting model (b). Developing the alternative concepts in terms of the angular overlap model (AOM) the expressions in Eqs. (5) and (6) are obtained for the ligand field parameter Δ and the trigonal splitting parameters K, K'. For the sake of simplicity u is chosen to have the ideal value 3/8. Relevant energy determinants are listed in Appendix A, while further calculational details are given elsewhere [13].

The effective d-overlap energies along the Ni–O(Co–O) bonds in the case (a) are represented by the AOM parameters e_σ, e_π in Eq. (5).

sp^3-hybridisation:

$$K = -2e_\pi; \; K' = -\sqrt{3}\,(e_\sigma \cdot e_\pi)^{1/2} \quad e_\sigma = 25/27\; e_\sigma(\text{sp}^3)$$

$$\Delta = 3e_\sigma - 4e_\pi \qquad\qquad\qquad e_\pi = 1/27 e_\pi(\text{sp}^3) \tag{5}$$

The relations to the energies of the sp^3 hybrid functions themselves, which are misaligned with respect to the Ni–O(Co–O) bond directions by about $\alpha \cong 16°$ (Fig. 4a), are also given ($\cos^2 \alpha = 25/27$, see Eq. (5)). A best fit to the spinel-type Mg$_{2-x}$Ni$_x$GeO$_4$ d–d spectra is obtained with the parameter set (Eq. (5a)):

sp^3-hybridisation:

$$e_\sigma(\text{sp}^3) = 3300 \text{ cm}^{-1}, \; e_\pi(\text{sp}^3) = 1500 \text{ cm}^{-1}; \; e_\sigma = 3050 \text{ cm}^{-1}, \; e_\pi = 55 \text{ cm}^{-1}$$

$$(\Delta = 8950 \text{ cm}^{-1}; \; B = 850 \text{ cm}^{-1}) \tag{5a}$$

with C/B fixed at the free ion ratio of 4.2 and a spin–orbit coupling parameter chosen to be 80% of the free ion value ($\xi = 520$ cm^{-1}). While the very pronounced splitting of the $_b^3T_{1g}$ band is approximately reproduced, the splittings of the transitions to the $^3T_{2g}$ and $_a^3T_{1g}$ terms are calculated to be smaller and much larger than observed, respectively (see the calculated and experimental transition energies in Appendix A). Also, the $e_\sigma(\text{sp}^3)/e_\pi(\text{sp}^3)$ ratio (2.2) is unrealistically high. Furthermore, in contrast to the band assignment in this model, the relative intensities of the split bands of the $^3A_{2g} \rightarrow {}^3T_{2g}$ and $\rightarrow {}_b^3T_{1g}$ transitions suggest, that not the lower-, but

the higher-energy components represent the trigonal (doubly orbitally degenerate) ^{3}E split terms. Apparently, negative signs for K and K' (Eq. (5)), which indicate an *effective* trigonal elongation along the S_6 axis, are not appropriate to explain the observed spectra. This apparent elongation is caused by the mismatch (Fig. 4a) between the sp^3 hybrids and the Ni–O bond directions (bent bonds), which introduces small π-contributions into the Ni–O bonds, leading to non-vanishing K and K' values (Eq. (5)). The π-overlap is anisotropic, however, because it involves only three of the four cube diagonals in Fig. 4b, implying stronger π-components parallel than perpendicular to the S_6 axes of the MeO$_6$ polyhedra.

Switching to the alternative bonding model (b) the expressions in Eq. (6) are obtained for the ligand field parameters K, K' and Δ.

sp_z-hybrid; p_x, p_y:

$$K = e_\pi - 2e'_\pi; \quad K' = \sqrt{3}\ \{(e'_\sigma \cdot e'_\pi)^{1/2} - \tfrac{1}{2}(e_\sigma \cdot e_\pi)^{1/2}\}$$

$$\Delta = 3(e'_\sigma + e_\sigma) - 4(e'_\pi + e_\pi) \tag{6}$$

$$e'_\sigma[e'_\pi] = \cos^2(54°44') \cdot e_\sigma(sp_z)[e_\pi(sp_z)]$$

$$e_\sigma[e_\pi] = \cos^2(35°16') \cdot e_\sigma(p_x, p_y)[e_\pi(p_x, p_y)] \tag{6a}$$

Here e'_σ, e'_π are the antibonding AOM energy components along the Ni–O bonds resulting from the 'lone-pair' sp_z-hybrid, while e_σ, e_π are corresponding energy contributions from p_x and p_y (Fig. 4a). The relations to the original AOM parameters ($e_\sigma(sp_z)$, $e_\pi(p_x,p_y)$, $e_\sigma(p_x,p_y)$, $e_\pi(sp_z)$) in the z- and x-, y-coordinate system (defined by the orientation of the sp_z lone-pair), from which the set in Eq. (6) originates, can be taken from the expressions in Eq. (6a), which are discussed below. There are, thus, four free AOM energy variables, while only three ligand field parameters (Δ, K, K') are available. We may estimate the magnitude of $e_\sigma(sp_z)$, however, by utilising the d–d spectra of V^{IV} and Cr^{IV} doped into the tetrahedral Ge^{IV} position of Mg$_2$GeO$_4$ (spinel modification) from which Δ parameters of $\cong 10000$ cm^{-1} can be deduced [21]. Assuming that the AOM energies of these four-valent 3d cations should be about equivalent to those $e_\sigma(sp_z)$ and $e_\pi(p_x,p_y)$ energies, which correspond to the total overlap of the lone pair and of the p-orbitals perpendicular to it with the d-orbitals of the three Ni^{2+} cations (Fig. 4), meaningful fittings to the experimental spectra (Fig. 2) are possible. This consideration follows our concept, that the positive charge of a tetrahedrally co ordinated 3d cation with the oxidation state ($+$IV) acting on each oxygen atom is comparable to that of three divalent 3d cations in octahedral coordination. Using the parameter set in Eq. (7), transition energies in excellent agreement with the observation are obtained.

$e'_\sigma = 3300$ cm^{-1}; $e'_\pi = 290$ cm^{-1}		$K = 590$ cm^{-1}
$e_\sigma = 1600$ cm^{-1}; $e_\pi = 1170$ cm^{-1}		$K' = 510$ cm^{-1}

4900 cm^{-1}	1460 cm^{-1}	($\Delta = 8870$ cm^{-1})

$$B = 850 \text{ cm}^{-1},\ C/B = 4.2;\ \zeta = 520 \text{ cm}^{-1} \tag{7}$$

$$e_\sigma(\mathrm{sp}_z) = 3e'_\sigma = 9900 \text{ cm}^{-1}; \qquad e_\pi(\mathrm{sp}_z) = 3e'_\pi = 870 \text{ cm}^{-1}$$

$$e_\sigma(\mathrm{p}_x,\mathrm{p}_y) = (3/2)e_\sigma = 2400 \text{ cm}^{-1}; \; e_\pi(\mathrm{p}_x,\mathrm{p}_y) = (3/2)e_\pi = 1750 \text{ cm}^{-1} \qquad (7a)$$

Here, $e_\sigma(\mathrm{sp}_z)$ and the $e_\sigma(\mathrm{sp}_z)/e_\pi(\mathrm{p}_x,\mathrm{p}_y)$ ratio ($\cong 5._5$) are calibrated, such that these values match the Δ values of tetrahedral $\mathrm{Cr^{IV}}$ and $\mathrm{V^{IV}}$ cited above ($\Delta = 4/9\{3e_\sigma(\mathrm{sp}_z) - 4e_\pi(\mathrm{p}_x,\mathrm{p}_y)\}$). Fig. 2 gives the assignment up to 26500 cm^{-1}. Energy values for the observed and calculated band positions are listed in the Appendix— this case standing as a model example for many others to be discussed, where only figures with band assignments and calculated transition energies are shown. Taking LS coupling into account does not change the calculated band positions essentially, the additional splittings remaining in the range of the half-width of the bands. All essential spectral features are accounted for. The large e_σ (sp$_z$) energy distributes over the three Ni–O bonds. The total metal-d ligand-s,p overlap energy of σ symmetry (antibonding effect) along the Ni–O bond vectors amounts to nearly 5000 cm^{-1}, while the corresponding π-antibonding energy is about 1500 cm^{-1} (Eq. (7)). As expected the σ-overlap of the sp$_z$ hybrid is more pronounced than that of the p$_x$,p$_y$ orbitals, in contrast to the 3dπ-contributions to the Ni–O bond, where the energetic situation is reverse.

The signs of K and K' indicate an apparent trigonal *compression* of the NiO$_6$ octahedra in this case, which can be verified by inspecting Fig. 4. The sp$_z$ hybrids are aligned parallel to three of the four pseudo-C_3 axes of the cube, circumscribing one MeO$_6$ octahedron—forming tetrahedral angles with the singular S_6 direction, along which the trigonal distortion of the octahedron occurs for u deviating from 3/8. The angles between the sp$_z$ (p$_x$,p$_y$) orbitals and the Me–O bond directions are 54°44′ (35°16′) yielding the relations in Eqs. (6a) and (7a). Projections with the same angles define e'_π and e_π in the same equations. The σ-contributions of the hybrid and p$_x$,p$_y$ orbitals are more pronounced perpendicular than parallel to the S_6 axis, if one bears in mind that $e_\sigma(\mathrm{sp}_z)$ is much larger than $e_\sigma(\mathrm{p}_x,\mathrm{p}_y)$ (Eq. (7a)). Similarly, the π-bonding is more effective perpendicular than parallel to the S_6 symmetry axis ($e_\pi(\mathrm{p}_x,\mathrm{p}_y) > e_\pi(\mathrm{sp}_z)$). Both anisotropic bonding properties indeed correspond to a trigonal compression. The possible additional angular distortion of the octahedra in spinels MMe$_2$O$_4$ for deviations ± 0.003 from the ideal oxygen parameter u (3/8) changes the angle between the sp$_z$ hybrid and the Ni–O bond vector by only $\mp 1.4°$, while the angle MeOM varies by $\delta\theta = \mp 1.0°$ for the same change of u, as has been pointed out before. These small deviations of the OMeO bond angles from 90° do not affect the energies of the 3d–3d transitions in the optical spectra significantly. The main structural influence of a variation of u is to adjust the sizes of the tetrahedral and octahedral interstices to the ionic radii of the metal ions. The hypothetical choice of a p$_z$ orbital instead of the sp$_z$ hybrid with a bonding capacity equal to that of p$_x$ or p$_y$, will cause vanishing K and K' energy values ($e_\sigma = 2e'_\sigma$, $e_\pi = 2e'_\pi$ in Eq. (6)) as expected.

An equally very good spectral fit is possible for Co$_2$GeO$_4$ (Fig. 3) within model (b) (see Appendix A) applying the parameter set of Eq. (8). As expected for

3d-cations of the same charge and directly neighboured in the periodic table the AOM parameters are very similar to those for Ni_2GeO_4 (Eq. (7)). The differences in their magnitudes should be considered as being mainly due to the error width in the fitting procedures.

$$e'_\sigma = 3600 \text{ cm}^{-1}; \quad e'_\pi = 450 \text{ cm}^{-1} \qquad\qquad K = 300 \text{ cm}^{-1}$$

$$e_\sigma = 1500 \text{ cm}^{-1}; \quad e_\pi = 1200 \text{ cm}^{-1} \qquad\qquad K' = 1045 \text{ cm}^{-1}$$

$$\underline{\qquad\qquad\qquad\qquad\qquad\qquad\qquad\qquad\qquad\qquad\qquad\qquad\qquad\qquad}$$

$$5100 \text{ cm}^{-1}; \quad 1650 \text{ cm}^{-1} \qquad\qquad (\Delta = 8700 \text{ cm}^{-1})$$

$$B = 800 \text{ cm}^{-1}, \ C/B = 4.5; \ \xi = 430 \text{ cm}^{-1} \tag{8}$$

However, in the case of Co_2GeO_4 the σ-anisotropy seems to be slightly more pronounced and the π-anisotropy less distinct than for the d^8-configured Ni^{2+} centre in the same host compound.

$NiGa_2O_4$ is a spinel with a nearly inverse cation distribution, which implies that half of Ga^{3+} occupies the tetrahedral sites and equal amounts of Ni^{2+} and Ga^{3+} are found in octahedral coordination. The cationic coordination of oxygen is hence approximately $Ga^{(4)}O(Ni_{1/2}Ga_{1/2})_3^{(6)}$, the upper indices in parentheses giving the respective coordination numbers. One might suggest, that not necessarily model (b) is the appropriate bonding description anymore because the polarising charge from the tetrahedral Ga^{3+} ions acting on each oxygen atom ($+0.75$) is distinctly smaller than that from the three Ni^{2+} and Ga^{3+} cations in the opposite direction ($+1.25$). Indeed the optical spectra of mixed crystals between Ni_2GeO_4 and $NiGa_2O_4$ exhibit decreasing band splitting effects with increasing $NiGa_2O_4$ concentration [16]. Apparently a sp^3 hybridisation at the oxygen ligator atoms becomes increasingly important. Because the positional oxygen parameter u is distinctly larger than $3/8$ (0.3825) for the similar spinel $MgGa_2O_4$ [22], which leads to by about 2.4° smaller MOMe angles (toward sp^3 hybridisation), the structural situation supports the bonding anisotropy effect in this case.

A similar oxygen parameter (0.381(2)) is reported for the spinel Zn_2SnO_4 with an inverse cation distribution and hence a cationic oxygen coordination $Zn^{(4)}O$ $(Zn_{1/2}Sn_{1/2})_3^{(6)}$ [23], which suggests four equal polarising charges of $+1/2$. The d–d spectrum of $ZnNiSnO_4$ (Fig. 5) shows very weak features of the characteristic tetrahedral $^3_aT_1 \rightarrow {}^3T_2$ and $\rightarrow {}^3_bT_1$ transitions of Ni^{2+} at about 4500 cm^{-1} and superimposing the band around 15000 cm^{-1}, respectively, if the solid is quenched from 1100°C, as can be deduced from the comparison with the spectrum of a Ni^{2+}-doped phenakite-type solid, where only tetrahedrally coordinated cations occur. Slow cooling to 400°C, however, leads to a complete migration of Ni^{2+} into the octahedral positions, which is due to the more pronounced octahedral site preference of the d^8 (Ni^{2+}) in comparison with the d^{10} (Zn^{2+}) cation. Though the rather broad spectrum looks cubic at the first sight, an octahedral band fitting is not practicable. Similarly the sp_z model does not work, as is easily seen when considering the large splitting of the highest-energy band in the Ni_2GeO_4 spectrum. However, a fitting on the basis of a sp^3 hybridisation is successful (Fig. 5), which
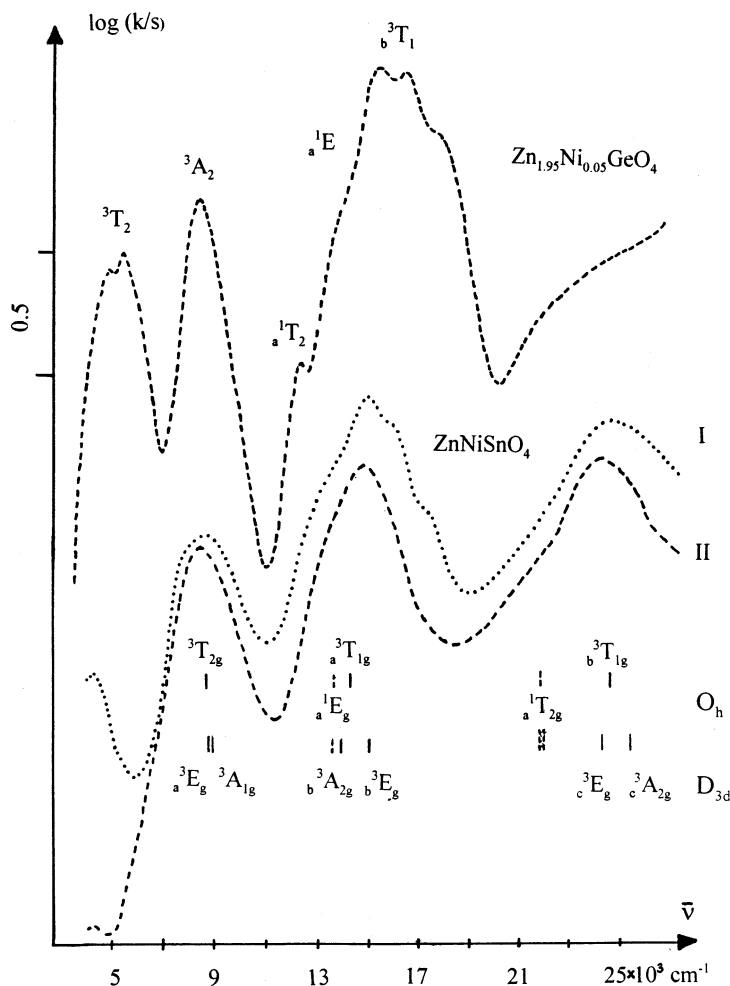
Fig. 5. Powder reflectance spectra of Ni^{2+}-doped Zn_2GeO_4 (phenakite lattice; white standard: MgO; band assignment in T_d) and of $ZnNiSnO_4$ (spinel structure; white standard: the Zn_2SnO_4 host lattice). I and II correspond to solids quenched and slowly cooled to 400°C from the sintering temperature of 1100°C, respectively; band positions were calculated for II with $B = 850$ cm^{-1}, $C/B = 4.2$ and: $\Delta = 8700$ cm^{-1} in O_h; $e_\sigma(sp^3) = 3200$, $e_\pi(sp^3) = 600$ cm^{-1} ($e_\sigma = 2950$, $e_\pi \cong 25$ cm^{-1}) in D_{3d} ($_a^3A_{2g}$ ground state).

is in accord with the effective charge distribution in the cationic oxygen coordination. Support for the assignment also comes from the observation, that the very distinct lower-energy shoulder of the $^3A_{2g} \rightarrow _a^3T_1$ transition remains intense at lower Ni^{2+} concentrations; it is hence obviously caused primarily by a symmetry splitting rather than by the spin-forbidden $^3A_{2g} \rightarrow {}^1E_g$ transition. The rather broad spectral appearence should be led back to the statistical occupancy of the octahedral sites by Sn^{IV} and Ni^{2+}.

The optical spectra of mixed crystals $MgAl_{2-x}Cr_xO_4$ with a normal cation distribution display the typical pattern of octahedrally oxo-coordinated Cr^{3+} with the lowest-energy band centred at $\Delta \cong 18000$ cm^{-1} and the $^3A_2 \rightarrow\, ^3_bT_1$ transition covered by charge-transfer absorption [24] (Fig. 6). The second spin-allowed transition is distinctly split by about 2000 cm^{-1}, as is that for a spinel with Mg^{2+} partly substituted by Cd^{2+}. From the performed AOM fitting calculations those on the basis of a sp_z hybridisation are not appropriate to reproduce the observed spectral features because they always yield larger splittings for the $^3A_{2g} \rightarrow\, ^3T_{2g}$ compared to the $^3A_{2g} \rightarrow\, ^3_aT_{1g}$ transition (see Fig. 2). Recalling that the $Mg^{(4)}OCr_3^{(6)}$
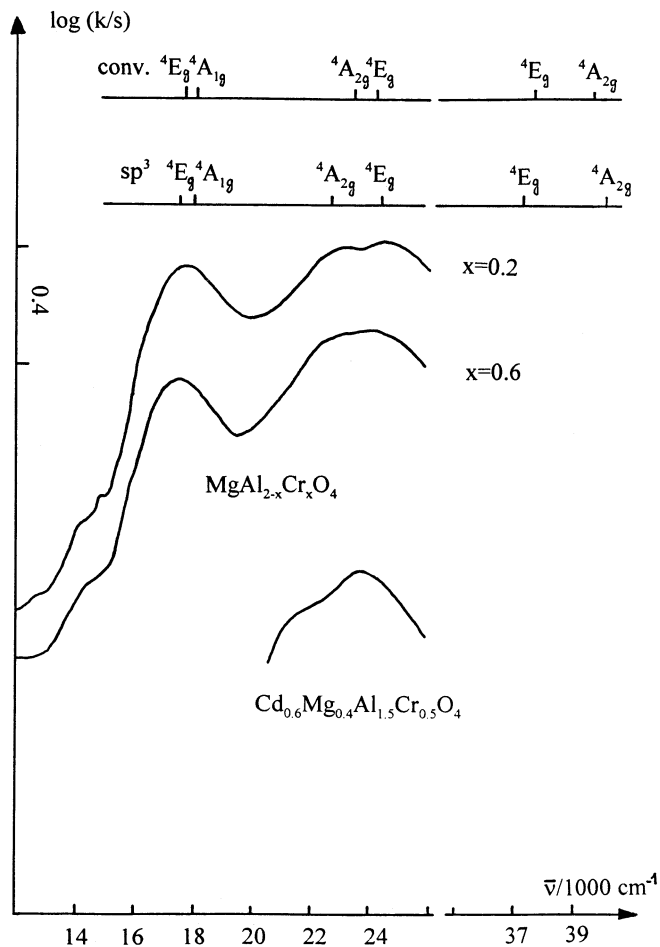

Fig. 6. Diffuse reflection spectra of spinel mixed crystals $MgAl_{2-x}Cr_xO_4$. Calculated band positions (for $x = 0.2$; D_{3d} symmetry) were based on the fitting parameters $B = 600$ cm^{-1} and: $e_\sigma = 5e_\pi = 8200$ cm^{-1} and $u = 0.381$, conventional AOM calculation; $e_\sigma(sp^3) = 6500$, $e_\pi(sp^3) = 2950$ cm^{-1} and $u = 3/8$ [sp^3]. The $^3A_2 \rightarrow\, ^3_aT_1$ transition for the solid $Cd_{0.6}Mg_{0.4}Al_{1.5}Cr_{0.5}O_4$ (with a smaller Δ parameter) is shown in addition.

coordination implies four ($+1/2$) polarising charges acting on the oxygen ligator atoms (as in ZnNiSnO$_4$) the sp^3 model is expected to be the better choice. This is indeed the case (Fig. 6), but a conventional-type AOM calculation with an estimated positional parameter $u = 0.381$ yields similar results, though less pronounced band splittings. Presumably both, the sp^3-type bonding anisotropy and the geometrical D_{3d} distortion, contribute to a distinct effective trigonal elongation of the CrO$_6$ octahedra.

We conclude this section by stating, that the large band splittings observed in the d–d spectra of Ni$_2$GeO$_4$(Co$_2$GeO$_4$) can be traced back to a local symmetry reduction due to bonding anisotropies, which are induced by sp$_z$ hybridisation on the oxygen atoms. Structural and spectral evidence has been accumulated to support such a bonding concept. Though the absolute magnitudes of the derived AOM parameters (Eqs. (7), (7a) and (8)) might be subject to uncertainties—there are four fitting parameters, from which one is adjusted by using experimental data from V^{IV} and Cr^{IV} doped Mg$_2$GeO$_4$—the bonding concept seems to be essentially correct. In most spinels the charge distribution in the oxygen coordination sphere is different, however, approximating four equal effective cationic charges in pseudotetrahedral arrangement, as in ZnNiSnO$_4$ for example. Here a sp^3 hybridisation is the appropriate bonding description, with less bonding capacity from oxygen left for Ni^{2+} in comparison with the situation in Ni$_2$GeO$_4$, which is due to the different cation distribution. This is reflected (Table 7) by the much lower e_σ energy in the case of ZnNiSnO$_4$ ($e_\sigma \approx 3000$ cm^{-1}), though the Δ value equals that of Ni$_2$GeO$_4$ ($e_\sigma \approx 5000$ cm^{-1}). Evidence for a bonding anisotropy of the discussed type is also found in the d–d spectra of spinel mixed crystals with Cr^{3+}.

2.2. The olivine structure

While the spinel lattice is based on a cubic close packing of anions, olivine type solids (space group Pnma)—such as Ni$_2$SiO$_4$ and Mg$_2$SiO$_4$ [25]—consist of approximately hexagonally close packed anion layers. There are two different octahedral sites and three different oxygen atoms in the unit cell. Interatomic distances and angles [26] are collected in Table 1 for the compound LiNiPO$_4$, where the two octahedral sites with C_i and C_s symmetry are occupied by Li$^+$ and Ni^{2+}, respectively. A solid of this constitution is chosen, in order to observe the Ni^{2+} spectrum of only one octahedral site (Fig. 7), without being disturbed by spectral superpositions. The NiO$_6$ polyhedron and the cationic coordination of the oxygen atoms are depicted in Fig. 8, the involved angles can be taken from Table 1. As in the spinel case a sp$_z$ hybridisation on the oxygen atoms is certainly also appropriate, because the high-valent and small P^V ion will dominate the bonding on the O1, O2 and O3 atoms. While the Ni–O1(O2)–P and Nib–O3–P angles are similar to the Ni–O–Ge angle in Ni$_2$GeO$_4$, the situation is different for the Nia–O3–P angle in the P(O3)Ni$_2$Li polyhedron. It is approximately rectangular ($\cong 94°$), implying that the 3dσ contribution to the Nia–O3 (Ni–O3′) bond originates nearly exclusively from the p$_{x(y)}$ orbital of oxygen without a significant sp$_z$ participation.

Table 1
Selected interatomic distances (Å) and angles (°) for LiNiPO$_4$ with the olivine structure[a] [26]

Interatomic distances (Å)			
O1–Ni	2.092(3)	O3'–Ni	2.143(2) [2x]
O2–Ni	2.040(3)	O3–Ni	2.049(2) [2x]

Interatomic angles (°)			
O1–Ni–O3'	85.05(10) [2x]	Li–O1–Li	86.06(12)
O1–Ni–O3	89.39(7) [2x]	Ni–O2–P	128.7(2)
O2–Ni–O3'	97.02(10) [2x]	Ni–O2–Li	122.53(10) [2x]
O2–Ni–O3	89.22(8) [2x]	P–O2–Li	91.51(13) [2x]
O3'–Ni–O3'	69.05(11)[b]	Li–O2–Li	89.36(13)
O3–Ni–O3	113.46(13)[c]	Nia–O3–P	93.77(11)
O3–Ni–O3'	88.54(5) [2x]	Nib–O3–P	126.01(14)
	152.27(10) [2x]	Nia–O3–Li	94.29(9)
O1–Ni–O2	177.48(12)	Nib–O3–Li	114.33(10)
Ni–O1–P	124.6(2)	P–O3–Li	89.29(10)
Ni–O1–Li	95.24 (12) [2x]	Nia–O3–Nib	128.93(9)
P–O1–Li	123.02(12) [2x]		

[a] For nomenclature see Fig. 8.
[b] The angle in Ni$_2$SiO$_4$ is 73.53(7)°.
[c] The angle in Ni$_2$SiO$_4$ is 107.39(8)°.

Because the polarising charge acting on the oxygen atoms by P^V ($+1.25$) is much larger and the (average) one represented by Ni^{2+} and Li$^+$ ($+0.75$) distinctly smaller than in the case of Ni$_2$GeO$_4$, an $e_\sigma(sp_z)$ parameter is expected, which is strongly reduced with respect to that in Eq. (7a). We suggest an energy value, which corresponds to a trivalent 3d metal ion in tetrahedral coordination with the same polarising charge of $+0.75$ as that of the Ni^{2+} and Li$^+$ environment of oxygen in LiNiPO$_4$. For the Fe^{III}O$_4$ tetrahedra in the garnet Y$_3$Fe$_5$O$_{12}$ a Δ-value of $\cong 6200$ cm^{-1} is reported [27], which was used as a rough adjusting energy for the parameter set in Eq. (9). The latter set—defined for an averaged Ni–O spacing of 2.086 Å—implies a tetrahedral Δ of 6650 cm^{-1} and an $e_\sigma(sp_z)/e_\pi(p_x,p_y)$ ratio of about 5 and provides an excellent fit to the observed spectra (Fig. 7).

$$e_\sigma(sp_x) = 6700 \text{ cm}^{-1}; \quad e_\pi(sp_z) = 485 \text{ cm}^{-1}$$

$$e_\sigma(p_x,p_y) = 3000 \text{ cm}^{-1}; \quad e_\pi(p_x, p_y) = 1280 \text{ cm}^{-1}$$

$$e_\sigma(\text{Ni–O}) \cong 3970 \text{ cm}^{-1}, \quad e_\pi(\text{Ni–O}) \cong 1000 \text{ cm}^{-1}$$

$$\Delta \cong 7900 \text{ cm}^{-1}; \ B = 920 \text{ cm}^{-1}; \ C/B = 4.2 \tag{9}$$

The involved structural angles and spacings are properly taken into account, the latter by using tabulated overlap integrals (Eq. (2)). As anticipated from intuitive reasoning, the 'octahedral' AOM parameters (Eq. (9)) defined along the Ni–O bonds are essentially smaller than those of Ni$_2$GeO$_4$. A further interesting feature is, that the contribution of the Nia–O3 ($=$ Ni–O3') overlap to the average e_σ(Ni–O) energy is much smaller ($\cong 425$ cm^{-1}) than that of each of the four other Ni–O

bonds ($\cong 770(80)$ cm^{-1}). This is even the case, if the calculation is performed on the basis of equal Ni–O spacings, so that we may consider the distinctly longer Ni–O3′ distances as being caused by the much more pronounced (but also distinctly weaker—see Eq. (9)) $3d\sigma$-interaction with the $p_{x(y)}$ ligand orbital in comparison with that of the sp_z hybrid. Because of the steric situation (Fig. 8a, Table 1) the latter has only a negligibly small projection along the Ni–O3′ bond direction. It should finally be noted that, as in the spinel case, a conventional-type AOM calculation is not able to reproduce in particular the large splitting of the $^3A_{2g} \rightarrow {}^3_bT_{1g}$ band in the spectrum of Ni^{2+}-doped LiMgPO$_4$ (Fig. 7).

We conclude that the spectra of olivine-type solids can be understood principally when applying the same bonding concept as that used for compounds with the spinel structure. However, while in the latter case the bonding situation is easy to survey due to the cubic structure and a cationic oxygen coordination with C_{3v} symmetry, the olivine lattice is only orthorhombic and the oxygen coordinations are of C_s symmetry (O1, O2) or even lack any symmetry element (O3). The above mentioned correlation between angular distortions and bond length changes such that oxygen orbitals, which are misdirected with respect to the Ni–O bonds, induce
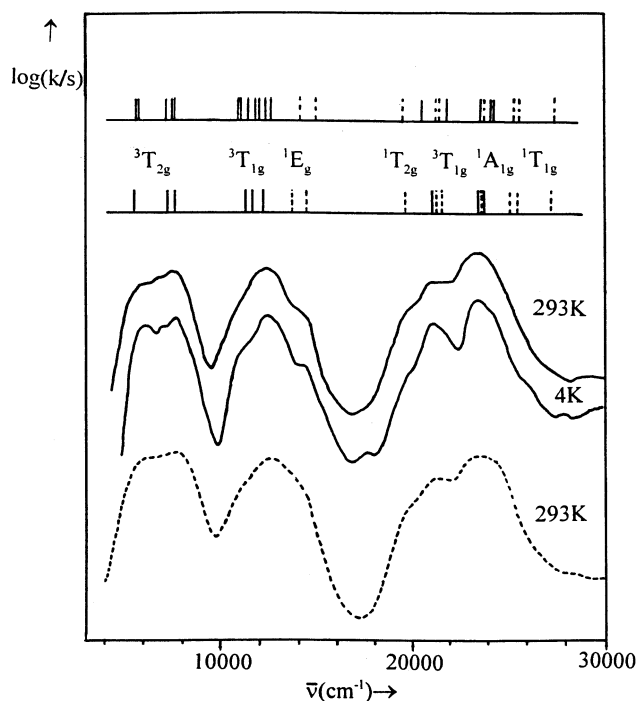

Fig. 7. Powder reflection spectra of olivine-type mixed crystals LiMg$_{1-x}$Ni$_x$PO$_4$ with $x = 0.03$ and $x = 1.0$ (dotted spectrum). The fitting parameters are those of Eq. (9); the assignment (singlets: dottet lines) gives the octahedral parent terms. The calculated transition energies on top include LS coupling ($\xi = 665$ cm^{-1}).
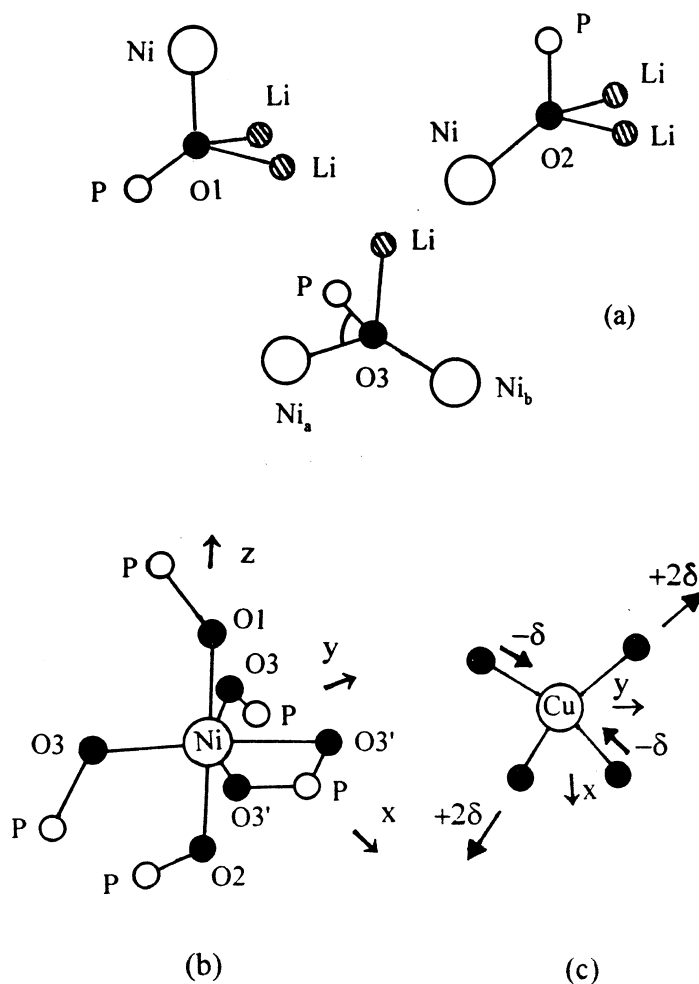
Fig. 8. (a) The cationic coordinations of the oxygen atoms in $LiNiPO_4$, site symmetries C_s (O1,O2) and C_1 (O3); and (b) the geometry of the NiO_6 octahedron (C_s symmetry, xz defines the mirror plane), with the orientations of the P(V) centres bonded to oxygen additionally illustrated; (c) depicts the equatorial xy plane of (b), showing the presumable geometrical changes, if Cu^{2+} is substituted into the octahedral site (changes $\|z$ for Cu–O1, Cu–O2: $-\delta$). The nearly rectangular P-O3–Ni angle in (a) is marked.

a weaker overlap and hence longer spacings, is an interesting feature of low-symmetry systems. It is problematic, however, as well, because it might be erroneous to *fully* account for *both effects* in the calculations. In spite of this draw-back the model seems to work astonishingly well.

It is also possible to dope the Jahn–Teller cation Cu^{2+} into the Mg^{2+} position of $LiMgPO_4$, yielding the nicely resolved EPR spectra of Fig. 9 and the d–d spectra in Fig. 10. Adopting the AOM parameters of Ni^{2+} in $LiMgPO_4$ (Eq. (9)) and the
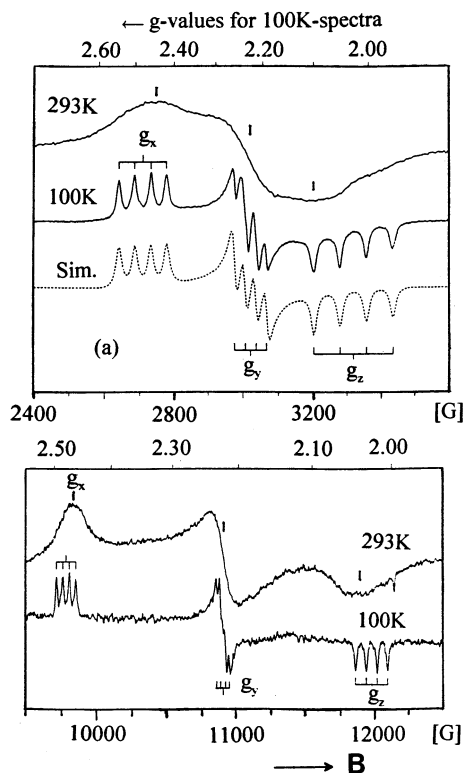
Fig. 9. EPR spectra of Cu^{2+}-doped (0.5 mol%) $LiMgPO_4$; X- and Q-band above and below. The g- and hyperfine components from the simulations are: $g_x = 2.480$, $g_y = 2.22_5$, $g_z = 2.02_6$ and $A_x = -53.3$, $A_y = -31.2$, $A_z = 72.8 \times 10^{-4}$ cm^{-1}.

Table 2
g-Values and ligand field transitions of Cu^{2+}-doped $LiMgPO_4$ (approximate D_2 symmetry, octahedral parent terms in parentheses; ground state $^2A_1$ (^2E_g); in 10^3 cm^{-1}); experimental values, calculated values with the AOM parameters (Eq. (9))[a] and values deduced from a modified AOM calculation[b]: 2nd, 3rd and 4th column, respectively

g_x	2.48_0	2.47_5	2.48_3[c]
g_y	2.22_5	2.31_3	2.22_9[c]
g_z	2.02_6	2.00_1	2.01_9
$\bar{g}$	2.24_4	2.26_3	2.24_4
$\rightarrow {}^2A_1$ (^2E_g)	5700	3200	5120
$\rightarrow {}^2B_1$ $(^2T_{2g})$	$\simeq 9500$	7910	8680
$\rightarrow {}^2B_2$ $(^2T_{2g})$	$\simeq 9500$	8920	10240
$\rightarrow {}^2B_3$ $(^2T_{2g})$	10800	10050	11260

[a] $\zeta = 720$ cm^{-1}; $k = 0.83$.

[b] With an additional compression of the M(II)–O1, M(II)–O2, of one M(II)–O3 and one M(II)–O3′ spacing by $\delta = 0.03$ Å; elongation of the remaining bond lengths by $2\delta = 0.06$ Å (see Fig. 8b,c and Table 1).

[c] Rotation of g_x and g_y toward the Cu–O bond lengths by 26° (see text).
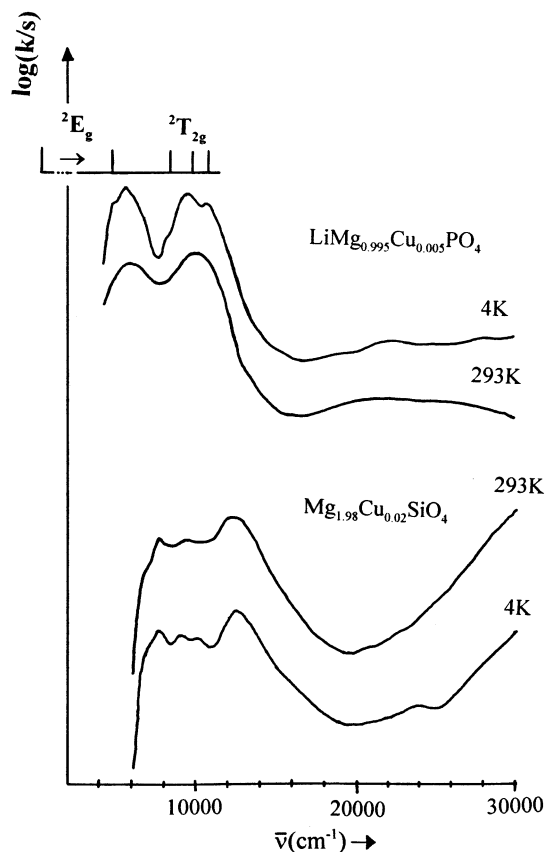
Fig. 10. d–d Spectra of Cu^{2+}-doped (0.5 mol%) $LiMgPO_4$ (assignment and calculated transition energies according to Table 2, column 4) and of Cu^{2+} (2 mol%) in the two Mg^{2+} sites (C_s, C_i) of Mg_2SiO_4.

involved geometries as given in Fig. 8 and Table 1 for the neighbour in the periodic table Cu^{2+} as well, the g-values and ligand field transitions collected in Table 2 are calculated and compared with the experimental values (columns 3 and 2, respectively). The g-tensor components nicely reflect the host site geometry, which is essentially a tetragonal compression, but, due to the pronounced angular distortion in the $Ni(O3)_2(O3')_2$ plane (Fig. 8c, Table 1), with a distinct orthorhombic distortion component superimposed. Only a rough correspondence between experimental and calculated values is observed, however. The main discrepancies are calculated d–d transitions, which are too low in energy, and an orthorhombic splitting g_x-g_y of the g-tensor components, which is much more pronounced in the experiment. Both observations can be accounted for by superimposing a Jahn–Teller distortion component, corresponding to a tetragonal elongation along either one of the two O3–Cu–O3' directions, on the host polyhedron. Such a model reflects the chemical experience. If a host site strain is present, which is essentially a tetragonal

compression, the additional vibronic coupling modifies the geometry in the plane of the longer spacings usually in the way shown in Fig. 8c [28]. Indeed a rather good agreement between experiment and AOM calculation is achieved by this simple approach, if a δ change of 0.03 Å is chosen (Table 2, column 4). In particular the g-values, which are of high accuracy, are nicely reproduced, proving that the bonding concept is essentially correct. The g-tensor components g_x and g_y, which follow the host site symmetry (Fig. 8c) in the first AOM calculation (Table 2, column 3), are rotated towards the Cu–O3 (O3′) bonds, if the vibronic effect is taken into account. Now g_x forms angles of $\pm 26°$ with the molecular x-axis, thus locally violating the point symmetry (xz mirror plane). The superimposed Jahn–Teller distortion component is surprisingly small, suggesting a non-flexible MO_6 polyhedron geometry. This is indeed reflected by the rigid
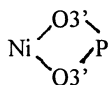
arrangement (Fig. 8b) with a common edge between the octahedron and the PO_4^{3-} tetrahedron, and also supported by the observation, that only a doping level of less than 3 mol% of Cu^{2+} is tolerated on the Mg^{2+} site in $LiMgPO_4$. A conventional AOM calculation cannot reproduce the experimental results even approximately.

Turning to Cu^{2+}-doped Mg_2SiO_4, where both octahedral sites can be occupied by the Jahn–Teller cation, a more complex EPR spectrum is observed (Fig. 11), which can be resolved into a strongly orthorhombic and an approximately tetragonal spectrum (Eq. (10)).

$$(C_i) \qquad g_x = 2.39_2, \ g_y = 2.14_5, \ g_z = 2.03_1; \ \bar{g} = 2.18_9$$

$$A_x = -95, \ |A_y| \cong 10, \ A_z = 55 \times 10^{-4} \ cm^{-1}$$

$$(C_s) \qquad g_\parallel \approx 1.99, \ g_\perp \approx 2.32_5; \ \bar{g} \approx 2.21_3$$

$$|A_\parallel| \approx 148, \ |A_\perp| \approx 20 \times 10^{-4} \ cm^{-1} \tag{10}$$

Our calculations suggest, that the latter is most probably that corresponding to the octahedral C_s site. Because the angular distortion in the equatorial $Ni(O3)_2(O3′)_2$ plane is less pronounced than in the case of $LiNiPO_4$ (Table 1, footnotes), the polyhedron remains in the tetragonally compressed host site geometry on substitution by Cu^{2+}, as reflected by the g-value sequence $g_\perp > g_\parallel \cong g_o$ (2.0023) in comparison with the strongly orthorhombic g-tensor for Cu^{2+}-doped $LiMgPO_4$ (Table 2). The lower averaged g-value indicates a stronger Jahn–Teller coupling than in the $LiMgPO_4$ host, and hence, a distinctly increased tetragonal compression with respect to that of the host polyhedron, which is also reflected by a higher-energy shift of the d–d transitions (Fig. 10).

The g-values of Cu^{2+} in the C_i site are characteristic of essentially elongated octahedra ($g_x > g_y \approx g_z > g_o$), in agreement with host polyhedra, which are already in such a geometry (Fig. 12). The orthorhombic symmetry component has its origin
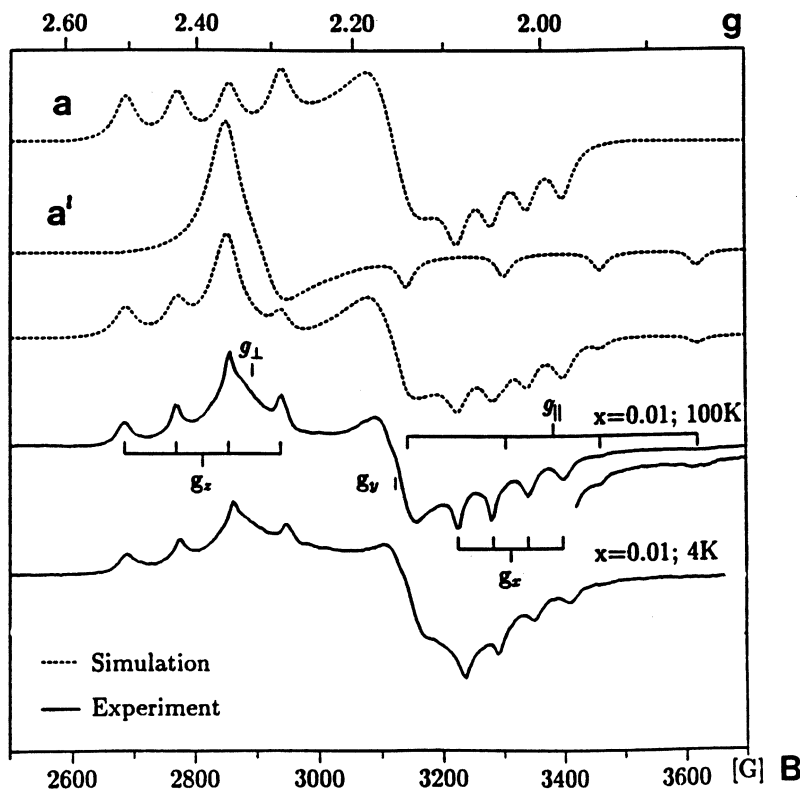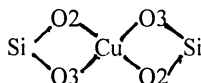
Fig. 11. X-band EPR spectra of Cu^{2+}-doped (1 mol%) Mg_2SiO_4. The simulated spectrum is constructed by the superposition of the a and a' spectra with the intensity ratio 1.4 (dotted lines).

in the distinct angular distortion in the

plane with O2–Cu–O3 angles of $\cong 75°$ and $\cong 105°$. The small averaged g-value indicates a large Jahn–Teller induced distortion component superimposing the host site elongation and is responsible for the higher-energy part of the d–d spectrum (Fig. 10).

Finally the d–d spectra of mixed crystals $Mg_{2-x}Ni_xSiO_4$ are displayed in Fig. 13. Utilising the spectrum of Ni^{2+} in the octahedral C_s site of $LiMgPO_4$ (Fig. 7) we can readily discuss the spectral changes with increasing Ni^{2+} concentration. At small x-values the intensity of the higher energy transitions dominates. They should be due to the C_i site with the slightly smaller average Mg–O spacings (2.096 Å [25]). With increasing x-values the lower-energy parts of the three absorption regions become more intense, in particular at $x > 1.0$, indicating the occupancy of the C_s position with the longer Mg–O bonds (2.130 Å [25]). A preference of Ni^{2+} for the C_i site has been deduced and claimed from crystallographic [25] and spectroscopic
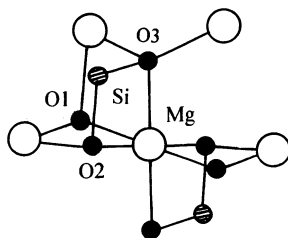
Fig. 12. The geometry of the C_i octahedron in Mg_2SiO_4, depicting the bridging between the SiO_4 and MgO_6 polyhedra via common O2/O3 edges (Mg–Oi spacings: 2.09, 2.07, 2.13 Å for $i = 1$, 2 and 3, respectively [25]).

data [29] already before. The same arguments hold for Co^{2+}, as has been shown convincingly in a very careful spectroscopic study by Schmitz–DuMont and Friebel [30].

The preceding discussion of the spectra of Ni^{2+}- and Co^{2+}-doped olivines has demonstrated, how useful even approximate AOM considerations of the kind proposed can be for the characterisation of bonding properties, vibronic coupling effects or site preferences.
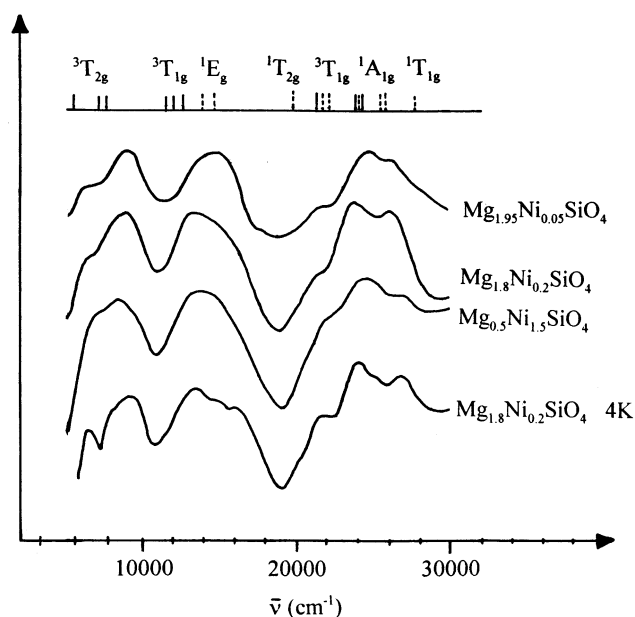
Fig. 13. d–d Reflection spectra (298 K) of Ni^{2+} on the octahedral C_s and C_i sites of Mg_2SiO_4. The calculated energy positions are those due to Ni^{2+} on the Mg^{2+} site (C_s) in $LiMgPO_4$ (Fig. 7). The 4 K spectrum of $Mg_{1.8}Ni_{0.2}SiO_4$ in high resolution is shown below. The intensity corresponds to $\log k/s$ for the 4 K and to reflectivity for the 298 K spectra.
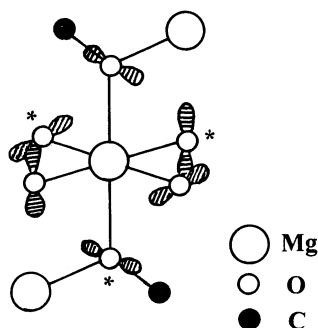
Fig. 14. The MgO_6 polyhedron in $MgCO_3$. The cationic oxygen coordination is partly shown, and the orientations of the oxygen 2p orbitals perpendicular to the $COMg_2$ planes are indicated. Either three of them are connected by the rotation around the C_3 axis (see markings).

2.3. The calcite structure

$MgCO_3$ and $NiCO_3$ crystallise in the calcite structure (space group Cm), which is based on a strongly distorted hexagonal close-packing of oxygen ions and contains trigonal-planar CO_3^{2-} anions. Fig. 14 depicts the coordination geometry of the $Mg^{2+}(Ni^{2+})$ octahedra, with equal Ni–O spacings (2.07_5 Å) but a very small
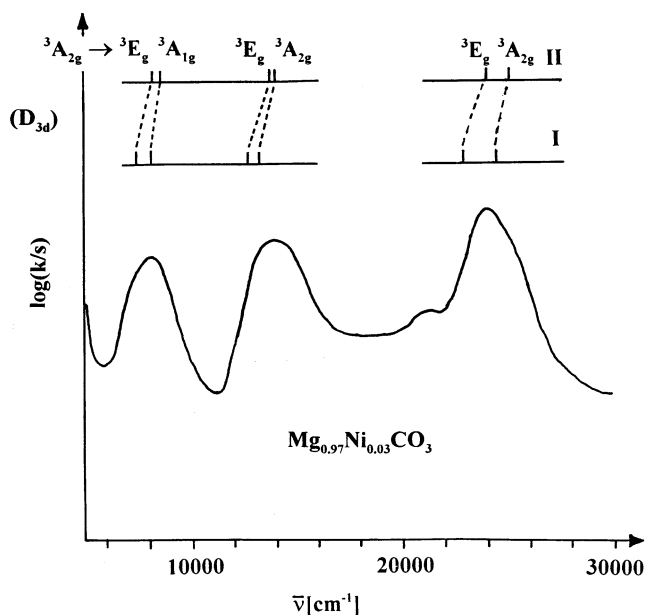
Fig. 15. The powder reflection spectrum of Ni^{2+}-doped $MgCO_3$ (3 mol%). Assignments (symmetry notations for a local D_{3d} point group) and calculated band positions: I. with the AOM parameters in Eq. (9); II. with a reduced $e_\pi(p_x, p_y)$ energy of 1000 cm^{-1}; $B = 890$ cm^{-1}, $C/B = 4.2$.
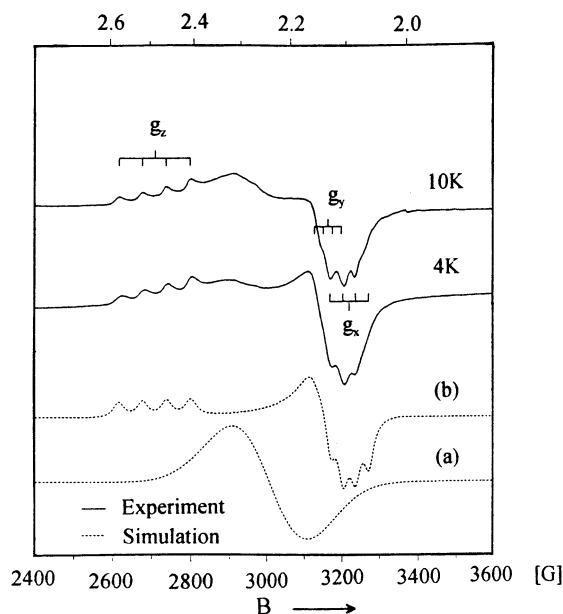
Fig. 16. X-band EPR spectra of Cu^{2+}-doped $MgCO_3$ (0.3 mol%); simulation with g- and A-tensor components: $g_z = 2.49_0$, $g_y = 2.13_2$, $g_x = 2.09_4$; $A_z = -72$, $A_y = 24$, $A_x = 34 \times 10^{-4}$ cm^{-1} (line widths 10, 15 and 10 G, respectively). The isotropic signal (g = 2.24, line-width 100 G) is superimposed with the intensity ratio (a)/(b) = 0.6.

angular distortion due to an elongation along a $\bar{3}$ axis (OMeO angles around $\bar{3}$: $6x \cong 88.5°$) [31]. The cationic oxygen environment is strictly planar $CONi_2$, the CONi and NiONi bond angles being 119.3° (2x) and 121.6°, respectively.The effective charges polarising the oxygen ions from opposite sides are $+4/3$ (C^{IV}) and $+2/3$ (2 Ni^{2+}), suggesting a sp_z hybridisation along the C–O bond. The remaining p_x and p_y orbitals of oxygen are oriented perpendicular to the $CONi_2$ plane, as indicated in Fig. 14, and located in this plane, respectively.The charge distribution is rather similar to that in the olivine $LiNiPO_4$, and indeed a rough fit to the spectrum of Ni^{2+}-doped $MgCO_3$ (Fig. 15) is achieved with the parameter set (Eq. (9)). It is considerably improved choosing a by more than 20% reduced $e_\pi(p_x,p_y)$ energy, which is expected because the π-double bond of CO_3^{2-} corresponds to the overlap with the same p_x, p_y orbitals used for the Ni–O π-bonding (Fig. 14). A conventional type AOM calculation with reasonable e_σ and e_π parameters does not reproduce the band positions and the intensity distibutions sufficiently well.

Evidence for the presence of an inherent symmetry effect connected with the assumption of a sp_z hybridisation at the oxygen atoms as in the case of Ni_2GeO_4 comes from a calculation, which neglects the small trigonal distortion of the NiO_6 octahehedra. It yields band splittings of nearly the same magnitude. The symmetry effect is also apparent in the EPR spectra of Cu^{2+}-doped $MgCO_3$ (Fig. 16), which are isotropic at high and well resolved anisotropic at low temperature. The

substitution of Mg^{2+} by Cu^{2+} should lead to an elongated octahedron without lower-symmetry distortion components because a significant host site strain is not present. The g-tensor is distinctly orthorhombic though (see caption to Fig. 16). The large g-values and the small ground state splitting of $\cong 4000$ cm^{-1} (from the d–d spectrum) suggest an only very modest Jahn–Teller distortion of the CuO_6 octahedra due to a rather rigid lattice. The isotropic signal, which still contributes to the intensity of the EPR spectrum at 4 K, is most probably caused by thermally averaged CuO_6 polyhedra (dynamic Jahn–Teller effect).

2.4. Rutile-type solids

While in the preceding sections symmetry effects connected with a sp hybridisation on the oxygen atoms have been considered, with Ni_2GeO_4 and Co_2GeO_4 (Figs. 2 and 3) as spectacular examples, we will consider in the following bond anisotropies of a very different kind. While the d–d spectra of rutile-type solids $Zn_{1-x}Ni_xSb_2O_6$ (Fig. 18) show very distinct band splittings, those of $NiTa(Nb)_2O_6$ with the same structure (Fig. 19 I–III) possess a nearly cubic appearance. This is unexpected because the angular distortion of the NiO_6 octahedra and the small bond length differences are the same in all mentioned cases. Furthermore, the excited $^2T_{2g}$ state of Cu^{2+} in the d–d spectra of mixed crystals $Zn_{1-x}Cu_xSb_2O_6$ (Fig. 20) is split considerably (nearly 3000 cm^{-1}), though the ^2E_g ground state splitting is < 4000 cm^{-1}, indicating only a small Jahn–Teller distortion of the CuO_6 octahedra. We will show below that a sp$^2_{x,y}$ hybridisation on oxygen, which implies strongly anisotropic π-bonds via the p_z orbital, accounts accurately for the mentioned and further spectral phenomena. $ZnSb_2O_6$ crystallises in the tetragonal rutile structure with an ordered distribution of the metal ions over the octahedral sites (Fig. 17a: trirutile type, space group $P4_2/mnm$) [32]. The oxygen ions possess a planar $ZnOSb_2$ coordination (Fig. 17b), with bond angles Sb–O1(O2)–Sb of $\sim 103(133)°$ and Zn–O1(O2)–Sb of $\sim 129°$ (128°) and 129° (100°). Following our previous concept, which implies that the high-valent cations determine predominantly the bonding situation at the ligands, a sp^2 hybridisation at the oxygen atoms (σ-bonds) is suggested, with one p-orbital perpendicular to the $ZnOSb_2$ plane available for π-overlap. The directions of the sp^2 hybrid orbitals have been chosen such, that they are symmetrically oriented with respect to the two Sb–O1(O2) bonds. Thus, the third hybrid orbital has the direction of the Ni–O bond for O1, but forms an angle of $\cong 14°$ with this bond in the case of O2. Fig. 17c depicts the geometry of the ZnO_6 polyhedron, which is compressed slightly along the Zn–O1 spacings. In particular the orientations of the p(π) orbitals are depicted. The molecular x, y and z axes are the C_2 axes of the D_{2h} distorted octahedron, the O2–Zn–O2′ bond angles around x and y being $\cong 78°$ and $\cong 102°$, respectively. The distinct misdirection of the sp^2 hybrids in the case of O2 implies a by about 6% smaller overlap along the Zn–O2 bond. The Zn–O2 spacing on the other hand is by $\cong 0.03$ Å larger than the Zn–O1 distance, which corresponds to a $\sim 7\%$ weaker bond, if a dependence of the crystal field on the fifth power of the distance is assumed. Apparently the two effects are correlated, and indeed we cannot fit the

spectral data sufficiently well when including both effects into the calculations. Because the angular effect is obviously model dependent, we have—successfully, see below—only the different Ni–O spacings taken into account. We will come back to the considered correlation phenomenon (see also Section 2.2) when discussing solids with the columbite structure.

2.4.1. Nickel(II)

The optical spectra of Ni^{2+} in the tetragonal trirutile-type solids $Zn_{1-x}Ni_xSb_2O_6$ and $NiTa_2O_6$ are depicted in Figs. 18 and 19. The NiO_6 and ZnO_6 octahedra are slightly tetragonally compressed ($NiTa_2O_6$: 2.048 Å (Ni–O1, 2x), 2.082 Å (Ni–O2, 4x), $\alpha = 81°$ [33]; see Fig. 17c). Adopting the parameters in Eq. (11) and allowing for the slightly different Zn(Ni)–O bond lengths, a very good fit to the spectrum in
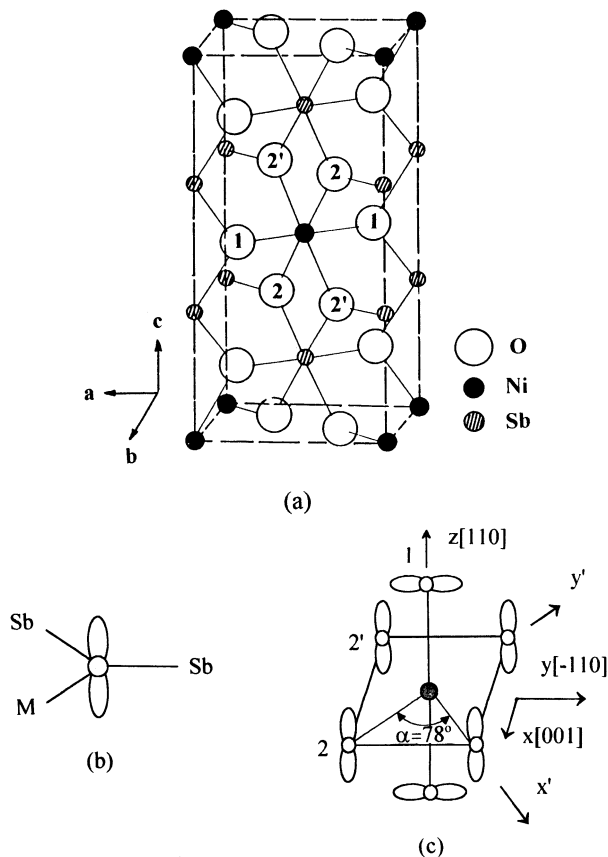
Fig. 17. (a) The trirutile unit cell of $Zn(Ni)Sb_2O_6$ (space group $P4_2/mnm$); (b) the planar cationic coordination of the oxygen ligator atoms O1 and O2, bond angles are given in the text; (c) the NiO_6 polyhedra—molecular geometry D_{2h} (compression $\|z$)—with the orientations of the p-orbitals available for π-bonding indicated. In the case of $CuSb_2O_6$ the CuO_6 polyhedra possess C_{2h} symmetry (elongation $\|x'$), see text.
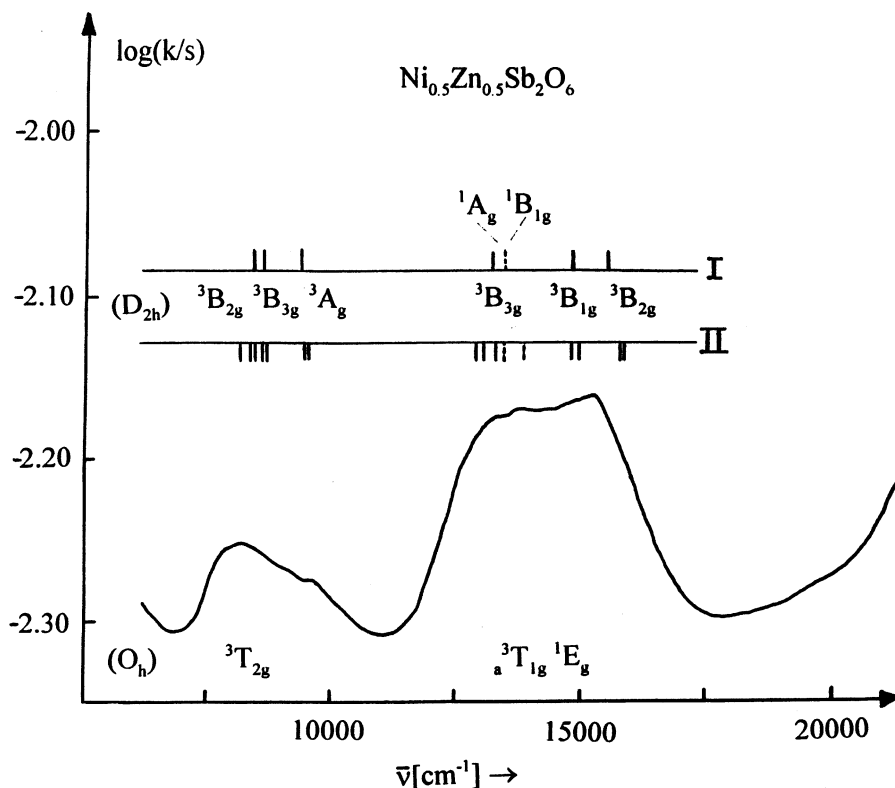
Fig. 18. Diffuse reflection spectra of the mixed crystal series $Zn_{1-x}Ni_xSb_2O_6$ with $x = 0.5$. Assignment (D_{2h} symmetry, $^3B_{1g}$ ground state; octahedral parent terms are also given) and fitting of band positions (dotted markings refer to the spin-forbidden transitions to ^1A_g, $^1B_{1g}$) with the parameter set of Eq. (11): I and II without and with LS coupling, respectively.

Fig. 18 is obtained—see also the comparison of the experimental band positions with the calculated transition energies in Appendix B—if the bonding anisotropy according to the orientation of the p(π) orbitals in Fig. 17c is taken into account.

$$e_\sigma = 3485 \text{ cm}^{-1}, \ e_\pi = 660 \text{ cm}^{-1} \quad \text{(for a (Ni–O)} = 2.07 \text{ Å)};$$

$$\Delta \cong 9150 \text{ cm}^{-1}, \ B = 850 \text{ cm}^{-1}, \ C/B = 4.2; \ \xi = 520 \text{ cm}^{-1} \tag{11}$$

In particular, the spectral intensity distribution is nicely reflected, which cannot be achieved in a calculation with isotropic π-bonding. The considerable splittings of the $^3A_{2g} \rightarrow {}^3T_{2g}$, $_a^3T_{1g}$ transitions are well reproduced. Because the $^3A_{2g} \rightarrow {}_b^3T_{1g}$ transition is covered by the charge-transfer originating from Sb^V, the Racah parameter B is only estimated roughly. We can state already here—and the discussion of the spectral properties of the corresponding Cu^{2+} mixed crystal series will confirm this—that it is the π-anisotropy which is predominantly responsible for the apparent symmetry splitting. The octahedral ligand field parameter is calculated

to be $\cong 9150$ cm^{-1}, if one utilises Eq. (12), which takes the reduced π-(anti)bonding capacity of oxygen in the trirutile structure into account (due to the presence of only one π-orbital per oxygen atom, Fig. 17c).

$$\Delta = 3e_\sigma - 2e_\pi \qquad (12)$$

The appeearence of the d–d spectrum of NiTa$_2$O$_6$ and of NiNaNbO$_6$ as well (Fig. 19I, II), is very different from that of Ni^{2+} in ZnSb$_2$O$_6$. Firstly, the band splittings due to the π-anisotropy are much less pronounced and hence indicate a reduced e_π parameter (see Appendix B). Secondly, the bands have shifted to distinctly lower energies, implying a by more than 10% smaller ligand field parameter Δ. A lower-energy shift of about the same magnitude is observed, when comparing the Δ value of Zn$_{1-x}$Cu$_x$Sb$_2$O$_6$ mixed crystals with that of the trirutile
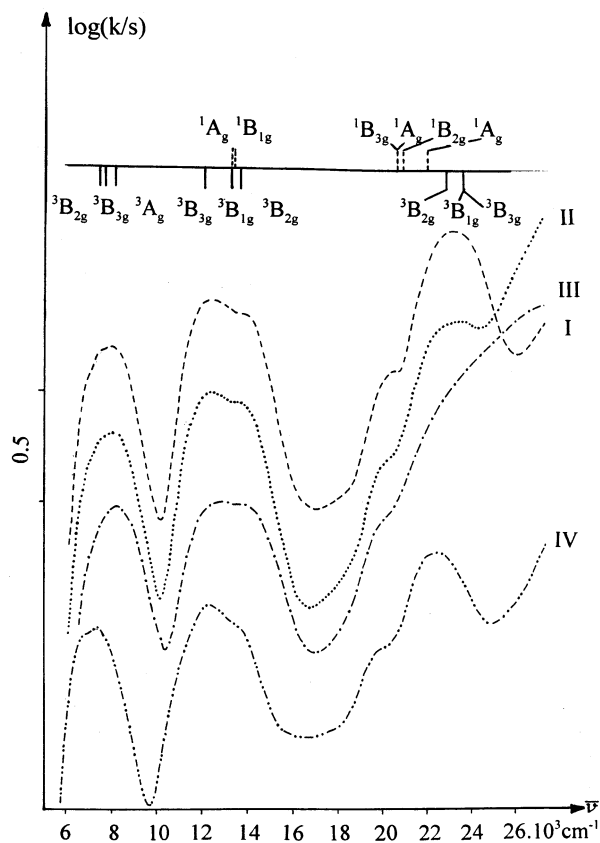
Fig. 19. Diffuse reflection spectra of various oxide ceramics with the trirutile (I: NiTa$_2$O$_6$; II: NiNbTaO$_6$) and the disordered rutile structure (III: NiNb$_2$O$_6$, high-temperature phase). The spectrum of NiNb$_2$O$_6$ in the low-temperature modification (columbite lattice) is also shown (IV). The assignment (D_{2h} symmetry, $^3B_{1g}$ ground state) and fitting (octahedral parent terms: $^3T_{2g}$, $_aT_{1g}$, $_aE_g$, $_aT_{2g}$, $_aA_{1g}$, $_bT_{1g}$) are given for I, with the parameters in Eq. (13) and on the basis of the structural data [33].

$Zn_{0.625}Cu_{0.375}Ta_2O_6$ [34]. With the parameter set in Eq. (13), where tentatively an e_π parameter is chosen, which is about half in magnitude of that valid for the $Zn_{1-x}Ni_xSb_2O_6$ mixed crystals, a good fit to the spectrum of $NiTa_2O_6$ is achieved.

$$e_\sigma = 2900 \text{ cm}^{-1}, \ e_\pi = 350 \text{ cm}^{-1};$$

$$\Delta = 8000 \text{ cm}^{-1}, \ B = 850 \text{ cm}^{-1}, \ C/B = 4.2 \qquad (13)$$

In particular only band splittings of the $^3A_{2g} \rightarrow {}^3T_{2g}$, $^3_bT_{1g}$ transitions below 1500 cm^{-1} are predicted. Because we cannot not exclude, that e_π is even smaller, an e_σ value < 2900 cm^{-1} is equally feasible.

The band positions of $NiNb_2O_6$ in the high-temperature modification (quenched from 1400°C), which possesses a disordered rutile structure, are very similar to those of the trirutile phases $NiTa_2O_6$ and $NiTaNbO_6$. Only the third spin-allowed transition is obscured by a low-lying band, which is presumably caused by Ni^{2+}–Ni^{2+} charge-transfer due to the occupation of interconnected octahedra by Ni^{2+}. A distinct red-shift of the $NiNb_2O_6$ spectrum occurs by the structural change from the rutile to the columbite lattice (Fig. 19 III, IV) which will be commented on below.

The rather different AOM parameters for mixed crystals $Zn_{1-x}Ni_xM_2O_6$ (M = Sb^V and Ta^V, Nb^V, respectively) in spite of equal metal-to-oxygen spacings can be understood as follows. The $4d^{10}$ configuration of Sb^V implies an only weak tendency for a $4d\pi$–$2p\pi(O)$ overlap due to fully occupied bonding and antibonding t_{2g} orbitals, in contrast to the d^0 configured Ta^V and Nb^V ions, where a considerable π-overlap with oxygen is expected. This has, in our opinion, severe consequences also in respect of the $d\sigma$ contributions to the M^V–O bonds, these being more pronounced for Sb^V than for Ta^V or Nb^V in order to compensate for the π-energy deficiency. The Ni–O bonds seem to follow this pattern in the case of the $d\sigma$-bond contributions, with about a 20% larger e_σ parameter in the d^{10} case (Eqs. (11) and (13))—apparently because the 3d orbitals overlap with oxygen sp^2 hybrid orbitals, which also accomplish the bonds with the two Sb^V or Ta^V (Nb^V) atoms. On the other hand, $Ta^V(Nb^V)$ and Sb^V exhibit π-overlap with *one and the same p orbital* at the oxygen ligator atom (Fig. 17b) as Ni^{2+} does. Smaller e_π energies for the tantalates (niobates) than in the case of the antimonates have hence to be anticipated, because in the former solids more π-bonding capacity is used for the M^V–O bond. This concept readily explains the parameter magnitudes, though the π-effect—due to e_π energies of only small magnitude—is not as spectacular as the σ-effect. Furthermore, cations with a d^{10} configuration are more polarisable in comparison to the rather rigid d^0 cations, implying that the metal–oxygen bonds are more covalent in $NiSb_2O_6$, which is also in accord with the higher e_σ and e_π energies. This aspect and the just considered dependence of the interplay between the $d\sigma$ and $d\pi$ contributions to the Ni–O bond on the geometry and the electronic configurations of the high-valent cations in the coordination sphere of oxygen is beyond the scope of this section and will be discussed in greater detail in Section 3.

Table 3
Cu–O spacings (Å), AOM parameters (cm^{-1}) and observed molecular g-values for the compressed (D_{2h}) and elongated (C_{2h}) CuO$_6$ polyhedra in mixed crystals Zn$_{1-x}$Cu$_x$Sb$_2$O$_6$[a] [36]

		e_σ	e_π	g_i
Cu–O1	D_{2h} 1.98 (2x)	4560	975	2.02 ($\|z$)
Cu–O2	2.08 (4x)	3035	545	2.35 ($\|y$)
				2.33$_5$ ($\|x$)
Cu–O2	C_{2h} 2.12 (2x)	2545	430	2.11[b] ($\|z$)
Cu–O1(2′)	$\cong$ 2.01 (4x)	4015	815	2.13$_5$[b] ($\|y'$)
				2.43[b] ($\approx \|x'$)
$\overline{\text{Cu–O}}$	2.04$_5$ (6x)	3485	660	
$\overline{\text{Cu–O}}$[c]	2.04$_5$ (6x)	5070	1900	
$\overline{\text{Cu–O}}$[d]	2.04$_5$ (6x)	5900	2280	

[a] The AOM energies for the averaged (octahedral) spacings are also listed.
[b] Calculated from the observed exchange coupled g_i^e values: $g_1^e = 2.11$, $g_2^e = 2.19_5$, $g_3^e = 2.37$ [36].
[c] AOM parameters from the spectral fit to Fig. 20 without assuming π-anisotropy, for the compressed octahedron (see text).
[d] AOM parameters from the spectral fit to Fig. 20 without assuming π-anisotropy, for the elongated octahedron (see text).

A series of d–d spectra of oxidic solids with the trirutile and rutile structure, collected by Kasper [35], impressively demonstrates the discussed symmetry effect when switching from a d^{10} to a d^0 cation. The spectral appearence for compounds with a mixed d^0/d^{10} occupation on the M^V positions—NiNbSbO$_6$ or NiTaSbO$_6$ for example—is intermediate between those considered in Figs. 18 and 19.

We proceed to consider the Zn$_{1-x}$Cu$_x$Sb$_2$O$_6$ mixed crystals series, the spectral properties of which give further evidence for the proposed bonding concept.

2.4.2. Copper(II)

The substitution of Cu(II) into the Zn(II) site of ZnSb$_2$O$_6$ induces an enhanced compression of the CuO$_6$ polyhedra $\|z$ due to vibronic coupling (Jahn–Teller effect) at a low Cu(II) doping level, while at higher concentrations the distortion switches to the slightly more preferred elongation ($\|x'$, see Fig. 17c) [36]. CuSb$_2$O$_6$ crystallises in a monoclinic variant of the trirutile structure ($P2_1/n$) [37] induced by the cooperative order of the two magnetically inequivalent CuO$_6$ polyhedra with such a geometry in the unit cell. The observed Cu–O spacings and molecular g-values [36] are listed in Table 3. Surprisingly, the reflection spectra of mixed crystals Zn$_{1-x}$Cu$_x$Sb$_2$O$_6$ do not change significantly, neither in respect to the intensity distribution of the broad and structured band corresponding to the transition to the split terms of the octahedral ^{2}T$_{2g}$ parent state nor regarding the extent of the symmetry splitting (Fig. 20), though the CuO$_6$ polyhedra switch from compressed to elongated. With the choice of the same AOM parameters e_σ and e_π for the averaged Cu–O spacing as those for the Ni–O bond (Eq. (11)), energy parameters for all involved bond lengths can be calculated utilising Eq. (2) and are listed in Table 3.

The AOM calculations for the compressed and elongated[1] CuO_6 polyhedra, based on the molecular geometries (D_{2h} and C_{2h}, respectively), as revealed by crystallographic and spectroscopic data [36], yield the term diagrams in Fig. 21. Calculational details are given elsewhere [13]; here we cite only the matrix connecting the two ^2B_g terms (Eq. (14); C_{2h} case). $\alpha(\cong 78°)$ is the angle around the x-axis, while x', y', z denote the Cu–O bond directions with respect to which the AOM parameters are defined (Fig. 17c).

$$
\begin{array}{lll}
d_{xz} & 2\cos^2(\alpha/2)(e_\pi^{x'} + e_\pi^{y'}) & -\sin\alpha(e_\pi^{x'} - e_\pi^{y'}) \\
d_{yz} & -\sin\alpha(e_\pi^{x'} - e_\pi^{y'}) & 2\sin^2(\alpha/2)(e_\pi^{x'} + e_\pi^{y'}) + 2e_\pi^z
\end{array} \qquad (14)
$$

The calculated transition energies, for both D_{2h} and C_{2h} geometries, are in thoroughly good agreement with the observed band positions and a spectral appearance, which is largely independent on x. The Cu–O spacings in the D_{2h} case, which are not directly accessible from the experiment, have been chosen such, that the
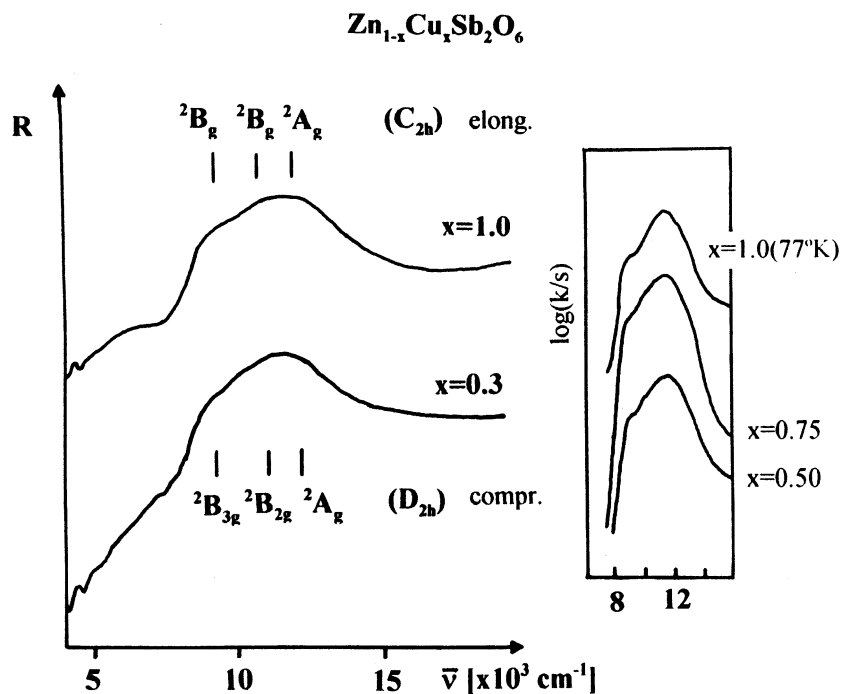
$$Zn_{1-x}Cu_xSb_2O_6$$

Fig. 20. Diffuse reflection specra of $Zn_{1-x}Cu_xSb_2O_6$ mixed crystals (298 K; reflectivity scale is arbitrary). The resolution is not essentially improved at 5 K. Assignment and energy positions according to Fig. 21; with inclusion of the deviation of α from 90° (Fig. 17c) and LS coupling ($\zeta = 665$ cm^{-1}, 80% of the free ion value). The insert shows spectra with the log k/s intensity scale.

---

[1] The small deviations of the O1–Cu–O2(O2') bond angles from 90° ($\pm 2°$) and the tiny equatorial Cu–O bond length difference [$\|z$: 2.004(4) Å, $\|y'$: 2.012(4) Å] (Fig. 17c) have been neglected.

III   **II**   **I**   **I**   **II**   **III**

E

D$_{2h}$(D$_{4h}$) compr.   **C$_{2h}$(D$_{4h}$) elong.**

Left diagram (D$_{2h}$ compr.), from top:

$^2A_g(^2B_{2g})$ — $\approx dx^2-y^2$

$^2B_{2g}(^2E_g)$ — dxz

$^2B_{3g}(^2E_g)$ — dyz

$^2B_{1g}(^2B_{1g})$ — dxy

$^2A_g(^2A_{1g})$ — $\approx dz^2$

Right diagram (C$_{2h}$ elong.), from top:

$^2A_g(^2E_g)$ — $\approx dx^2-y^2$

$^2B_g(^2E_g)$ — $\approx dxz$

$^2B_g(^2B_{2g})$ — $\approx dyz$

$^2A_g(^2A_{1g})$ — $\approx[(1/2)dz^2+(\sqrt{3}/2)dxy]$

$^2A_g(^2B_{1g})$ — $\approx[-(\sqrt{3}/2)dz^2+(1/2)dxy]$

Energy scale: 2, 4, 8, 10, 12
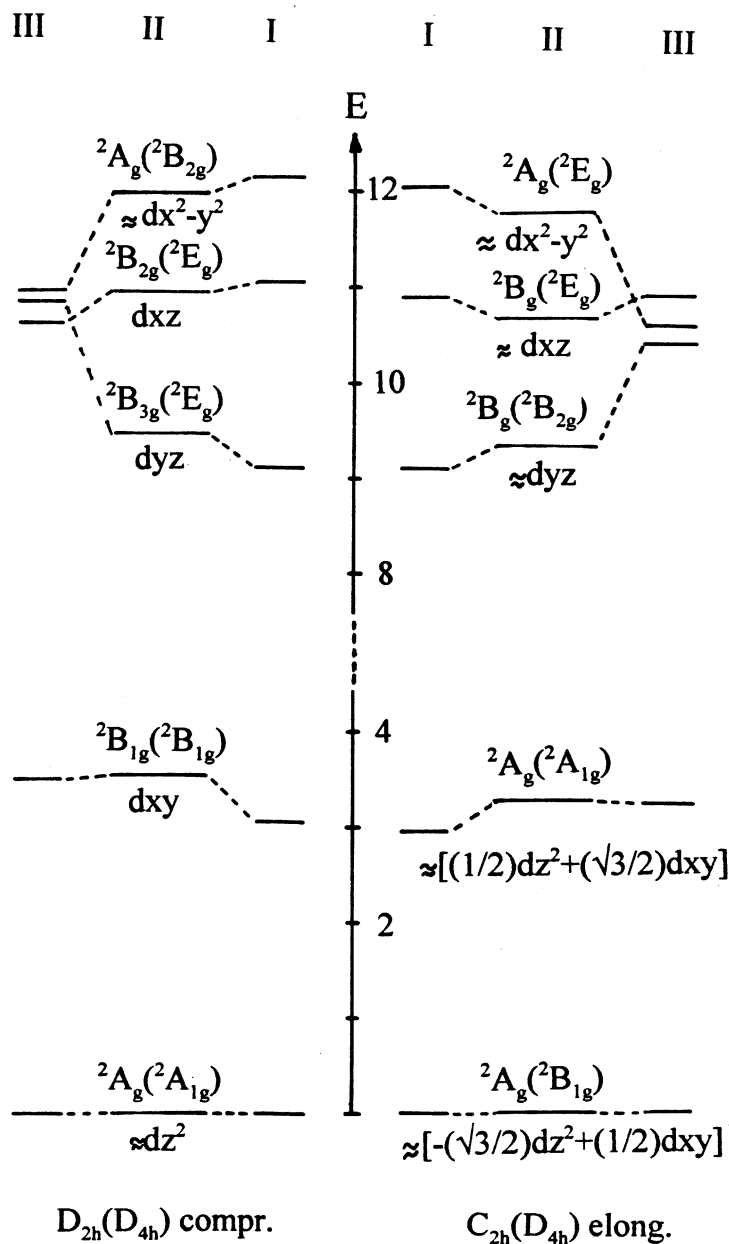
Fig. 21. Calculated energy positions of the terms originating from the 3d^9 configuration of Cu(II) in the trirutile lattice, based on available crystallographic and spectroscopic data [36] and the AOM parameter set in Eq. (11) and Table 3. The geometries are compressed $D_{2h}(\|z)$ (left) and elongated $C_{2h}(\|x')$ (right), without (I) and with (II) taking the deviations of the angles around x and y (see Fig. 17c) from 90° into account. The AOM energies of the excited states (for $\alpha = 90°$ and from lower to higher energies) are for D_{2h}: $2(e_\sigma^z - e_\sigma^{x'y'})$, $2e_\sigma^z + e_\sigma^{x'y'} - 2(e_\pi^z + e_\pi^{x'y'})$, $2e_\sigma^z + e_\sigma^{x'y'} - 2e_\pi^{x'y'}$, $2e_\sigma^z + e_\sigma^{x'y'}$ (left) and for C_{2h}: $2(e_\sigma^{yz} - e_\sigma^{x'})$, $3e_\sigma^{y'z} - 2e_\pi^{y'z} - e_\pi^{x'} \mp N$, $3e_\sigma^{y'z}$, the non-diagonal energy N being $\{(e_\pi^{y'z})^2 + (e_\pi^{y'z} - e_\pi^{x'})^2\}^{1/2}$ (right). The tetragonal parent terms are given in parentheses and the energy scale is in units of 10^3 cm^{-1}. III gives the orbital energies, if the π anisotropy according to Fig. 17c is not taken into account: e_π (isotrop.) = 330 cm^{-1}.

calculated d–d transition energies match with those of the elongated octahedron within 200 cm^{-1}. Apparently the spectrum is governed by the π-anisotropy imposed on the oxygen atoms by their cationic coordination (Fig. 17c) rather than by the bond length changes accompanying the geometrical switch, as can be infered from a conventional MO calculation with the same AOM parameters, but without taking the π-anisotropy into account (Fig. 21 III: e_π (isotrop.) $= \frac{1}{2} e_\pi$). The considerable deviation of the angle α from 90° has only a small energy effect (Fig. 21 I → II). In agreement with the experiment the calculated splittings of the octahedral ^2E_g ground state are below the low-energy limit of spectral observation (Fig. 20).

When trying to fit the experimental spectra without allowing for the π-anisotropy, very large in particular e_π parameters result, in order to reproduce the considerable splitting of the $^2T_{2g}$ state. The e_σ and e_π values for the averaged octahedral spacing (2.04$_5$ Å), derived from these calculations, are considerably larger than those when taking π-anisotropy into account and furthermore differ significantly for the elongated and compressed geometry (Table 3^{c,d}). Also, the calculated ground state splittings are far above 5000 cm^{-1}—these findings being in contrast to a sound bonding concept and the experimental results.

In spite of the given arguments in favour of the anisotropic π-bonding model one might reason, that the so-far experimental evidence—splittings of rather broad ligand field bands (Figs. 18 and 20)—is only partly convincing. We will show in the following, however, that the observed g-values of the considered mixed crystal series with Cu^{2+} strongly support the proposed anisotropic bonding concept.

If the g-values for the compressed CuO$_6$ octahedron are calculated, adopting the energy positions of Fig. 21 and taking the intermixing of the two ^2A_g terms in the D_{2h} point group into account, one obtains perfect agreement with the observed g-tensor components (Table 3) when choosing covalency parameters $k_x = k_y = k_z = 0.83$ for the involved orbitals d$_{yz}$, d$_{xz}$ and d$_{x^2-y^2}$ ($g_x = 2.32_9$, $g_y = 2.35_5$, $g_z = 2.01_5$). The covalency parameters can be derived from the orbital contributions u_i to the g-tensor components for a d^9 cation. The latter are defined in a D_{2h} ligand field and in second order perturbation theory as in Eq. (15). Here ξ_0 is the free-ion LS coupling constant (830 cm^{-1} for Cu(II)), and the ΔE_i are the transition energies from the ground state to the excited split states originating from the octahedral $^2T_{2g}$ parent term (d$_{yz}$, d$_{xz}$ and d$_{x^2-y^2}$ for $i = x$, y and z, respectively, Fig. 21 left).

$$u_i = k_i^2 \xi_0^2 / \Delta E_i \quad (i = x, y, z) \tag{15}$$

The orbital reduction factors k_i are in first approximation products of the mixing coefficients, which specify the metal contributions in the MO wave-functions of the ground state [^2A_g ($\cong$ d$_z^2$): α; see Eq. (20) in Section 4.1] and of the excited states [^2A_g(d$_{x^2-y^2}$): β; $^2B_{2g,3g}$ (d$_{xz}$, d$_{yz}$): γ, γ']] (Eq. (15a)).

$$k_z \approx \alpha\beta; \qquad k_y \approx \alpha\gamma; \qquad k_x \approx \alpha\gamma' \tag{15a}$$

With the α-coefficient derived from the copper fine-structure (0.91) [36] we estimate $\gamma \cong \gamma'$ to be ~ 0.91. Both values indicate, that the Cu–O bonds in the trirutile structure are rather ionic. It should be noted, that the difference of the calculated g-values in the molecular xy plane of the compressed (D_{2h}) octahedron
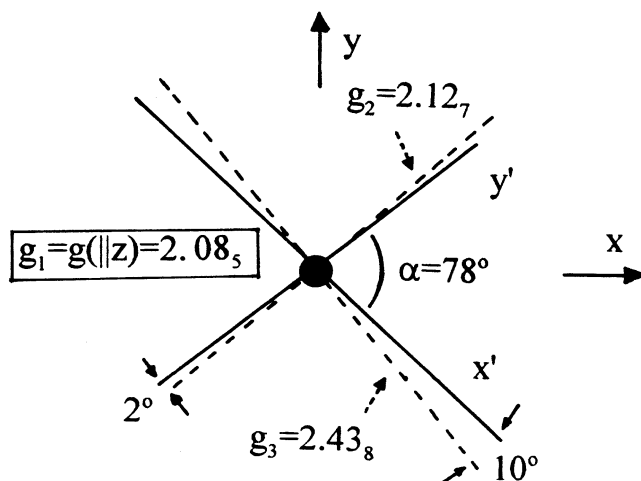
Fig. 22. Calculated g-tensor components for the elongated CuO_6-polyhedron in $Zn_{1-x}Cu_xSb_2O_6$ mixed crystals and their orientations with respect to the Cu–O spacings along x', y', z (see Fig. 17c).

is considerably enhanced from $\delta g = g_x - g_y \cong 0.02_5$ to about 0.08, if the π-anisotropy is removed—a surprisingly distinct effect, which is induced by the deviation of the O2–Cu–O2' angles from 90° (Fig. 17c) but largely compensated by the π-anisotropy.

Performing an analogous calculation for the elongated octahedron, but choosing isotropic covalency coefficients $k_i = 0.80$ ($i = $ x, y, z), which are somewhat smaller than those for the compressed geometry, the g-values of Fig. 22 are obtained. As observed usually in such cases the two small g-tensor components closely follow the directions of the short Cu–O bond lengths ($g_1 = g(\|z)$; $g_2 = g(\|y')$ within 2°). The third one (g_3) is oriented perpendicular to the $y'z$ plane with an angle of 10° with respect to the long Cu–O spacing $\|x'$. The molecular g-values cited in Table 3 were derived from the experimental exchange-coupled g^e-tensor components [36]. From these the $g(\|y')$ and $g(\approx \|x')$ parameters are in good agreement with the corresponding calculated values. The considerable mismatch between the calculated (Fig. 22) and the observed $g(\|z)$ value (Table 3), however, can only be removed, if k_z is substantially enhanced. Having in mind that the orbital contribution to $g(\|z)$ is connected with the xy-plane (Fig. 21), in which π-overlap is not possible (Fig. 17c), we expect a mixing coefficient $\beta = 1.0$ and hence a covalency parameter k_z equal to $\alpha \approx 0.91$ (Eq. (15a)). With the latter value we calculate $g(\|z) \cong 2.11$, in perfect accord with the experiment.

The conclusion, that π-anisotropies are important in controlling the d-contributions to the Cu–O bonds in oxide ceramics with the trirutile structure, seems hence justified by the EPR results as well. We further note as an interesting observation, that the local symmetry axes x and y of the CuO_6 polyhedra, which strongly deviate from the orientations of the Cu–O bonds along x', y' (Fig. 17c), are *the directions of quantisation for the two d_π-orbitals (d_{xz}, d_{yz})*. This is not only true for the

compressed (D_{2h}), but approximately also for the elongated octahedron (C_{2h}) with strongly differing spacings along x' and y'. While for the orientations of the mentioned two orbitals the π-anisotropy is decisive, the g-tensor components show a completely different orientational preference by closely following the directions of the short (and long) Cu–O bonds along y' (and $\sim x'$) in the C_{2h} case (Fig. 22). This is so because the factors, with which the u_i in Eq. (15) contribute to the g-values in tetragonally elongated octahedra (8 and 2 for $g(\| \approx x')$ and $g(\|y') \approx g(\|z)$, respectively), are determined by the σ-bonding in the ground state, which follows the Cu–O bond vectors. The π-anisotropy is only reflected by the *magnitudes* of the u_i's via the ΔE_i energies but has no distinct orientational influence.

The different properties of the metal–oxygen bonds in solids crystallising with the rutile or trirutile lattice are reflected structurally also. Thus, compounds such as $A^{II}Me_2^VO_6$ [A^{II}: Mg, Ni, Co], $A^{III}Me^VO_4$ [A^{III}: Al, Rh, Cr, Ga] and $Cr_2M^{VI}O_6$ exhibit c/a ratios (c being 1/3 of the lattice constant c' in the trirutile case) of ≥ 0.66, if the Me^V or M^{VI} cation is d^{10} configurated [Sb,Te], and ≤ 0.65 for d^0 cations such as Nb, Ta and W [7]. The reason is, that the angles within the
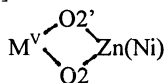
$$M^V \overset{O2'}{\underset{O2}{\diagup\diagdown}} Zn(Ni)$$

bridging units aligned along the crystallographic c-direction (Fig. 17a) are significantly different for $M^V =$ Sb and Ta, namely 78° (O2–M^V–O2′) and 82° (O2–Zn(Ni)–O2′) in the former case, compared to 81 and 86° in $NiTa_2O_6$. The consequence is a transition metal-to-M^V spacing via the common O2,O2′-edge, which is smaller for Ta^V. This indicates a σ-overlap between the *occupied* non-bonding $d_{x^2-y^2}$ orbital of Ni^{2+} (Fig. 17c and Fig. 21) and a correspondingly oriented *empty* 5d orbital of Ta^V. An interaction of this type is not possible for the d^{10}-cation Sb^V and yields in our opinion a further argument for the importance of bonding effects in the rutile structure, which markedly vary with the electronic structure of the M^V cations.

Interestingly enough, Cr^{3+} behaves similar to Ni^{2+}—the Δ values of $CrNbO_4$ (~ 14000 cm^{-1}) and Cr_2WO_6 (13400 cm^{-1}) being distinctly smaller than those of $CrSbO_4$ (~ 15000 cm^{-1}) and Cr_2TeO_6 (~ 16000 cm^{-1}) [24].

3. The variability of the ligand field parameter Δ—the interplay between dσ and dπ contributions to the transition metal–oxygen bond

In Table 7 the AOM parameters of Ni^{2+} (Co^{2+} and Cu^{2+} show analogous trends) in the octahedral sites of so far discussed structures are summarised. Before analysing the trends in the magnitude of e_σ and e_π in more general terms further example material will be presented.

3.1. Perovskite-type compounds

Perovskites ABO_3 consist of cubically close packed layers of A cations and

oxygen, the B cations occupying those octahedral interstices between the layers, which are exclusively formed by oxygen (Fig. 23). In elpasolites $A_2BB'O_6$ the octahedrally coordinated cations B and B' order perpendicular to the close-packed layers. The cationic oxygen coordination is linear, with one B and one B' centre, and is supplemented by four A cations to pseudooctahedral (Fig. 23c). As the selection of oxidic solids with ordered perovskite-type structures in Table 4 illustrates, strongly diverging Δ parameters result if Ni^{2+} is isomorphously incorporated into one of the octahedral sites [7], depending on whether d^0 or d^{10} cations occupy the other six-coordinated position. The substitution of W^{VI} or Nb^V in the Sr^{2+} elpasolites 3,4 by Te^{VI} or Sb^V for example leads to a decrease of the ligand field parameter of greater than 1500 cm^{-1}, though the Ni–O spacings do not change significantly. This effect is reverse to that observed in the case of the solids with the rutile structure and much more pronounced (Table 7).

The linear B–O–Ni bonds in the pseudooctahedral cationic oxygen coordination with C_{4v}-symmetry (Fig. 23c)—with one high-valent B cation, which dominates the bonding around the oxygen atoms—suggest a sp_z hybridisation along this direction. The perpendicular p_x, p_y orbitals are directed toward the large A cations. Because all listed compounds are either cubic or deviate only slightly from cubic
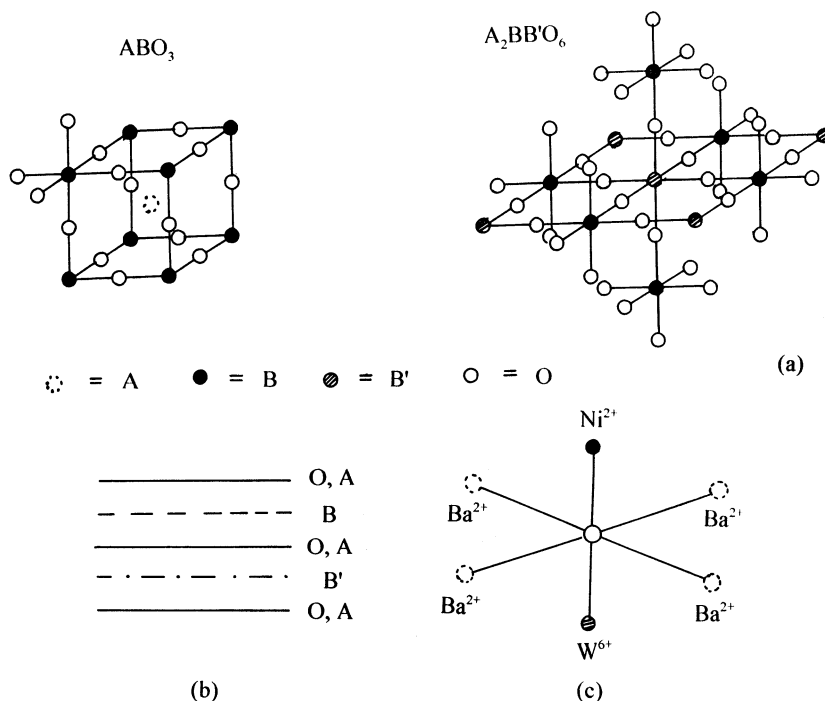

Fig. 23. (a) The perowskite unit cell and the frame of corner-connected octahedra in the elpasolite structure; (b) the cation order (B, B') perpendicular to close-packed layers (A, O) in elpasolite-type solids; (c) the cationic oxygen coordination in Ba_2NiWO_6.

Table 4
Ligand field parameters Δ and B (10^3 cm^{-1}) of perowskite-type solids [1,3,8,9,10 and 2,4,5,6,7 with 1:1 and 1:2 order, respectively; 11,12 disordered; 13,14 hexagonal BaTiO$_3$ structure with 1:2 order][a]

		Δ	B	a
1	Sr_2NiTeO_6	6.6	0.86_5	2.04
2	$Sr_3NiSb_2O_9$	6.9	$\cong 0.86$	(2.03)
3	Sr_2NiWO_6	8.5	$\cong 0.86$	2.04
4	$Sr_3NiNb_2O_6$	8.6	0.85	(2.03)
5	$Ba_3NiNb_{3/2}Sb_{1/2}O_9$	7.1	(0.85)	(2.08)
6	$Ba_3NiTa_2O_9$	7.6_5	0.85	(2.08)
7	$Ba_3NiNb_2O_9$	7.6_5	0.85	(2.08)
8	Ba_2NiWO_6	7.3_5	0.85	2.09
9	$Ba_2Ni_{0.4}Ca_{0.6}WO_6$	6.5_5	0.86_5	
10	$Ba_2Ni_{0.1}Ca_{0.9}TeO_6$	4.9	0.87	
11	$LaNi_{0.2}Mg_{0.3}Zr_{1/2}O_3$	8.5	0.82	
12	$LaNi_{0.2}Mg_{0.3}Sn_{1/2}O_3$	8.3	0.83	
13	$Ba_3NiSb_2O_9$	6.2	0.87	
14	$Ba_3Ni_{1/2}Ca_{1/2}Sb_2O_9$	5.8_5	0.87_5	

[a] Average Ni–O spacings (Å) are also given (estimated values in parentheses).

symmetry and furthermore the bonding symmetry on the oxygen atoms is high (see Fig. 23c), band splittings in the d–d spectra beyond those due to LS coupling are not expected and indeed not observed (Fig. 24). The solids of the constitution $A_2^{II}NiM_2^VO_9$ (A^{II}: Sr, Ba) in Table 4 differ from the elpasolites by displaying a 1:2 cation order perpendicular to the close-packed Sr(Ba)/O layers—with the exception of $Ba_3NiSb_2O_9$ and $Ba_3Ca_{1/2}Ni_{1/2}Sb_2O_9$, which crystallise in the hexagonal BaTiO$_3$ structure. Here, the sequence of the close-packed layers is of a mixed hexagonal–cubic type with the ratio 1:2. However, in all listed solids $A_3NiM_2O_9$ the cationic coordination of the oxygen atoms bonded to Ni^{2+} is that depicted in Fig. 23c, corresponding to a pseudooctahedral $M^V(OA_4)Ni$ entity.

In order to derive reliable e_σ and e_π parameters for Ni^{2+}, we consider the structural and spectroscopic properties of analogous Cu^{II} solids first. Because of the presence of a considerable Jahn–Teller distortion in these cases more experimental data are available, so that e_σ and e_π may be determined separately. The obtained AOM parameters should be transferable to the neighbour in the periodic table (Ni^{2+}) in the same type of solid, as was the case for the Sb^V trirutile phases considered above. Spectral energies [38] and structural data from powder neutron diffraction [39] for the solids $Sr_2CuM^{VI}O_6$ (M^{IV}: Te, W) and Ba_2CuWO_6 are collected in Table 5, the results for Sr_2CuTeO_6 being the most precise ones. The AOM parameters deduced from fitting the d–d spectra on the basis of the Cu–O spacings—here overlap integrals are used as before (Eq. (2))—and including LS coupling are listed for mean bond lengths a_e. The latter are not the geometrically averaged values, but refer to the *energetic* averages (Eq. (16)).

$$e_i = (e_i^{\parallel} + 2e_i^{\perp})/3; \quad i = \sigma, \pi \tag{16}$$

They readily account for the fact that the overlap integrals, and hence the bond energies as well, only gently decrease in the range of long metal–ligand spacings ($a_\parallel$, $e_i^\parallel$), while they sharply increase in the short bond region ($a_\perp$, $e_i^\perp$). Here, the symbols $\parallel$ and $\perp$ refer to the long axial ($\parallel z$) and short equatorial spacings ($\parallel x$, $\parallel y$) of the tetragonally elongated CuO_6 octahedron, respectively. The difference between the *geometrically* ($\bar{a}$) and *energetically* (a_e) averaged Cu–O spacings becomes more pronounced with increasing values of the radial distortion parameter ρ (Table 5). The latter is defined in Eq. (17), the δa_i ($i = x, y, z$) being the bond length deviations from the geometrical average $\bar{a}$.
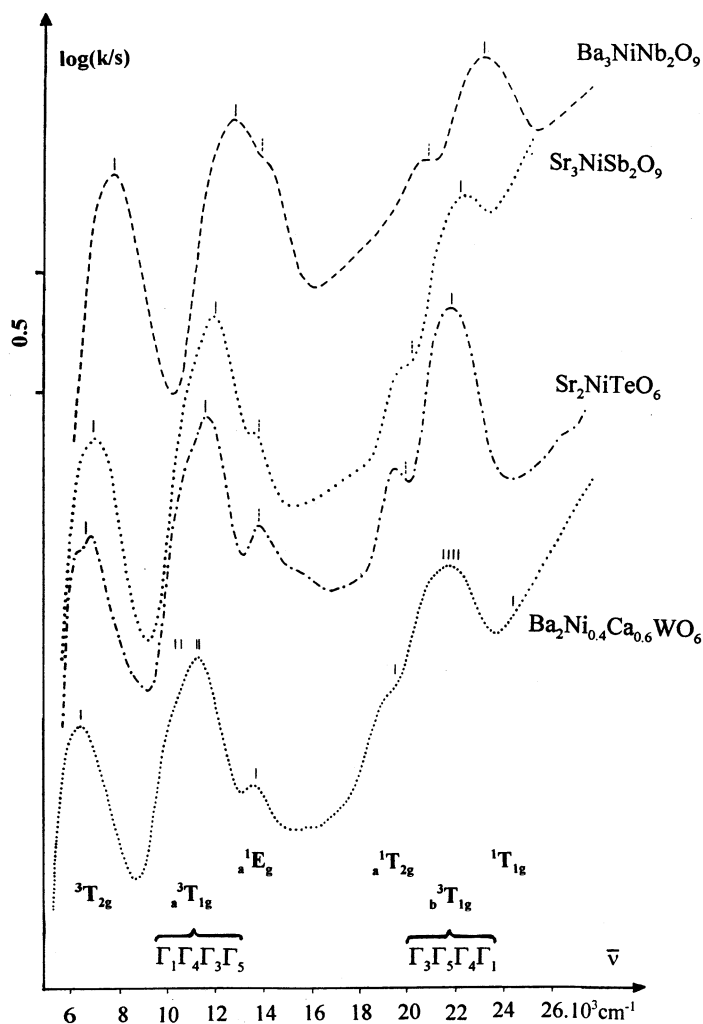

Fig. 24. d–d Spectra of Ni^{2+} in oxide ceramics with an ordered perovskite structure; fitting with the ligand field parameters of Table 5 ($C/B = 4.2$), for $Ba_2Ni_{0.4}Ca_{0.6}WO_6$ including LS coupling ($\xi = 550$ cm^{-1}, Bethe notation).

Table 5
Reported energies (in 10^3 cm^{-1}) of the d–d transitions (298 K) [38] and Cu–O bond distance data (Å) [39] for solids $Sr_2CuM^{VI}O_6$–Me^{VI}: Te (I), W (II)- and Ba_2CuWO_6 (III)[a]

	I	II	III
$\rightarrow\,^2A_{1g}$ (^2E_g)	8.0	8.2	7.6
$\rightarrow\,^2B_{2g}$ ($^2T_{2g}$)	8.7	9.9	9.6
$\rightarrow\,^2E_g$ ($^2T_{2g}$)	11.1	12.3	11.7
$a_\perp$ (4x)	1.97	1.94	1.98
$a_\parallel$ (2x)	2.34	2.29	2.42
$\bar{a}$ (6x)	2.09_5	2.05_5	2.12_5
ρ	0.43	0.40	0.51
e_σ	3.3	3.7	3.2
e_π	0.8_5	$\cong 0.8_5$	$\cong 0.6_5$
a_e	2.06_5	2.03	2.09

[a] Fitting AOM parameters (in 10^3 cm^{-1}) for mean spacings a_e (as defined in Eq. (16)) are also given ($\xi = 680$ cm^{-1}). ρ (Å) is the radial distortion parameter and $\bar{a}$ (Å) the geometrical mean of $a_\parallel$ and $a_\perp$.

$$\rho = \{2(\delta a_x^2 + \delta a_y^2 + \delta a_z^2)\}^{1/2} \tag{17}$$

For small ρ-values as in the case of $CuSb_2O_6$ ($\rho = 0.13$ Å), the difference between a_e and $\bar{a}$ becomes negligible.

Apparently e_π—which is spectrally reflected by only rather small splittings of the π-antibonding $^2T_{2g}$ term and hence not very precise—varies only a little in Table 5, while a very distinct increase of e_σ is noted when substituting $M^{VI} =$ Te by W in Sr_2CuMO_6. The AOM parameters for the former solid reproduce the Δ parameter of the corresponding nickel compound (Table 4) and can obviously be transferred directly, while slight adjustments of the AOM energies are necessary to yield the observed ligand field parameters Δ in the cases of Sr_2NiWO_6 and Ba_2NiWO_6 (Table 7). The reduced e_σ energy when substituting Sr^{2+} by the considerably larger Ba^{2+} cations seems to be mainly due to the $\sim 2\%$ larger Ni–O spacing.

The Δ values in Table 7 decrease by 1500–2000 cm^{-1}, if a d^0 is replaced by a d^{10} cation in a solid with an otherwise analogous constitution. If the Ni^{2+} site is expanded additionally by the partial substitution by Ca^{2+} the range of Δ values is extended down to 4900 cm^{-1}. The absorption minimum between the two $^3A_{2g} \rightarrow\,^3_{a,b}T_{1g}$ transitions is always located at least partly in the visible region and mainly colour-determining (Fig. 24). At low Δ values also the minimum following the third spin-allowed band is shifted into the visible region, if it is not obscured by charge-transfer transitions. Thus as has been analysed in the introduction (Fig. 1) an impressing colour shift is observed with increasing Δ and nearly constant Racah-parameters B,C. *This sequence is obviously also that of the AOM parameter* e_σ.

In order to explain the magnitude and the trend of e_σ for Ni^{2+} in the solids with ordered perovskite-type structures, we first notice the unique geometry around the oxygen atoms corresponding to a linear coordination with polarising charges of $+1$ (M^{VI}) or $+5/6$ (M^V) and $+1/3$ (Ni^{2+}) *directly opposite to each other* (Fig.

23c). In difference to the spinel (Ni_2GeO_4) case with effective charges $+1$ (Ge^{IV}) and $+1$ ($3Ni^{2+}$), the charges in this case are not even approximately balanced and suggest *a pronounced trans-effect within an asymmetric sp_z hybrid*. Such concept would readily explain the distinctly smaller e_σ energies in comparison with that of Ni_2GeO_4 and furthermore the increase of this parameter when substituting Te^{VI} or Sb^V by W^{VI} or Nb^V [Ta^V], because the comparatively stronger σ-interaction of a d^{10} cation with oxygen should lead to reduced e_σ energies in the Ni–O bond. Both effects are observed experimentally, the latter being reverse to that for the rutile-type solids (Tables 4 and 7). The cation order perpendicular to close-packed layers (Fig. 23b) apparently supports the trans-effect, making it cooperative throughout the structure.

We expect a trend for e_π, which is analogous to that observed in the case of the trirutile phases with Sb^V and Ta^V. The energetic differences should be smaller, however, because the π-(anti)bonding capacity for Ni^{2+} at any oxygen atom is comparatively much larger due to the presence of *two* $2p(\pi)$ orbitals and of only *one* high-valent cation. On the other hand the π-effect is presumably screened by the A cations, which are positioned in the p_x, p_y directions (Fig. 23c). Unfortunately e_π could not be determined with the same precision as in the trirutile case, where large band splittings in the d–d spectra were observed due to π-(anti)bonding anisotropies.

Our bonding concept is further supported by the d–d spectra of Ni^{2+}-doped perovskites $LaMg_{1/2}Zr(Sn)_{1/2}O_3$, which are disordered on the octahedral sites (Table 4, solids 11 and 12). The bands are very broad and the difference between the Δ values of the Zr^{IV} (d^0) and Sn^{IV} (d^{10}) solid is nearly vanishing.

We will proceed to discuss shortly solids $MMeF_6$ (M^{II}: Ni, Co, Mn, Fe; Me^{IV}: Ti, Hf, Zr, Sn, Pb) with the fluoride ion as the ligand, which crystallise in a slightly trigonally distorted variant of the $LiSbF_6$ structure [40]. The latter is an ordered version of the ReO_3 type and corresponds to elpasolites $A_2BB'O_6$ with unoccupied A positions. Thus we expect spectroscopic properties of solids $Ni(Co)MeF_6$ very similar to those of the oxidic compounds (Table 4) considered above. Fig. 25a shows the d–d spectra of the solids $NiMeF_6$, Me^{IV} being the d^0 and d^{10} configurated Hf and Sn cations, respectively. The Δ value seems to be slightly smaller in the case of the tin compound, but the shift is within the error limit of determining the band positions, even for the ${}^3A_{2g} \rightarrow {}_a^3T_{1g}$, ${}_b^3T_{1g}$ transitions, which depend on Δ with a factor of about 1.5. Passing to the corresponding Co^{2+} solids an analysis is more promising, because the ${}_a^4T_{1g} \rightarrow {}^4A_{2g}$ transition shows not only a stronger dependence on Δ (approximately a two-electron jump), but is practically independent on B as well. As depicted in Fig. 25b this transition shifts by ca. 600 cm^{-1} to

---

Fig. 25. (a) d–d Spectra (adopted from [41]) of solids $NiMeF_6$, fitting parameters $\Delta = 6950$ cm^{-1}, $B = 950$ cm^{-1}, $C/B = 4.2$; and (b) of mixed crystals $CoZr_{1-x}Sn_xF_6$. In the latter case the transition energies (above and below) were fitted with $\Delta = 7000$ and 6700 cm^{-1}, $B = 880$ cm^{-1}, $C/B = 4.5$ (the splitting of the ${}_a^4T_{1g}$ ground state by LS-coupling, $\xi = 485$ cm^{-1}-, has been taken into account).

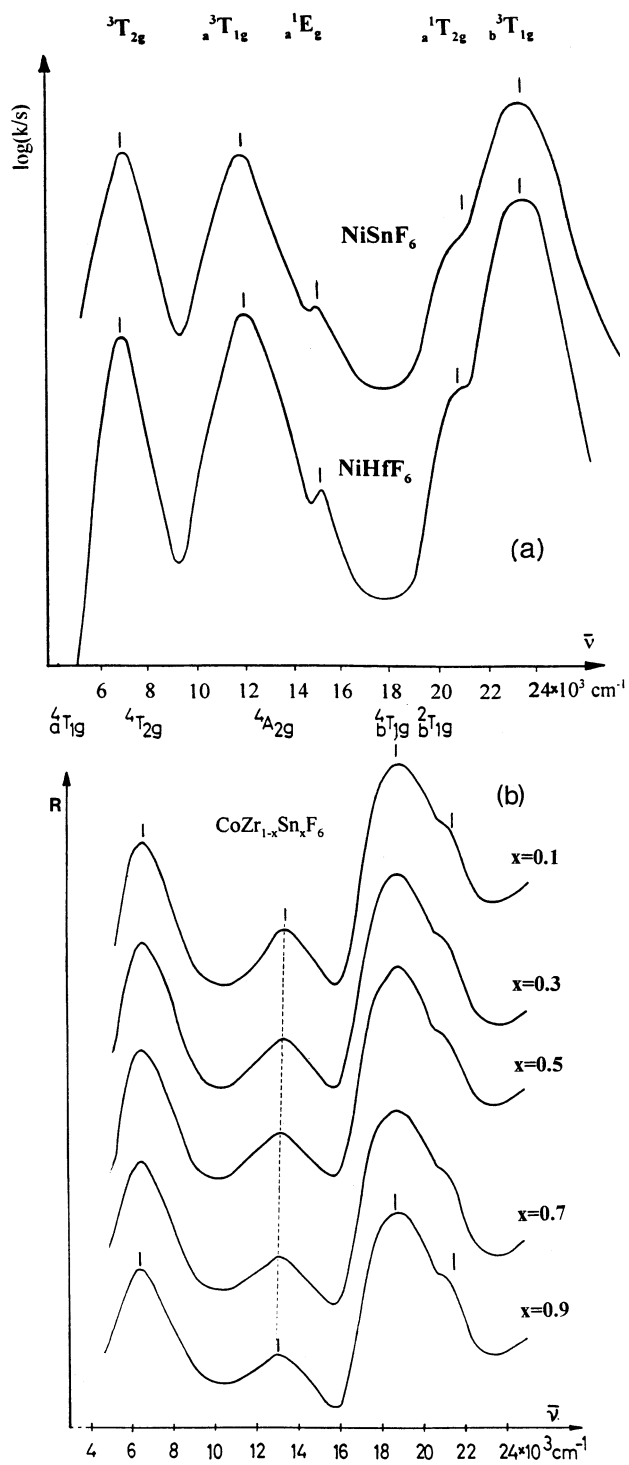Fig. 25.

lower energies with increasing x in the mixed crystal series $CoZr_{1-x}Sn_xF_6$, corresponding to a by nearly 300 cm^{-1} lower Δ value in the case of the tin compound. The spectra of the compounds with Ti^{IV} and Hf^{IV} on the Me position are nearly identical with the one of $CoZrF_6$. Apparently a bonding effect analogous to that deduced for $Sr_2NiM^{VI}O_6$ (M^{VI}: W, Te) occurs (Table 4), but extremely weakened in comparison with oxide ceramics. Because our concept implies, that this effect results from 3d covalency, it should indeed be small for an ionic ligand such as fluoride.

Passing to Cr(III) as the 3d cation one expects a considerably enhanced covalency. Elpasolite-type mixed crystals $Sr_2(Zn_{0.2}Ga_{0.8-x}Cr_x)(Me_{0.2}Me'_{0.8})O_6$ [Me^{VI}, Me$'^V$ = Te, Sb or W, Ta] have been reported [42] whose d–d spectra yield Δ values of $\cong 13000$ and ~ 16500 cm^{-1} in the case of the d^{10} cations Te^{VI}, Sb^V and for the d^0 configurated W^{VI}, Ta^V centres, respectively. As anticipated the bonding effect exceeds distinctly with $\sim 25\%$ that of Ni^{2+} in the same oxidic matrix. The rather complex composition of the solids has been chosen in order to have a sufficiently large ionic charge difference between the two octahedral sites in the elpasolite lattice, which only guarantees a cation order.

3.2. Columbite-type layer structures

Mixed phases of $Zn_{1-x}Ni_xNb_2O_4$ crystallise [43] in the columbite lattice (space group *Pbcn*), the latter being composed of hexagonally closed-packed oxygen layers. The metal ions occupy 75% of the octahedral sites between these layers extending parallel to the *bc*-plane, with an order of the di- and five-valent cations along the crystallographic *a* direction (Fig. 26). The cation distribution is similar to that in the ordered perovskites (Fig. 23b), though in contrast to that in the trirutile lattice. The latter is based also on a (very distorted) hexagonal close-packing of oxygen atoms, but the cation order does not follow the layers. The NiO$_6$ polyhedra in the columbite NiNb$_2$O$_6$ are of C_1 point symmetry only and tetragonally compressed in first approximation as in the (tri)rutile lattice (Fig. 27a). The cationic coordination is Ni(O1)Nb$_2$ for two and Nb(O2)Ni$_2$ for four of the oxygen atoms (Fig. 27b). Besides these (O3)Nb$_3$ polyhedra exist, which are not of interest in the context of this review though. Following the previous bonding concept we anticipate a sp and sp^2 hybridisation on O2 and O1, respectively, with two p orbitals available for π-overlap in the former case and only one in the latter. On the basis of the involved geometries (Fig. 27) the ligand field parameters for the Ni–O bond in NiNb$_2$O$_6$ obey the relations in Eq. (18), disregarding the tiny misalignment ($< 3°$) of the sp^2 hybrid orbital with respect to the Ni–O bond (Fig. 27b). Δ is the appropriately weighted sum of the e_i contributions from the sp hybridised O2 and the sp^2 hybridised O1 ligator atoms.

$$\Delta = 1/3\{3e_\sigma(sp^2) - 2e_\pi(sp^2)\} + 2/3\{3[\cos^2\beta e_\sigma(sp_z) + \sin^2\beta e_\sigma(p_{x,y})],$$
$$- 2e_\pi(p_{x,y}) - 2[\sin^2\beta e_\pi(sp_z) + \cos^2\beta e_\pi(p_{x,y})]\} \tag{18}$$
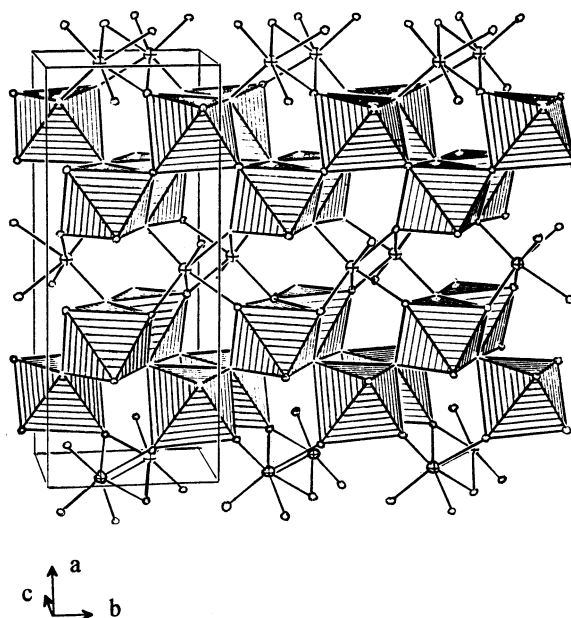
Fig. 26. The cation layers parallel to the hexagonally close-packed oxygen layers (the unit cell is indicated) in the columbite structure ($NiNb_2O_6$) (adapted from [43]; the M^VO_6 octahedra are fully drawn).

For the O2 atoms a calculational procedure analogous to that applied in the spinel and olivine case is used, β being the structural angle defined in Fig. 27c. Though the presence of a cation order perpendicular to close-packed anion layers (Fig. 26) might give rise to a *trans*-effect as in the ordered perovskite lattices, this is not considered as realistic, because the angles between the M^V–O and Ni–O bond vectors deviate strongly from linearity and also the effective charges polarising the O2 anions are nearly balanced [$+5/6$ (M^V) and $+2/3$ (2 Ni^{2+})], similar to the Ni_2GeO_4 case. Thus, the AOM parameters (Eq. (7a)) might be appropriate for O2, but with in particular strongly reduced $e_\sigma(sp_z)$ and $e_\sigma(p_{x,y})$ energies. Such a choice allows for the substitution of a cation with d^{10} configuration (Ge^{IV}) by a d^0 cation (Nb^V), which is expected to have a drastic effect on Δ and the AOM parameters, similar to that observed in the case of trirutile- and elpasolite-type oxidic solids (Table 7). For the sp^2-hybridised O1 atoms with a cationic coordination analogous to that in the trirutile lattice the AOM parameters for $NiTa_2O_6$ (Eq. (13)) can be suggested. One can indeed reproduce the band positions in the d–d spectra of $NiNb_2O_6$—and of $CuNb_2O_6$ (orthorhombic modification) as well (see below)— with a parameter set in accordance with these requirements. We refrain from presenting quantitative data, however, because—due to the C_1 symmetry of the metal and oxygen coordinations and the presence of two differently hybridised O1 and O2 atoms—this might be an overinterpretation. Estimated AOM parameters are listed in Table 7. The resulting Δ value is smaller than the one for the trirutile solids with d^0-cations on the M^V position. This is reflected by the red-shift of the

spectrum (Fig. 19) when passing from the high-temperature rutile modification of $NiNb_2O_6$ to the low-temperature phase with the columbite structure.

$MgWO_6$ has a structure closely related to the columbite lattice, but with a 1:1 cation order perpendicular to hexagonally close-packed oxygen layers (Fig. 26). The Ni^{2+} and oxygen polyhedron geometries are similar to those in Fig. 27 and accordingly the spectrum of $NiWO_6$ closely resembles that of $NiNb_2O_6$, displaying the same Δ-value.
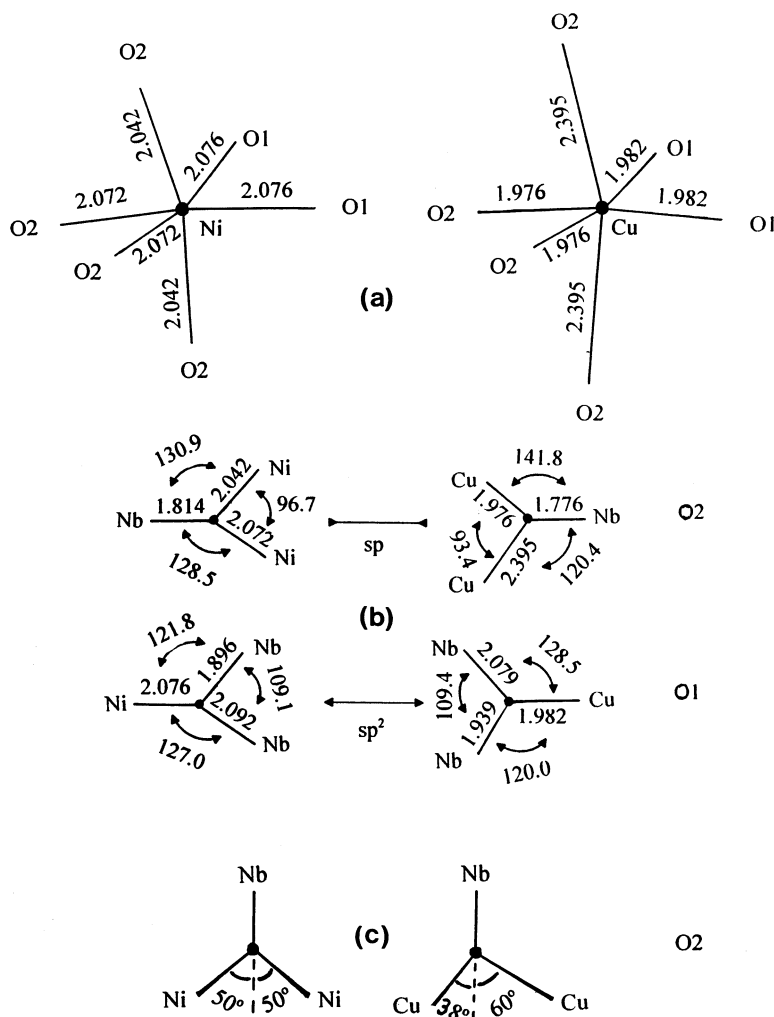
Fig. 27. The geometries of the $NiO_6(CuO_6)$ polyhedra (a) and of the cationic coordination of the oxygen atoms O1 and O2 (only approximately planar) (b) in the orthorhombic columbites $NiNb_2O_6(CuNb_2O_6)$; spacings (Å) and angles (°) from [43] ([44]). The angles between the sp_z lone pair on the O2 atoms and the two M–O2 bonds are $\beta = 50._5(1._0)°$ for Ni, but strongly diverging for Cu (c). The angle between the sp^2 hybrid orbital and the Ni(Cu)–O1 bond is 2.6(4.3)°.
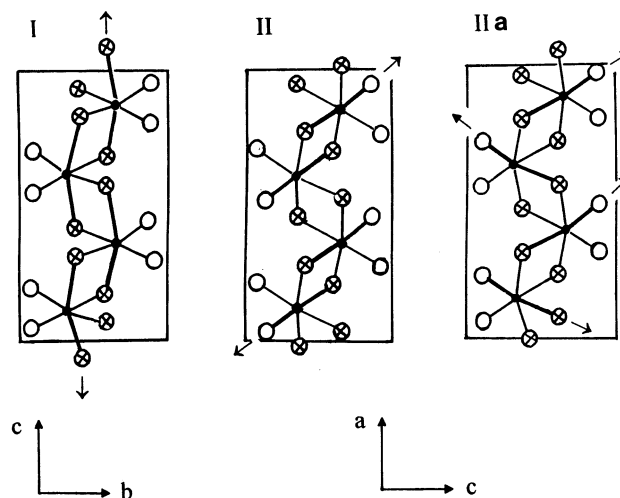
Fig. 28. The structures of $CuNb_2O_6$: projections of the edge-connected chains of CuO_6 polyhedra in one of the Cu^{2+} layers of the columbite lattice onto the $bc(ca)$ plane for the orthorhombic (I) and monoclinic modification (II, IIa), respectively (note the different notations of the crystallogr. axes in the two phases!); II refers to [47], IIa is suggested from EPR data (see text). The O2 atoms are crossed, and the long Cu–O axes are marked by bulky lines and arrows.

In the orthorhombic phase of $CuNb_2O_6$ a very distinct elongation of the CuO_6 octahedra due to Jahn–Teller coupling is observed [44], the preferred axis being that along the bonds with O2 in transposition (Fig. 27a). The long axes are slightly bent and oriented parallel to each other (*ferrodistortive* [45]) in either one of the two Ni^{2+} layers in the unit cell (Fig. 26) and located approximately in the *ac* plane with an inclination of $\cong +30°$ with respect to *c* in one layer and $\cong -30°$ in the other one. This is visualised by the projection of the chain of edge-connected CuO_6 polyhedra in one layer onto the bc plane (Fig. 28 I), where the long O2–Cu–O2 spacings are marked by thick lines. Because the two Cu^{2+} layers are separated from each other by two layers of Nb^VO_6 octahedra—shortest Cu–Cu spacings 3.2 and 7.5 Å within one layer and between the layers, respectively—the magnetic coupling between the differently oriented polyhedra of these two layers (canting angle $2\gamma \cong 60°$) is only very weak. This is concluded from the EPR spectrum, showing the characteristics of tetragonally elongated octahedra with a small orthorhombic symmetry component [46]. The d–d reflection spectrum is rather broad, the given assignment being suggested by the AOM calculations (Fig. 29a, Table 6).

Inspecting the cationic O2 coordination in $NiNb_2O_6$ and $CuNb_2O_6$ (Fig. 27b) more closely an interesting feature is revealed. While in the former compound the sp hybrid orbital (hatched line in Fig. 27c) is projected with an angle of $\beta \cong 50°$ on the two Ni–O2 bond directions, the steric situation is rather different in $CuNb_2O_6$. Here the angle of projection is distinctly smaller (38°) for the short Cu–O2 bond and much greater (60°) for the long Cu–O2 spacing. This stereochemical change when switching from Ni^{2+} to Cu^{2+} obviously supports the vibronic coupling,

weakening one Cu–O2 σ-bond and strengthening the other one. The thus created bonding anisotropy effect can be considered as a host site strain, which enables the *trans* O2–M–O2 bond lengths—the short Ni–O2 spacings in the case of Ni^{2+}—to become the axis of elongation for $M = Cu^{2+}$ (Fig. 27a). This view is in perfect agreement with our supposition of a sp hybridisation on the O2 atoms. The described structural phenomenon—the angular change at the O2 atoms and the bond length changes along Cu–O2—are most certainly correlated. We refer to Sections 2.2 and 2.4, where similar correlation effects were analysed.

$CuNb_2O_6$ is dimorphous, the orthorhombic modification being thermodynamically slightly more stable than the monoclinic phase [47]. For the latter the space group $P2_1/c$ is proposed by neutron diffraction powder analysis [47]. The structure is described to be of a slightly distorted columbite-type as noticed before [34], in which the CuO_6 polyhedra are elongated along one of the two O2–Cu–O1 bond directions (compare Fig. 27a), *perpendicular to the axis of elongation in orthorhombic* $CuNb_2O_6$. The long axes are proposed to orient parallel to each other in one Cu^{2+} layer (ferrodistortive order) [47], as is indicated in Fig. 28 II. However, in the second layer the elongation switches to the alternative O2–Cu–O1 bond direction giving rise to an approximately *antiferrodistortive order* in the complete unit cell. The canting angle between the directions normal to the best equatorial planes of the short Cu–O bond lengths in the two layers is $2\gamma \cong 70°$. The different cooperative Jahn–Teller order in the two $CuNb_2O_6$ modifications is reflected by the changes of the unit cell constants in comparison to those of $ZnNb_2O_6$ (Table 6). While the

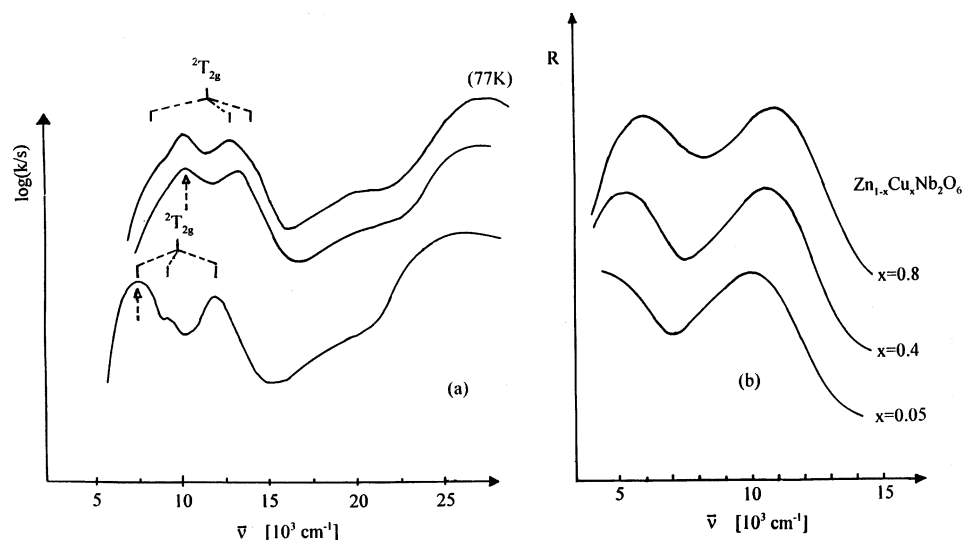Fig. 29. The powder reflection spectra at 298 K (lower temperatures indicated) of mixed crystals $Zn_{1-x}Cu_xNb_2O_6$: (a) $x = 1.0$ (log k/s intensity scale): orthorhombic (above) and monoclinic phase (below); tentative band assignment by octahedral parent terms (dotted arrows denote the transition within the ^2E_g ground term); (b) solids with varying x, intensity in reflectance units (arbitrary).

Table 6

Energies (10^{-3} cm^{-1}) of the d–d transitions, Cu–O bond length data and distortion parameters (Å) for $CuNb_2O_6$, orthorhombic (I) and monoclinic (II) modification; the unit cell parameters (Å)[a] for I, II and $ZnNb_2O_6$ (III) are also given

	I[b]	II[c]
$^2_aA_1(^2E_g) \rightarrow {}^2_bA_1(^2E_g)$	9500	$\cong 7500$
$\rightarrow {}^2_cA_1(^2T_{2g})$	$\cong 8000$	$\cong 7500$
$\rightarrow {}^2_dA_1(^2T_{2g})$	12 000	9100
$\rightarrow {}^2_eA_1(^2T_{2g})$	$\cong 13\,500$	12 000
$a_\perp$	1.98 (4x)	1.96 (2x)
		2.02$_5$ (2x)
$a_\parallel$	2.39$_5$ (2x)	2.31 (2x)
$\bar{a}$	2.12 (6x)	2.10 (6x)
ρ	0.48	0.37

	$a_o = b_m$	$b_o = c_m$	$c_o = a_m$	β_m	V (Å^3)
I	14.10	5.61	5.12	–	405.$_0$
II	14.19	5.72	5.03	–	408.$_3$
III	14.17	5.76	5.01	91.7°	408.$_7$

[a] o, orthorhombic; m, monoclinic.
[b] Assignment suggested from AOM calculations.
[c] Tentative assignment.

lattice parameter c of orthorhombic $CuNb_2O_6$, which is determined predominantly by the long Cu–O2 spacings, is expanded strongly by $\cong 2\%$, in particular b is reduced in length. For the unit cell constants of the monoclinic phase a reverse trend and much smaller changes are observed. Due to the symmetry lowering there are four different cationic oxygen coordinations in monoclinic $CuNb_2O_6$, in comparison with the two in orthorhombic $Cu(Ni)Nb_2O_6$ (Fig. 27b).

We were not able to fit the d–d powder spectrum of monoclinic $CuNb_2O_6$ (Fig. 29a, Table 6) even approximately with the parameter set used for $NiNb_2O_6$ and orthorhombic $CuNb_2O_6$, though the structure type and the constitution of the cationic oxygen environment are identical. We think that the reason might be a cooperative Jahn–Teller order, which is slightly different from that proposed in [47]. EPR spectroscopy reveals an antiferrodistortive order, but it is suggested also from these measurements [46], and is discussed in greater detail below, that the perpendicular orientation of the elongated O2–Cu–O1 bond lengths occurs *within each pair of edge-connected octahedra in the same layer*—as depicted in Fig. 28 IIa. The realisation of this type of cooperative order demands a further symmetry lowering of the unit cell. It is not excluded in [47], that this might be the case, because an anisotropic refinement of the temperature factors in particular of Cu^{2+} was not possible in the space group $P2_1/c$.

The mixed crystal series $Zn_{1-x}Cu_xNb_2O_6$ has been spectroscopically investigated thoroughly and by X-ray diffraction [34,46]. While the solids crystallise in the space group *Pbcn* below $x \approx 0.4$, a monoclinic distortion occurs above this critical

concentration. However, in the case $x = 1.0$ the monoclinic phase can only be obtained when applying low sintering temperatures around 700°C [44]. At higher reaction temperatures orthorhombic $CuNb_2O_6$ is formed.

The low temperature EPR spectra (Fig. 30b) indicate compressed CuO_6 polyhedra at very low doping levels ($g_\parallel \cong 2.00_5$, $g_\perp = 2.34_5$) and are very similar to those of Cu^{2+} in the structurally analogous $MgWO_4$ host (vide supra), where the $g_\parallel$
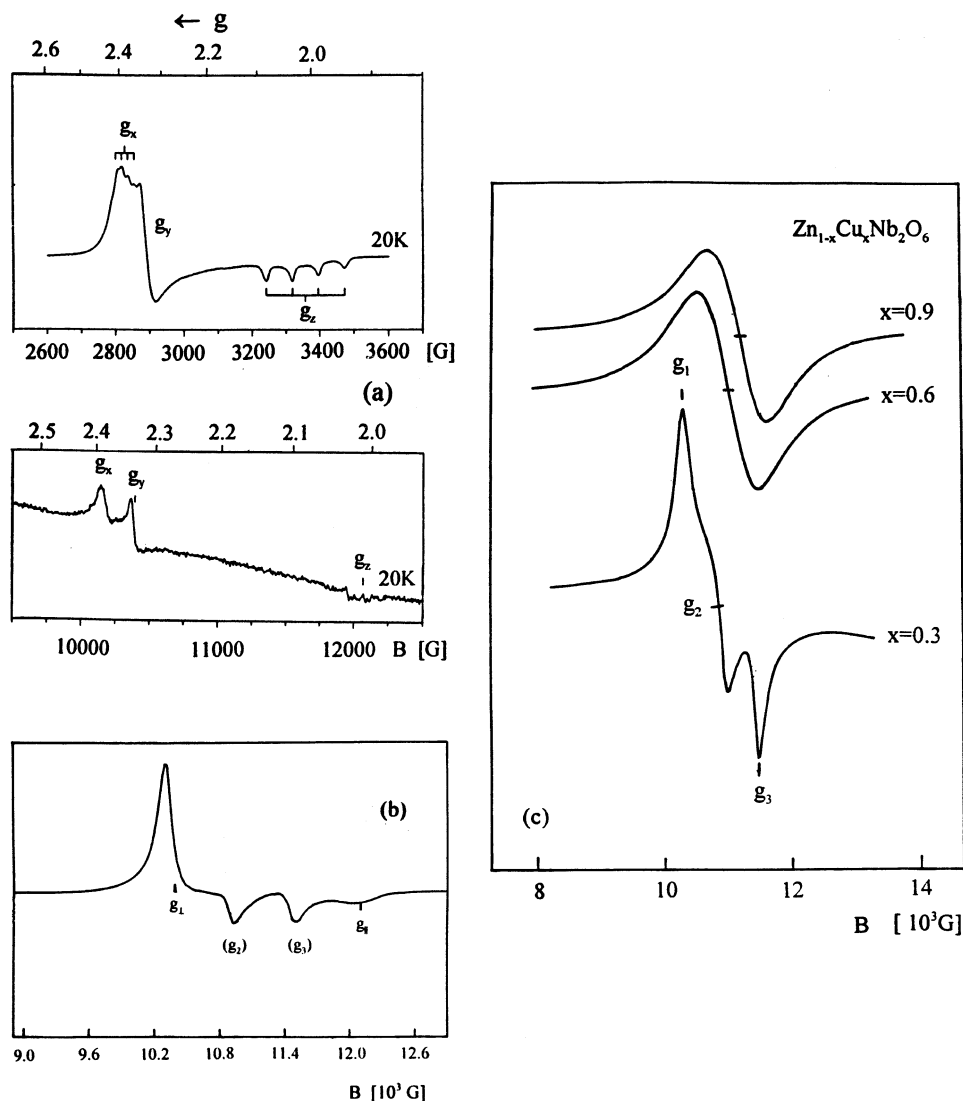

Fig. 30. EPR spectra of Cu^{2+}-doped $MgWO_6$ (1 mol%) (a), $ZnNb_2O_6$ (5 mol%) (b) and of mixed crystals $Zn_{1-x}Cu_xNb_2O_6$ (c). g- and A-tensor components for (a), (b) and ($x = 0.3$) are given in the text, the g_{av} values for $x = 0.3$, 0.6 and 0.9 are 2.23, 2.20 and 2.17, respectively.

hyperfine structure (X band) and a small orthorhombic distortion component (Q band) are nicely resolved (20 K: $g_z = 2.011$, $g_y = 2.335$, $g_x = 2.390$; $A_z = 72.6$, $|A_y| \approx 0$, $A_x \cong -20 \times 10^{-4}$ cm^{-1}; Fig. 30a). They show two additional distinct features (g_2, g_3 in Fig. 30b), which increase in intensity with x becoming larger, while the spectrum of the compressed polyhedra becomes weaker. In the range $0.25 \leq x \leq 0.40$ the latter spectrum has vanished and only the well-resolved 'additional' spectrum remains [$g_1 \cong g_{\parallel} = 2.35$, $g_2 \cong 2.23$, $g_3 = 2.11$] (Fig. 30c). It can be consistently explained as being caused by exchange-coupled *elongated* octahedra with a nearly perpendicular orientation of the long axes (canting angle $2\gamma \approx 70°$) [46]. Because the exchange-coupled signals are already present at very low Cu^{2+} concentrations they should be due to paramagnetic centres in the same layer, rather than to Cu^{2+} ions in different layers with large interionic distances. Thus, we have the interesting stereochemical situation, that vibronic coupling leads to a *compressed* geometry (enforced by a host site strain with the same sign of distortion, see the NiO_6 polyhedron in Fig. 27a) for *isolated* CuO_6 polyhedra, while a drastic change to an *elongated* polyhedron geometry occurs, if neighboured octahedral sites are occupied by Cu^{2+}. The possibility for such Cu^{2+} pairs to have their preferred axes oriented (nearly) perpendicular with respect to each other reduces the elastic energy, which is necessary for the oxygen and copper nuclei to move along a certain distortion path, and allows to switch from the compressed to the vibronically more favourable elongated conformation ([28]). Above the critical Cu^{2+} concentration of the orthorhombic-to-monoclinic phase transition ($x \approx 0.4$) the spectrum smears out to a broad signal even at lower temperatures, which shifts to smaller g-values with increasing x (Fig. 30c). This is in accord with a corresponding higher-energy shift of the d–d transitions (Fig. 29b). Both observations indicate a more pronounced Jahn–Teller distortion of the local CuO_6 octahedra, if Cu^{2+} progressively substitutes the non-Jahn–Teller cation Zn^{2+} in the concentration region above $x = 0.4$. This is clearly a cooperative effect, induced by the long-range approximately antiferrodistortive order pattern in the monoclinic phase, which we propose to be that of Fig. 28 IIa. A cooperative effect of this kind is favoured in structures with CuO_6 polyhedra, which form separate sheets in the lattice (Fig. 26). It is not present in mixed crystals $Zn_{1-x}Cu_xSb_2O_6$ (Section 2.4.2), because the CuO_6 polyhedra are imbedded in an environment of rigid NbO_6 octahedra in the trirutile lattice, where a cation order perpendicular to close-packed oxygen layers does not exist.

The Jahn–Teller distortion of the CuO_6 octahedra is markedly smaller in the monoclinic than in the orthorhombic phase, as can be infered from the d–d transitions, which are considerably blue-shifted in the latter case (Fig. 29a). The elastic strain, which counteracts the tendency of Cu^{2+} for strong local and cooperative vibronic interactions (CuO_6 polyhedron and unit cell distortion, respectively), is more pronounced in the orthorhombic than in the monoclinic phase, because the changes of the lattice parameters as compared to those of $ZnNb_2O_6$ are larger in the former case (Table 6). It is apparently the bonding anisotropy induced by the angular change of the O2 coordination when switching from $NiNb_2O_6$ (or monoclinic $CuNb_2O_6$) to orthorhombic $CuNb_2O_6$ (Fig. 27c), which favours the considerably increased local Jahn–Teller distortion, thus over-compensating the stronger elastic strain.

Table 7

AOM (e_σ, e_π) and ligand field (Δ) parameters (in 10^3 cm^{-1}) of various oxide ceramis with Ni^{2+} [a]

		$\bar{a}$	e_σ	e_π	Δ	Structure	cc	
Ni_2GeO_4		$204._5$	4.9	1.4_5	8.9	Spinel	$Ge^{(4)}ONi_3^{(6)}$	sp
$ZnNiSnO_4$		–	3.0	$\cong 0$	8.9		$Zn^{(4)}O(Sn,Ni)_3^{(6)}$	sp^3
$LiNiPO_4$		$208._5$	$\cong 3.9_5$	$\cong 1.0$	$\cong 7.9$	Olivine	$P^{(4)}O(Li,Ni)_3^{(6)}$	sp
$NiCO_3$		$207._5$	$\cong 3.9$	$\cong 0.6$	9.2	Calcite	$C^{(3)}ONi_3^{(6)}$	sp
$Zn_{1-x}Ni_xSb_2O_6$		$\cong 207$	3.5	0.6_5	9.1_5	Trirutile	$Sb_2^{(6)}ONi^{(6)}$	sp^2
$NiTa_2O_6$		207	$\cong 2.9$	$\cong 0.3_5$	8.0		$Ta_2^{(6)}ONi^{(6)}$	sp^2
Sr_2NiTeO_6		204	3.3	0.8_5	6.6	Elpasolite	$Te^{(6)}OSr_4^{(12)}Ni^{(6)}$	sp
Sr_2NiWO_6		204	$\cong 4.0$	$\cong 0.8_5$	8.5		$W^{(6)}OSr_4^{(12)}Ni^{(6)}$	sp
Ba_2NiWO_6		$\cong 209$	$\cong 3.3$	$\cong 0.6_5$	7.3_5		$W^{(6)}OBa_4^{(12)}Ni^{(6)}$	sp
$Zn_{1-x}Ni_xNb_2O_6$	O1	$207._5$	≈ 2.9	$\approx 0.3_5$	$\cong 7.3$[b]	Columbite	$Nb_2^{(6)}ONi^{(6)}$	sp^2
	O2	206	≈ 4.0	$\approx 1.2_5$			$Nb^{(6)}ONi_2^{(6)}$	sp

[a] The cationic oxygen coordination cc (the upper indices in parentheses give the coordination numbers with respect to oxygen) and the assumed type of 2s–2p hybridisation on oxygen are indicated; $\bar{a}$ (Å) is the average Ni–O spacing.

[b] Weighted average of O1 and O2.

3.3. Analysis and discussion

Table 7 gives an overview of the AOM parameters for Ni^{2+} in the octahedral sites of various oxidic host solids. They were derived from the d–d spectra utilising optical and EPR results for Cu^{2+} in the same hosts for comparative purposes. Though some empirical and intuitive arguments were used, in particular to reduce the number of independent bonding parameters, we consider the collected e_σ and e_π parameters as broadly correct. Reliable in any case are *the trends in dependence on the structure and chemical composition* of the respective oxide ceramic.

The cationic coordination of the oxygen atoms, which bridge the polyhedra in the extended network of the solid structures, seems to play a crucial role. We have presented far-reaching experimental evidence for the influence of the second-sphere coordination of oxygen ligator atoms in the preceding chapters, and this may justify the terminology used in the title of this article. If small cations M (radius r) of high oxidation states (n) and in an environment of low coordination number (N) are present besides say Ni^{2+}, oxygen is polarised strongly by effective ion potentials P_{eff} (Eq. (19)), if an ionic approach is applied.

$$P_{eff} = ne/Nr \tag{19}$$

Hence, these cations are predicted to use a disproportionately large part of the bonding capacity of oxygen and to determine predominantly the bonding properties of the oxygen ligator atoms. Depending on the P_{eff} values, the coordination number and the geometry of the oxygen environment, widely differing e_σ (and e_π) energies are indeed expected, in agreement with the data in Table 7. Following such a bonding concept, sp, sp^2 or sp^3 hybridisation is assumed on the oxygen ligator

atoms, the former two being appropriate, if one or two high-valent cations are present in the oxygen coordination sphere, respectively, while the latter refers to a situation with charges distributed equally. We have demonstrated that a valence description on this basis allows to fit the spectral data even in cases where the conventional AOM fails. Thus, the very large band splittings in the d–d spectra of Ni_2GeO_4 in spite of nearly undistorted NiO_6 octahedra could be accounted for by a bonding anisotropy effect, connected with a sp hybridisation along the Ge–O bond (Section 2.1). Similarly, the distinct splittings in the d–d spectra of trirutile mixed crystals $Zn_{1-x}Ni_xSb_2O_6$—and the g-tensor properties of the corresponding Cu^{2+} solids as well—could only be explained by the presence of anisotropic π-contributions in the Ni–O bond, caused by a sp^2 hybridisation within the planar Sb_2ONi coordination (Section 2.4). Though all data result from powder spectra (in usually high resolution), we have selected mostly examples where the symmetry effects and the band shifts were very distinct.

The idea to analyse and interpret the optical properties of transition metal ions in an ionic model via the action of contrapolarising forces of high-valent cations on the ligator atoms was introduced first by Neuhaus in the case of oxidic Cr^{III} solids [48]. This concept was later taken up and deepened by Blasse [49] and Reinen [7,24,34], considering in particular the bonding effects when substituting a d^0 by a d^{10} cation. Furthermore, the slightly more pronounced covalency of a 4d compared to a 5d cation—as evidenced by the nephelauxetic series of ligands [1]—was used by Blasse to explain the different crystal-chemical properties of for example Nb^V $(4d^0)$ and Ta^V $(5d^0)$ [49,50]. While the more ionic Ta^V tries to avoid too many further tantalum neighbour contacts—$NiTa_2O_6$ crystallises in the trirutile lattice—Nb^V behaves differently; the stable modification of $NiNb_2O_6$ is of the columbite type, where in contrast to the trirutile structure oxygen polyhedra OM_3^V exist besides others (see Sections 2.4 and 3.2).

As already mentioned in Section 1, the derived AOM energies in Table 7 have to be regarded as effective parameters, which reflect not only the weak covalent d–d overlap within the Ni–O bond, but comprise electrostatic interactions as well. Though all so-far attemps to quantify this aspect failed, Table 7 illustrates clearly by the very distinct 'd^0/d^{10} effect' that the former contributions are presumably significant. Apparently polarisable cations with a d^{10} configuration, such as Sb^V and Te^{VI} are more covalently bonded to the oxygen ligator atoms than the more ionic and rigid d^0 configurated Ta^V, Nb^V and W^{VI} centres. This bonding property is imparted to the Ni–O interaction via the oxygen hybrids, inducing by about 15% larger e_σ energies for Ni^{2+} in the former case in trirutiles, though the ionic radii of the M^V or of the M^{VI} cations do not differ significantly. A similarly large effect is observed in perovskite-type solids, but with a reversed trend. This has been explained by a local trans-effect, which becomes cooperative in this kind of lattice due to the cation order perpendicular to close-packed oxygen layers. The presence of a *trans*-effect is indicated further by the magnitudes of the AOM parameters of for example the elpasolites Sr_2NiWO_6 and Sr_2NiTeO_6, which are rather small in comparison to those of Ni_2GeO_4, where also sp hybridisation on oxygen occurs.

As Table 7 further visualises, the AOM parameters are not simply transferable from one oxidic solid to the other. They have this property however, if finer criteria such as the crystal structure and the geometry and composition of the cationic oxygen coordination are referred to. Then even the bonding parameters of cations neighboured in the periodic table such as Cu^{2+} and Co^{2+} are roughly interchangable with those of Ni^{2+}.

The e_σ energies collected in Table 7 are distributed over a much larger range of magnitude ($\pm 25\%$) than the ligand field parameter Δ ($\pm 15\%$), the latter being an apparently less sensitive probe for the Ni–O bond covalency than the former. The data further visualise, that the generally assumed e_σ/e_π ratios between 4 and 6 are not necessarily correct, but may be smaller or even much larger, depending on the discussed bonding characteristic of oxygen. After all Δ is a rather complex bonding parameter, which reflects the interplay of σ- and π-interactions on the one hand, but is influenced strongly by the *effective electronegativity* of oxygen towards the transition metal ion on the other hand. This effective electronegativity is modeled by the other cations in the coordination sphere of the oxygen atoms. We will come back to this point in the following chapter.

It might be interesting to speculate about the AOM parameters of a simple compound such as NiO, where according to the high structural and spectral symmetry e_σ and e_π cannot be determined independently. The octahedral cationic ONi_6 coordination of oxygen in the NaCl-type lattice can be directly compared with that in the Ni_2GeO_4 spinel ($GeONi_3$), when substituting three Ni^{2+} ions by Ge^{IV} with the same effective charge (Fig. 4a). Thus, we may suggest AOM parameters for NiO similar to those for Ni_2GeO_4: $e_\sigma \approx 5000$ cm^{-1} and $e_\pi \approx 1500$ cm^{-1} (Table 7).

The performed AOM considerations not only involve basic science but are useful in applied chemistry as well. If one knows the principles how to steer the magnitudes of e_σ, e_π and Δ by the proper choice of suitable oxidic host solids with certain structural and constitutional properties, one may vary the colour of the compounds in an aimed way. Because the d–d transitions of transition metal ions such as Ni^{2+}, Co^{2+} and Cr^{3+} are usually located in the visible region, the colour changes are sometimes quite spectacular (Fig. 1 and Introduction), with some of these solids being potential inorganic pigments.

We think that the angular overlap model in its semiempirical form is able—despite its theoretical weaknesses—to reflect essential properties of the transition metal–ligand bond, meeting the line of the chemists' thinking in a lucky way. As we have tried to demonstrate, it can even reveal finer details, if it is applied in a more sophisticated approach. In the last chapter we will critically inspect in particular the Racah-parameters deduced from the d–d spectra of Ni^{2+} and Cr^{3+} and the mixing coefficient α in the ground state MO of Cu^{2+} derived from EPR spectroscopy, whether they give additional and reliable informations about the bond covalency.

Finally the remark seems necessary, that the AOM parameters are concerned only with the d–d contributions to the transition metal–ligand bond. It is usually assumed, however, that they give a good image of the symmetry and the covalence of the bond as it is.

4. The transition metal–oxygen bond covalency

4.1. Bonding parameters from spectroscopy

Table 8 comprises bonding parameters for the M–O bond (M(II) = Ni, Cu) in various oxidic solids, from which most were considered in the preceding chapters. Here α, κ and φ refer to Cu^{2+}, substituted isomorphously into the octahedral Mg^{2+} or Zn^{2+} positions. The mixing coefficient α represents the metal contribution in the one-electron wave function, which characterises the MO ground state of Cu^{2+} in a ligand field of tetragonal or orthorhombic symmetry (Eq. (20)) and is a relative measure for the d-covalency in the copper–ligand bond.

$$\psi_g = \alpha(\cos(\varphi/2)d_{x^2-y^2} + \sin(\varphi/2)d_{z^2}) - \alpha'L \tag{20}$$

The angular parameter φ determines the geometry of the Cu^{2+} coordination, with $\varphi = 0°$ (120°, 240°) and $\varphi = 180°$ (300°, 60°) corresponding to tetragonally elongated and compressed octahedra along the molecular $z(x, y)$ axes, respectively, and φ angles deviating from these values to orthorhombic polyhedron geometries [45]. L comprises the proper symmetry adapted ligand LCAO's. By using the master Eq. (21) [56] α can be deduced from the copper hyperfine structure in the EPR spectra, which is frequently resolved at low doping levels of Cu^{2+} in the host compound (Figs. 9, 11, 16 and 30a), depending on how careful the synthesis is performed.

$$A_z/P = (-\kappa - 4/7\cos\varphi)\alpha^2 + \delta g_z + (\delta g_x/14)\cdot(3 - 2\sqrt{3}\sin\varphi)/(2\cos\varphi - 1)$$
$$+ (\delta g_y/14)\cdot(3 + 2\sqrt{3}\sin\varphi)/(2\cos\varphi - 1) \tag{21}$$

The δg_i ($i = x, y, z$) are the deviations of the experimental g-tensor components from the spin-only value $g_0 = 2.0023$. A_x and A_y are generated by the cyclic permutation of the δg_i ($i = x \to y \to z$) and by raising φ by 120° every time. The generally used values for P and the Fermi contact term κ (3d) are 0.036 cm^{-1} and 0.43 for the free Cu^{2+} ion. If d_{z^2} participates in the ground state wave function, interaction with the 4s metal orbitals is possible by symmetry. The experimental κ value decreases in this case because κ (4s) is strongly negative (-5.56) [51]. The coefficient γ, by which 4s mixes into the ground state wave function, can be estimated using Eq. (22).

$$\gamma \cong \alpha\{(\kappa - \kappa(3d))/\kappa(4s)\} \tag{22}$$

Any reduction of κ with respect to 0.43 (Table 8) hence indicates an admixture of d_{z^2} with the ground state, either by static or by dynamic distortion effects. In cases, where the hyperfine structure is well resolved in all three g_i ($i = x, y, z$) signals, α, κ and φ can be unambigously determined, if the signs of the hyperfine tensor components, which cannot be simply deduced from the spectra, are chosen such that only physically meaningful solutions are admitted. In cases of less resolved hyperfine structures the listed α values (Table 8: $\cong$) are approximate. Eq. (21a) gives the isotropic contribution to the hyperfine coupling, and Fig. 31 displays the φ dependence of the A_i's ($i = x, y, z$) for typical values of κ and of the orbital contributions δg_i to the g-tensor components.

Table 8

Nephelauxetic ratios β for Ni^{2+} and mixing coefficients α in the ground state MO of Cu^{2+} (Eq. (21)) for various oxidic solids and compounds with F, N and S ligator atoms (for the purpose of comparison); the Fermi contact terms κ and the angular distortion parameters φ are also given for Cu^{2+} (see text)

	β	α	κ	φ (°)	Structure	Ref.
Ba_2ZnF_6	0.91_5	0.92^e	0.27	60	K_2NiF_4-related	[51]
$K_2[Zn(OH_2)_6](SO_4)_2$	$\cong 0.91$	0.91^e	–	–	Tutton salt	[52]
$LiMgPO_4$	0.88_5	0.95	0.28	37	Olivine	j
$Mg_3(PO_4)_2$ [a]	$\cong 0.88$	$\cong 0.93$	$\cong 0.30$	$\cong 34$	–	j
Mg_2SO_4	0.88_5	0.95	0.22	56	α-Mg_2SO_4	j
Mg_2SiO_4 (C_i site)	–	$\cong 0.93$	$\cong 0.26$	$\cong 20$	Olivine	j
$MgCO_3$	0.85_5	0.92	0.29	5	Calcite	j
$Mg_3(BO_3)_2$ [a]	0.84_5	0.92	0.29	17	–	j
$ZnSb_2O_6$	0.83^c	0.91	0.29	60	Trirutile	[35,42]
$MgWO_4$	0.83	0.88	0.25	49	Wolframite	j
Sr_2ZnWO_6	0.82_5	$\cong 0.88$	$\cong 0.30$	4	Elpasolite	[53]
La_2ZnTiO_4	d	$\cong 0.88$	$\cong 0.29$	4	Elpasolite	[53]
Ba_2ZnWO_6	0.82_5	$\cong 0.85$	$\cong 0.30$	4	Elpasolite	[53]
$LaSrGaO_4$ [b]	$\cong 0.82$	$\cong 0.86$	$\cong 0.43$	0	K_2NiF_4	[54]
Y_2BaZnO_4	–	0.84	0.43	0	–	[54]
$M(TACN)_2^{2+}$	0.82_5	0.86_5	0.43	0	NH^h	[55]
$M(NO_2)_6^{4-}$	d	0.87^f	–	–	NO_2	[56]
$M(TTCN)_2^{2+}$	$\cong 0.77$	0.74	0.43	0	S^h	[55]
$M(dtc)_2$	–	$\cong 0.73^g$	–	–	S^i	[57]

[a] For one of the two sites.

[b] Coupled substitution of Sr/Ga by La/Cu.

[c] Value for $NiTa_2O_6$.

[d] B dependent d–d transitions obscured by low-lying charge-transfer bands.

[e, f] The α' coefficient in Eq. (20), deduced from the ligand hyperfine structure in the EPR spectrum is: ~ 0.47 [51,52] and $\cong 0.63$ [56], respectively.

[g] The α' coefficient in Eq. (20), deduced from extended Hückel LCAO calculations on the basis of EPR data is: ~ 0.8 [57]).

(h)   triaza(trithia)cyclononane - tridentate

TACN   TTCN
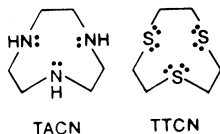
(i)   dithiocarbamate - bidentate
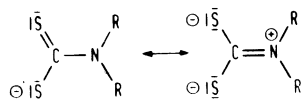
(j)   This study and S.L. Lee, Diploma (1992) and Doctoral Thesis (1996), Marburg
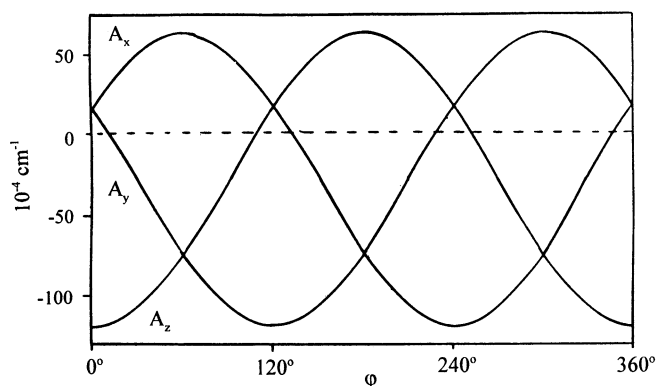
Fig. 31. φ-Dependence of the main A-tensor components (in 10^{-4} cm^{-1}), using Eq. (21) and $P = 0.036$ cm^{-1}, $\kappa = 0.3$, $\bar{g} = 2.18$ (φ determines the magnitudes of the g_i components, $i = x, y, z$ [56]), $\alpha^2 = 0.9$.

$$1/3(\Sigma\, \delta g_i - \Sigma A_i/P) = \alpha^2\kappa \quad (i = x, y, z) \tag{21a}$$

β in Table 8 is the nephelauxetic ratio B/B_0 for Ni^{2+} on the Mg^{2+} or Zn^{2+} positions, the Racah parameter $B_0 = 1040$ cm^{-1} being that of the free Ni^{2+} ion. It should be noted, that the β-values cited in the literature frequently differ due to a different choice of B_0. Also, similar to Δ (Eq. (1b)) the decrease of β due to covalency has been factorised by Jorgensen [1,58], with ligand and metal contributions h and k, respectively (Eq. (23)).

$$1 - \beta = h \cdot k \tag{23}$$

We refrain from doing this with the results in Table 8 explicitly, because in the case of weak bond covalencies the small $(1 - \beta)$ values are subject to larger errors. The ligand contributions h vary between about 1 and 2 for the oxidic solids collected in Table 8.

B can be derived accurately from the experimental spectra in all cases, where the highest energy spin-allowed d–d transition $^3A_{2g} \rightarrow {}_b^3T_{1g}$ is well resolved. For Δ/B values around 10 this transition depends approximately on $13B$, while the energetic position of the $^3A_{2g} \rightarrow {}_a^3T_{1g}$ transition is only weakly determined by interelectronic repulsion ($\sim 2B$). β can be estimated to have a tolerance of $\pm 0.01_5$ in these cases corresponding to ± 200 cm^{-1} in the $^3A_{2g} \rightarrow {}_b^3T_{1g}$ band position.

The β- and α-values show approximately the same trend (Table 8). A decrease of the nephelauxetic ratio indicates a reduced effective charge on the transition metal ion, induced by the *total* σ- and π-donor activities of the ligands. Thus, β—though reflecting 3d-contributions solely—can be considered to be a probe for the entire M–O bond properties. The mixing coefficient α describes the extent of the covalent interaction between M$^{\delta+}$ cations and O$^{\delta-}$ anions, again carrying effective charges δ, δ', which are reduced with respect to those in a purely ionic description. Hence, we may crudely argue that the two bonding parameters probe broadly analogous bond properties. They vary between 0.91 and 0.82 (β) and 0.95 and 0.84 (α) for

oxides, thus covering the wide range between F^- ($\beta = 0.91_5$, $\alpha = 0.92$) and N-ligator atoms ($\beta = 0.82_5$, $\alpha = 0.87$). If small high-valent, strongly polarising cations with a large ion potential (Eq. (19)) are present in the oxygen coordination sphere, electron density is withdrawn from the anion, leaving a considerably reduced effective ionic charge of the anions towards Ni^{2+} or Cu^{2+}. Oxygen becomes more electronegative by the electron density shift toward the higher-valent cations which then leads to a less pronounced covalency of the Ni(Cu)–O bond.

Though one can follow this principle through Table 8, there are some inconsistencies. C^{IV} and B^{III} induce a less ionic transition metal–oxygen bond in comparison to P^V and S^{VI}, inspite of their high ion potentials due to very small ionic radii. This might be caused by the π-bonds, which are present in the trigonal planar CO_3^{2-} and BO_3^{3-} anions. As is generally accepted, electrons involved in π-bonds possess a less donating character than electron pairs entering σ-bonds. Thus, in the mentioned cases less electron density is transfered to the C and B atoms from their oxygen neighbours (1π, 3σ bonds) than in PO_4^{3-} or SO_4^{2-} (4σ bonds). It is also surprising at the first sight, that the covalency of the Ni(Cu)–O bonds in the perovskite-type solids ($\beta \cong 0.82$, $\alpha \cong 0.87$) seems to be comparatively marked. We suppose that the presence of the large low-valent alkaline earth and/or rare earth cations in the oxygen coordination sphere outweighs the influence of cations such as W(VI) (see below). Indeed the complete absence of strongly contrapolarising cations leads to a very low α-value (Y_2BaZnO_4).

It is expected, that β shows a more pronounced variation in the case of Cr^{3+}. Frequently the quartet–doublet transitions $^4A_{2g}(t_{2g}^3) \rightarrow {}_a^2E_g$, ${}_a^2T_{1g}$ (both $\cong t_{2g}^3$) in the d–d spectra of octahedrally oxo-coordinated Cr^{3+} are resolved and allow to determine B_{55} or β_{55} (with $B_0 = 920$ cm^{-1}) with high precision (Fig. 32) [24]. B_{35} is accessible from the broad $^4A_{2g}(t_{2g}^3) \rightarrow {}_a^4T_{1g}(\sim t_{2g}^2e_g^1)$ transition, which depends, for Δ/B_{35} ratios around 25, on this parameter with a factor of ~ 7 (for further details see [24]). The third spin-allowed tansition $^4A_{2g}(t_{2g}^3) \rightarrow {}_b^4T_{1g}(\sim t_{2g}^1e_g^2)$ is weak in intensity ($\approx$ two-electron excitation) and covered mostly by charge-transfer bands. Table 9 comprises some reliable β_{55} and β_{35} data for Cr^{3+} in oxide ceramics from literature. The variation of β_{35} is more pronounced than that of β_{55}. This is expected, because the latter parameter only involves π-antibonding t_{2g} electrons, while β_{35} also implies interactions involving the more delocalised σ-antibonding e_g electrons. If the smaller higher-valent cations are successively replaced by large low-valent cations with high coordination numbers and hence only weak polarising influence on the oxygen environment, the less ionic the Cr–O bond appears to be. In agreement with the results for Ni^{2+} rather low nephelauxetic ratios are hence found in the case of perovskite-type compounds.

The results in Tables 8 and 9 and their interpretation find support by data, deduced from other independent physical methods. The optical basicities Λ and electronic polarisabilities $P(O)$ collected in Table 10 [59], which characterise the oxygen atoms of various oxides in their bonding behaviour towards cations such as Ni^{2+}, Co^{2+} or Cr^{3+}, show the same trend. Here, the former are relative numbers, which are derived from the $^1S_o \rightarrow {}^3P_1$ transition energies of Tl_2O, PbO or Bi_2O_3 doped into various host oxides and standardised with respect to CaO. The
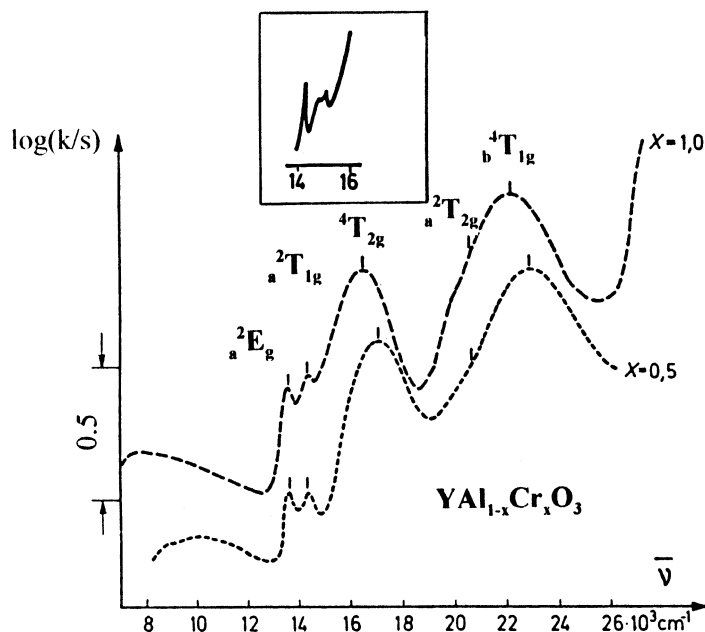
Fig. 32. d–d Powder spectra of perovskite mixed crystals $YAl_{1-x}Cr_xO_3$ (band positions calculated with $B_{55} = 705$ cm^{-1}, $C/B = 4.0$ and $\Delta = 17050$ (16450) cm^{-1}, $B_{35} = 555$ (545) cm^{-1} for $x = 0.5$ (1.0); the insert shows the lowest energy quartet–doublet transitions for Cr^{3+}-doped corundum $Al_{1.9}Cr_{0.1}O_3$.

transitions shift to higher energies, if the electronegativity of the oxygen ligator atoms towards the probe cations increases. The polarisibility values are deduced from opictal refractivity data. If ternary host compounds are investigated, $\Lambda(P)$ is found to have values between those of the constituting oxides [MgO: 0.78(1.71), SiO_2: 0.48(1.41) → $MgSiO_3$: 0.58(1.48) and Mg_2SiO_4: 0.63(1.51), for example]. Thus, the oxygen atoms in the elpasolites Ba_2NiWO_6 and Sr_2NiWO_6 are indeed expected

Table 9
Nephelauxetic ratios of octahedrally coordinated Cr^{3+} in various oxidic solids (data from [24]); the cationic oxygen coordination (cc) is also given; the upper indices in parentheses give the coordination numbers with respect to oxygen

Compound	β_{55}	β_{35}	cc	Structure
$Cr(OH_2)_6^{3+}$	(0.85)	0.79	$H_2OCr^{(6)}$	–
$Al_2O_3(Cr^{3+})$	0.80	0.73	$OAl_4^{(6)}$	Corundum
$MgAl_{2-x}Cr_xO_4$	(0.81)	0.70(1)	$Mg^{(4)}OAl_3^{(6)}$	Spinel
$ZnGa_{2-x}Cr_xO_4$	(0.81)	0.70(1)	$Zn^{(4)}OGa_3^{(6)}$	Spinel
$Y_3(Al_{2-x}Cr_x)Al_3O_{12}$	0.815	0.67(2)	$Y_2^{(8)}OAl^{(4)}Al^{(6)}$	Garnet
$Y_3(Ga_{2-x}Cr_x)Ga_3O_{12}$	0.815	0.67(2)	$Y_2^{(8)}OGa^{(4)}Ga^{(6)}$	Garnet
$YAl_{1-x}Cr_xO_3$	0.77	0.60	$Y_4^{(12)}OAl_2^{(6)}$	Perovskite
$LaAl(Ga)_{1-x}Cr_xO_3$	–	0.57(1)	$La_4^{(12)}OAl_2^{(6)}$	Perovskite

Table 10
Binding properties of oxygen in various oxide compounds towards other cations: optical basicities Λ, electronic polarisabilities $P(O)$, electronegativities $\chi(O)$ and effective charges $q(O)$; data from [59]

Compound	Λ	$P(O)$	$\chi(O)$	$q(O)$
SO_3	0.33	–	3.7	−0.4
P_2O_5	0.40	1.33	3.5	−0.6
B_2O_3	0.42	1.39	–	–
SiO_2	0.48	1.41	3.5	−0.6
Al_2O_3	0.60	1.46	3.4	−0.7
MgO	0.78	1.71	3.1	−1.0
CaO	1.00	2.49	3.0[a]	−1.1[a]
Li_2O	1.00	–	–	–
BaO	1.15	3.70	2.8	−1.3
Na_2O	1.15	–	2.6	−1.5
Cs_2O	1.7	–	2.2	−1.9

[a] Identical values: La_2O_3; between MgO and Al_2O_3: Y_2O_3 ($\chi(O) \approx 3.2$; $q(O) \approx -0.9$); near to CaO: SrO ($\chi(O) \approx 2.9$; $q(O) \approx -1.2$).

to be rather polarisable due to the presence of Ba^{2+} and Sr^{2+}, which induce comparatively pronounced covalency contributions to the Ni–O bond. A further source of information are thermochemical data (heats of formation) for oxides. They can be translated into oxygen electronegativity values (Pauling) $\chi(O)$, which depend on the chosen electronegativities for the metal atoms, though. From these effective charges $q(O)$ can be estimated, utilising the relation: $q(O) = \chi(O) - 4.1$, which is suggested from quantum chemical calculations [59] (Table 10). Though these numbers are rather coarse, they reproduce the broad range of observed β and α values summarised in Table 8, reaching from beyond nitrogen ($\chi = 3.0$)—see the low mixing coefficient α for Y_2BaZnO_5—to nearly fluoride ($\chi = 4.0$).

We conclude by stating, that the nephelauxetic ratios (Ni^{2+}, Cr^{3+}) and the mixing coefficients α in the ground state MO of Cu^{2+} are a consistent and reliable, though relative, measure of the covalency contributions to the transition metal–oxygen bond, as has been demonstrated for a great variety of oxidic solids. The critical quantity is the geometry and constitution of the cationic coordination of the oxygen atoms in the respective crystal structure. These chemical and structural features also determine the magnitudes of the ligand field strength Δ and of the constituting AOM energies e_σ, e_π. In contrast to β and α these parameters are rather complex bonding probes, however, as this has been discussed extensively in Section 3. Oxygen is singular in its bonding behaviour due to the variability of the cationic coordination, with coordination numbers between three (trirutile lattice) and six (elpasolite structure) and oxidation states of the coordinating cations between + I and + VI. Fluorides and chlorides are much less variable, because the lower anionic charge does usually not allow cations of high valence to be present in the F^- or Cl^- coordination sphere. On the other hand, nitride is a very promising candidate for studying the transition metal–nitrogen bond properties, but unfortunately the available spectral data are very scarce.

4.2. The stabilisation of nickel(III,IV) and copper(III) in oxide matrices

The data collected in Tables 8–10 can be helpful in establishing criteria, how the electronic properties of ligator atoms are correlated with the maximal oxidation states of transition metal ions bonded to these ligands. It is well known, that higher oxidation states of the late 3d cations—such as Ni^{III} or Cu^{III}—can be stabilised by strongly electronegative anions. Examples are solids $A_2A'M^{III}F_6$ with the elpasolite structure (A,A′: alkaline ions; $M^{III} =$ Al, Ga, Ni, Cu), where Cu and Ni occupy the octahedral M^{III} positions. They possess $t_{2g}^6 e_g^2$ [60] and low-spin $t_{2g}^6 e_g^1$ (Jahn–Teller distortion present [61]) ground state configurations, respectively. Interesting is also the existence of a compound $Na_5[Cu(HIO_6)_2] \cdot yH_2O$ with square-planar $Cu^{III}O_4$ entities [62], where the strongly contrapolarising I^{VII} cations presumably generate a rather ionic Cu–O bond. However, covalent ligands may also stabilise Ni^{III} and Cu^{III}. In contrast to the situation in the mentioned ionic fluoride and oxide complexes the stabilising factor here is the pronounced reduction of the cation charge by electron donation from the ligands, shifting the metal orbitals to lower energies. Typical examples of this type are the solids AMO_2 ($A^I =$ Na, K, Rb,Cs; $M^{III} =$ Ni [63], Cu [64]) and $La_2Li_{1/2}M_{1/2}O_4$ ($M^{III} =$ Co, Ni, Cu), the latter crystallising in the ordered K_2NiF_4 structure [65]. The oxygen atoms are involved in rather covalent bonds with the M^{III} cations in these compounds, because the contrapolarising forces of the alkaline and La^{3+} cations are comparatively weak (see the bonding characteristics of Ni^{II} and Cu^{II} in Table 8 and the discussion in the preceding subsection). However, much more covalent ligator atoms such as sulfur in dithiocarbamate with sulfur ligator atoms for example (Table 8) may also generate Cu^{III} and even Ni^{IV}. The former forms very stable square-planar complexes $Cu(dtc)_2^+$, which are easily obtainable under mild oxidation conditions from the corresponding neutral Cu^{II} complex [57].

While the Cu^{II}–O bond is mainly ionic—the unpaired electron (Eq. (20)) possesses predominant metal d-character between 70 and 90%, as measured by α^2 (Table 8)—the Cu^{III}–O overlap is much more pronounced covalent. It is estimated from X-ray absorption spectroscopy that the d-electrons are delocalised strongly in $La_2Li_{1/2}Cu_{1/2}O_4$, but still reside with a probability $> 50\%$ at the transition metal [66]. The one-electron MO scheme in Fig. 33 (below) gives a schematic sketch of this situation for a low-spin square-planar Cu^{III} complex—with antibonding MO's resulting from d_{xz}, d_{yz} (e_g^*), d_{xy} (b_{2g}^*) and d_{z^2} (a_{1g}^*), which are occupied fully and an empty σ-antibonding $d_{x^2-y^2}$ (b_{1g}^*) MO. Switching to a ligand field of sulfur atoms from dtc we already find for Cu^{II} a pronounced covalency, α^2 being 0.54 (Table 8). Hence, it is expected that the 3d electrons in the corresponding Cu^{III} complex reside preferentially on the ligands. This corresponds to a MO scheme, in which the metal atoms possess a very low effective charge, the metal orbitals being located below those of the ligand orbitals (Fig. 33, above). Such a case does not always imply an energetically stable situation, because interelectronic repulsion—which is not taken into account in conventional one-electron MO diagrams—eventually destabilises the non-bonding ligand orbitals to a larger extent than the nearby antibonding MOs. This may give rise to an electron flow from the non-bonding to empty or only partially occupied antibonding ligand-centred MOs. The instability either occurs in

the ground state or by low-energy optical excitation, leading to decomposition by the reduction of the metal atom and oxidation of the ligand. Ab-initio calculations on $Fe^{VI}O_4^{2-}$ tetrahedra suggest that a redox process of this kind might indeed occur [67].

After all the available experimental material of compounds with cobalt, nickel and copper indicates, that the higher oxidation states ($\geq III$) can be stabilised not only by strongly electronegative, but also by covalent ligands. A more pronounced covalency leads to small effective charges on the cations and hence energetically strongly stabilised, low-lying metal orbitals (Fig. 33, above) in extreme cases. Here redox processes between the metal and the ligator atoms are possible, depending on the nature of the non-bonding orbitals on the ligand. These considerations might contribute to the understanding of the role of Cu^{II} and Cu^{III} in superconducting oxide ceramics. The oxygen atoms in solids of that kind are typically of rather low electronegativity, because only large cations with high coordination numbers and with correspondingly weak contrapolarising forces, such as Ba^{II}, Bi^{III}, La^{III}, etc. are present besides copper.

It should finally be noted, that the charge-transfer spectra are a further valuable source of information concerning the bond properties [1,58]. The ligand-to-metal charge transfer tansitions shift to lower energies with increasing oxidation state of the transition metal ion and hence increasing bond covalency. In the case of oxidic copper(III) and nickel(III,IV) solids they are located in the visible region, imparting brownish to black colours to these compounds. An interesting feature is here, that the covalency of the transition metal–oxygen bond becomes more pronounced, if one switches from solids with isolated polyhedra to compounds where these polyhedra are interconnected by common oxygen ligator atoms-due to electron transfer between the $3d^n$ cations and hence to a more distinct electron delocalisation [68]. This matter is beyond the scope of this article, however.
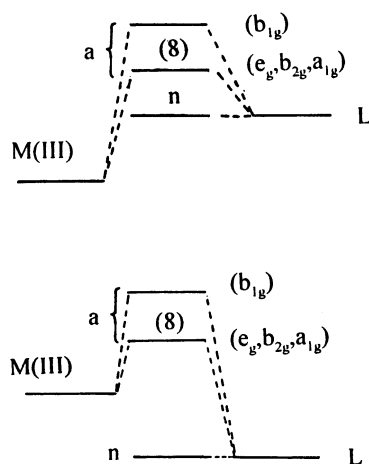

Fig. 33. Schematic MO diagrams of tetragonally elongated ML_6 or square-planar ML_4 complexes (D_{4h} symmetry); only the sections with the nonbonding (n) and antibonding (a) orbitals are shown. The electron configuration is that of low-spin Cu^{III}; the effective charge of M^{III} is distinctly smaller in the above scheme.

Appendix A. The spinels Ni_2GeO_4 and Co_2GeO_4: energy matrices for d^8 and d^7 cations (a) and calculated ligand field transitions for Ni_2GeO_4 (b)

(a) Matrices for the high-spin states of a d^8 cation in a trigonal (D_{3d}) ligand field are listed in Table A1 [16]. The parameters K and K' (positive values correspond to a trigonal compression) have been defined in terms of the AOM model for small angular distortions from cubic symmetry in Eq. (4)—conventional approach—and for misoriented ligand orbitals of sp^3- and sp-hybrid type in Eqs. (5) and (6), respectively. Δ and B are parameters of the cubic ligand field (Eq. (1)) and interelectronic repulsion, respectively. The parent octahedral terms are indicated in parenthesis. The same equations are also valid for the d^7 electron configuration, when changing the signs of Δ, K and K'.

Table A1

$^3E_g(T_{2g})$	$^3E_g(_aT_{1g})$	$^3E_g(^bT_{1g})$	$^3A_{2g}(A_{2g})$	$^3A_{2g}(_aT_{1g})$	$^3A_{2g}(_bT_{1g})$
$\Delta+(1/2)K$	$(3/2)K$	K'	0	$-2K'$	0
$(3/2)K$	$\Delta+12B+(1/2)K$	$6B+K'$	$-2K'$	$\Delta+12B-K$	$6B-2K'$
K'	$6B+K'$	$2\Delta+3B+K$	0	$6B-2K'$	$2\Delta+3B-2K$

$^3A_{1g}(T_{2g})$ $\Delta-K$.

Matrices for ligand fields of misaligned metal–ligand bonds with lower symmetries can not be written in a closed form. For such cases a generalisation of the formalism for bent metal–ligand bonds has been performed [13]. Examples demonstrating the effect of large trigonal distortions on high-resolution optical spectra of Cr^{III} complexes are given elsewhere [69].

(b) Numerical values of the transition energies calculated using sp and sp^3 hybridised ligand orbitals (Section 2.1) are given in Table A2 for Ni_2GeO_4. In these calculations the oxygen atoms occupy regular octahedral positions, but the ligand field is of D_{3d} symmetry as the result of strong perturbations from the second coordination sphere. For comparison the experimental band energies are also given. Parameter values are those of Eqs. (7), (7a) and (5a).

Table A2

sp-Model				sp^3-Model				Experiment [16]
$\varsigma = 0$		$\varsigma = 520$		$\varsigma = 0$		$\varsigma = 520$		
$^3A_{2g}$	0	A_{1g}	5	$^3A_{2g}$	0	A_{1g}	0	
		E_g	0			E_g	5	
$^3A_{1g}$	8346	E_g	8319	^3E_g	8961	E_g	8757	
		A_{2g}	8351			E_g	8888	$\cong 8000$

Table A2 (*Continued*)

sp-Model				sp³-Model				Experiment [16]
$\varsigma = 0$		$\varsigma = 520$		$\varsigma = 0$		$\varsigma = 520$		
^2E_g	9150	E_g	8984			A_{1g}	9201	
		E_g	9188			A_{2g}	9026	
		A_{1g}	9362	$^3A_{1g}$	9173	E_g	9265	9100
		A_{2g}	9394			A_{2g}	9378	
^3E_g	14542	A_{1g}	14021	$^3A_{2g}$	13594	A_{1g}	13546	
		A_{2g}	14307			E_g	13923	
		E_g	14469	^3E_g	15414	A_{2g}	15183	
		E_g	15009			A_{1g}	15254	15100
$^3A_{2g}$	14812	A_{1g}	15117			E_g	15629	
		E_g	15342			E_g	15924	
$^3A_{2g}$	22975	E_g	23179	^3E_g	24283	E_g	24304	
		A_{1g}	23274			E_g	24481	23100
^3E_g	25902	E_g	25908			A_{1g}	24619	
		E_g	25960			A_{2g}	24509	
		A_{1g}	26190	$^3A_{2g}$	26675	E_g	26824	26000
		A_{2g}	26202			A_{1g}	26843	
^1E_g	13460	E_g	13324	^1E_g	13450	E_g	13187	$\cong 13000$
$^1A_{1g}$	21076	A_{1g}	20930	$^1A_{1g}$	21601	A_{1g}	21629	21000
^1E_g	22349	E_g	22174	^1E_g	21866	E_g	21727	
$^1A_{1g}$	22242	A_{1g}	22312	$^1A_{1g}$	23204	^1A_g	23148	
$^1A_{2g}$	25686	A_{2g}	25735	^1E_g	26228	E_g	26288	
^1E_g	26494	E_g	26656	$^1A_{2g}$	26513	A_{2g}	26616	

Appendix B. d–d Transition energies for $NiSb_2O_6$ (left) and $NiTa_2O_6$ (right)

Table A 3
Observed band positions (10^3 cm^{-1}) are compared with those calculated in the AOM (sp² hybrid orbitals on oxygen, see Section 2.4.1 and Figs. 18 and 19)

Experimental	Calculated		Calculated	Experimental
8.2	8.43	$^3B_{2g}$	7.70	~7.3
	8.65	$^3B_{3g}$	7.87	
9.6	9.30	^3A_g	7.97	
13.5	13.25	$^3B_{3g}$	12.22	12.5

Table A3 (*Continued*)

Experimental	Calculated		Calculated	Experimental
	14.91	$^3B_{1g}$	13.32	
15.4_5	15.58	$^3B_{2g}$	13.81	13.8
–	13.30	^1A_g	13.34	
	13.44	$^1B_{1g}$	13.41	
	21.32	$^1B_{3g}$	20.62	
–	21.50	$^1A_{1g}$	20.71	$\cong 20.7$
	21.92	$^1B_{2g}$	21.00	
–	22.92	$^1A_{1g}$	22.01	–
	24.27	$^3B_{2g}$	22.79	
–	25.23	$^3B_{1g}$	23.61	23.4
	25.36	$^3B_{3g}$	23.62	

The used parameter sets are given in Eqs. (11) and (13) for $NiSb_2O_4$ and $NiTa_2O_6$, respectively ($^3B_{1g}$ ground state, without LS coupling).

References

[1] C.K. Jørgensen, Orbitals in Atoms and Molecules, Academic Press, New York, 1962.
[2] C.K. Jørgensen, Oxidation Numbers and Oxidation States, Springer, Berlin, 1969.
[3] (a) C.K. Jørgensen, R. Papalardo, H.-H. Schmidtke, J. Chem. Phys. 39 (1963) 1422. (b) C.E. Schäffer, C.K. Jørgensen, Mol. Phys. 9 (1965) 401.
[4] A.J. Bridgeman, M. Gerloch, Progress in Inorganic Chemistry, Wiley-Interscience, New York, vol. 45, 1997, p. 179 and references therein.
[5] D.W. Smith, J. Chem. Soc. (A) (1969), 1708 and 2529.
[6] D.W. Smith, Inorg. Chem. 17 (1978) 3153.
[7] (a) D. Reinen, Theor. Chim. Acta 5 (1966) 312. (b) D. Reinen, Thesis of Habilitation, Bonn, 1965.
[8] L. Pauling, The Nature of the Chemical Bond, 3rd ed., Cornell University Press, Ithaca, NY, 1960.
[9] A.D. Liehr, J. Phys. Chem. 68 (1964) 665 and 3629.
[10] M.J. Duer, N.D. Fenton, M. Gerloch, Int. Rev. Phys. Chem. 9 (1990) 227 and references therein.
[11] M. Atanasov, G.St. Nikolov, Commun. Dept. Chem. Bulg. Acad. Sci. 16 (1983) 329.
[12] J.M. Kennedy, C.E. Schäffer, Inorg. Chim. Acta 252 (1996) 185.
[13] M. Atanasov, in preparation.
[14] (a) J.W. Richardson, W.C. Nieuwpoort, R.R. Powell, W.F. Edgell, J. Chem. Phys. 36 (1962) 1057. (b) J.A. Pople, D.L. Beveridge, Approximate Molecular Orbital Theory, McGraw-Hill, New York, 1970, p. 29.
[15] R.B. von Dreele, A.L. Bowman, Acta Crystallogr. B33 (1977) 2287.
[16] D. Reinen, Theor. Chim. Acta 8 (1967) 260.
[17] F.C. Romejn, Phil. Res. Rep. 8 (1953) 304.
[18] R.D. Shannon, Acta Crystallogr. A32 (1976) 751.
[19] S. Sugano, Y. Tanabe, H. Kamimura, Multiplets of Transition Metal Ions in Crystals, Academic Press, New York, 1970.
[20] D. Reinen, Ber. Bunsenges. Physikal. Chem. 69 (1965) 82.
[21] W. Rauw, Thesis, Marburg, 1997.
[22] J.E. Weidenborner, N.R. Stemple, Y. Okaya, Acta Crystallogr. 20 (1966) 761.

[23] P. Poix, Ann. Chim. 10 (1965) 49.
[24] D. Reinen, Struct. Bond. (Berlin) 6 (1969) 30.
[25] D. Boström, Am. Miner. 72 (1987) 965.
[26] S.A. Warda, S.L. Lee, Z. Kristallogr. New Crystallogr. Struct. 212 (1997) 319.
[27] P. Köhler, G. Amthauer, J. Solid State Chem. 28 (1979) 329.
[28] D. Reinen, M.A. Hitchman, Z. Phys. Chem. 200 (1997) 11.
[29] D. Reinen, Z. Anorg. Allg. Chem. 356 (1968) 182.
[30] O. Schmitz-DuMont, C. Friebel, Monatsh. Chem. 98 (1967) 1583.
[31] F. Pertlik, Acta Crystallogr. C42 (1986) 4.
[32] A. Bystrøm, B. Hock, B. Mason, Ark. Kem. Miner. Geol. B15 (1941) 1.
[33] Hk. Müller-Buschbaum, Z. Anorg. Allg. Chem. 536 (1986) 15.
[34] V. Propach, D. Reinen, Z. Anorg. Allg. Chem. 369 (1969) 278.
[35] H. Kasper, Monatsh. Chem. 98 (1967) 2104.
[36] E.O. Giere, A. Brahimi, H.J. Deiseroth, D. Reinen, J. Solid State Chem. 131 (1997) 263.
[37] A. Nakua, H. Yun, J.N. Reimers, J.E. Greedan, C.V. Stager, J. Solid State Chem. 91 (1991) 105.
[38] D. Reinen, Z. Naturforsch. 23 (1968) 521.
[39] D. Reinen, H. Weitzel, Z. Anorg. Allg. Chem. 424 (1976) 31.
[40] F. Steffens, D. Reinen, Z. Anorg. Allg. Chem. 441 (1978) 63.
[41] F. Steffens, PhD Thesis, Marburg, 1978.
[42] D. Reinen, U. Kesper, D. Belder, J. Solid State Chem. 116 (1995) 335.
[43] Hk. Müller-Buschbaum, Z. Anorg. Allg. Chem. 503 (1983) 101.
[44] B. Kratzheller, R. Gruehn, J. Alloys Comp. 183 (1992) 75.
[45] D. Reinen, C. Friebel, Struct. Bond. 37 (1979) 1.
[46] D. Reinen, U. Kesper, unpublished results.
[47] J. Norwig, H. Weitzel, H. Paulus, G. Lautenschläger, J. Rodriguez-Carvajal, H. Fuess, J. Solid State Chem. 115 (1995) 476.
[48] A. Neuhaus, W. Richartz, Angew. Chem. 70 (1958) 430.
[49] G. Blasse, J. Inorg. Nucl. Chem. 26 (1964) 1191.
[50] G. Blasse, J. Inorg. Nucl. Chem. 27 (1965) 993.
[51] G. Steffen, D. Reinen, H. Stratemeier, M.J. Riley, M.A. Hitchman, H.E. Matthies, K. Recker, F. Wallrafen, J.R. Niklas, Inorg. Chem. 29 (1990) 2123.
[52] D. Getz, B.L. Silver, J. Chem. Phys. 61 (1974) 630.
[53] J. Wegwerth, Thesis, Marburg, 1994.
[54] D. Reinen, J. Wegwerth, Physica C 183 (1991) 261.
[55] D. Reinen, A. Ozarowski, B. Jakob, J. Pebler, H. Stratemeier, K. Wieghardt, T. Tolksdorf, Inorg. Chem. 26 (1987) 4010.
[56] A. Ozarowski, D. Reinen, Inorg. Chem. 24 (1985) 3860 and references therein.
[57] (a) C.P. Keijzers, H.J.M. deVries, A. van der Avoird, Inorg. Chem. 11 (1972) 1338. (b) J. Willemse, J.A. Cras, J.J. Steggerda, C.P. Keijzers, Struct. Bond. 28 (1976) 84.
[58] A.B.P. Lever, Inorganic Electronic Spectroscopy (Series: Studies in Physical and Theoretical Chemistry, vol. 33, Elsevier, Amsterdam, 1984 and references cited therein.
[59] J.A. Duffy, Bonding, Energy Levels and Bands in Inorganic Solids, Longman, Harlow, UK, and Wiley, New York, 1990, Ch. 6.
[60] G.C. Allen, K.D. Warren, Struct. Bond. 9 (1971) 49.
[61] D. Reinen, C. Friebel, V. Propach, Z. Anorg. Allg. Chem. 408 (1974) 187.
[62] V. Adelsköld, L. Eriksson, P.L. Wang, P.E. Werner, Acta Crystallogr. C44 (1988) 597.
[63] L.D. Dyer, B.S. Borie Jr., G. Pedro Smith, J. Am. Chem. Soc. 76 (1954) 1499.
[64] (a) K. Hestermann, R. Hoppe, Z. Anorg. Allg. Chem. 367 (1969) 249 and 261. (b) N.E. Brese, M. O'Keeffe, R.B. von Dreele, V.G. Young Jr., J. Solid State Chem. 83 (1989) 1. (c) J. Pickardt, W. Paulus, M. Schmalz, R. Schöllhorn, J. Solid State Chem. 89 (1990) 308.
[65] S.A. Warda, W. Pietzuch, G. Berghöfer, U. Kesper, W. Massa, D. Reinen, J. Solid State Chem. 138 (1998) 18.
[66] Z. Hu, G. Kaindl, S.A. Warda, D. Reinen, F.M.F. de Groot, B.G. Müller, Chem. Phys. 232 (1998) 63.
[67] M. Atanasov, H. Adamsky, K. Eifert, J. Solid State Chem. 128 (1997) 1.
[68] M. Atanasov, D. Reinen, J. Electron Spectrosc. Relat. Phenom. 86 (1977) 185.
[69] Th. Schönherr, Topics Curr. Chem. 191 (1997) 87.